SCUOLA DI DOTTORATO
UNIVERSITÀ DEGLI STUDI DI MILANO-BICOCCA

Department of Materials Science

PhD Course in Science and Nanotechnology of Materials
XXX Cycle

Curriculum in Materials Science

Novel materials for solar energy conversion devices: Towards industrial scaling-up

Francesco Carulli

Registration number 710022

Tutor: Prof. Sergio Brovelli

Co-tutor: Dr.ssa Silvia Luzzati

Coordinator: Prof. Marco Bernasconi

ACADEMIC YEAR 2016/2017

Preface

In this thesis, I report the result obtained during my three years PhD focusing on the study of light-energy conversion devices, involving both fundamental research and technological application. My PhD work can be divided into two main topics: the first was developed with the collaboration of the University of Milano-Bicocca, concerning the study of novel emitters for luminescent solar concentrators (LSCs), under the supervision of Prof. Sergio Brovelli. The second, which represents the majority of my work, was performed at Consiglio Nazionale della Ricerca (CNR), inside the ISMAC group under the supervision of dr. Silvia Luzzati and is focused on the study of novel functional materials for polymeric solar cell (PSC) applications regarding both photoactive layers and interface engineering layers.

During my stay in CNR, I had the opportunity to increase my know-how on PSCs and to interact with industrial research environment by participating to an industrial research project with ENI group. This part of my research activity is covered by industrial secret and is thus not included in the following dissertation.

Specifically, in the first part spent at the university of Milano-Bicocca I worked on LSC based on silicon-based Quantum Dots (SI-QDs) as novel emitting nanomaterials, with the aim of overcoming the efficiency-limiting light reabsorption phenomena in the device. Firstly, I demonstrated that these nanostructures composed by earth-abundant element can be effectively adopted as chromophores in high-performance LSCs to limit re-absorption losses. Secondly, I proved that the optical properties of flat devices can be maintained also in curve and flexible LSCs, a fundamental step to spread their application range, without altering their efficiency.

In the second part of my PhD, I focused on a different solar light conversion device, polymeric bulk hetero junction (BHJ) solar cells with direct architecture. In this field I initially performed a comparative study on the performance of PSCs based on PBDTTPD, a donor polymer which combines a simple molecular structure with good photovoltaics (PV) properties. Such polymer, obtained via standard Stille reaction, was compared with the same PBDTTPD obtained through a novel synthetic route which provides fewer preparation steps without involving the use of heavy-metal based catalyst. The fabricated devices were studied in terms of external quantum efficiency, morphology-performance relationship and charges recombination dynamics, demonstrating the effectiveness of the new synthetic strategy for the production of PBDTTPD as efficient PV grade donor for BHJ solar cells.

Lastly, as a continuation of the work on BHJs, I studied the effect of a novel, alcohol soluble, poly-fluorene-based interlayer on PSC, which still allows a full solution process device assembly and induce a remarkable enhancement of the PSC efficiency. In particular, I worked with emphasis on two different topics: firstly the description of the mechanism inducing the PV performances improvement, distinguishing the effect on interfacial engineering of interlayers from the effect of solvent used during their deposition through photo-electrical, electrical and surface characterization. Secondly I focused on the study of the degradation phenomena in the device, a topic which is often omitted, and its kinetics in relation with presence of interlayer and different metallic cathodes.

Summary

PART I

PART II

PART I

1. Luminescent solar concentrators

1.1. Introduction

1.1.1. Device Structure

Luminescent solar concentrators (LSCs) consist of a semi-transparent slab of polymeric or glassy matrix doped or coated with highly emissive chromophore species[1]. The chromophores can absorb a fraction of incident sunlight, both direct and diffused, and re-emit a lower energy radiation inside the slab. A large fraction of the re-emitted light inside the slab is guided by total internal reflection to the edges where classical PV cells are coupled for its conversion into current [1-4]. In this way, LSCs collect light from the most extended surface and concentrate it on the small edges, greatly increasing the flux of radiation reaching the PV cells and boosting the photocurrent.

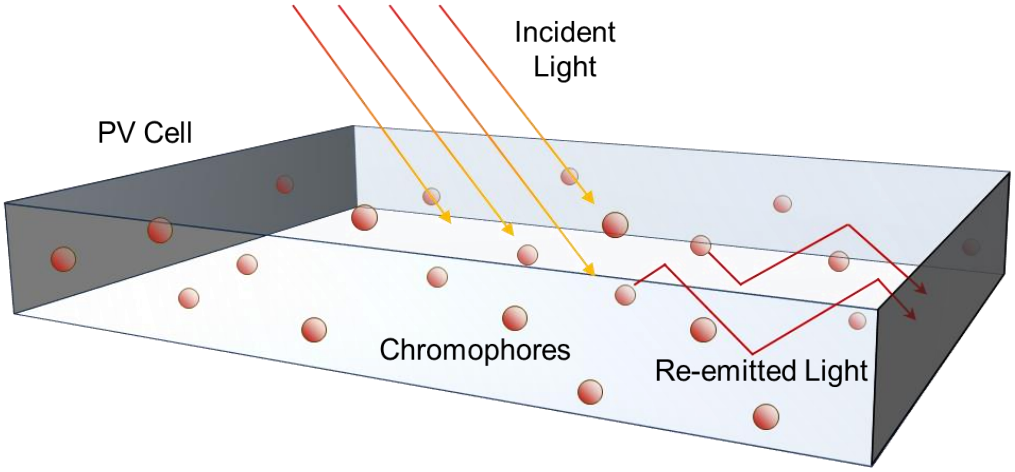

Figure 1.1.: Structure of a luminescent solar concentrator.

1.1.2 History of LSC

The first luminescent solar concentrator (LSC) type architecture, published in 1973 by Lerner[5], aroused a great interest in the development of the device, leading to a large amount of publications[6, 7]. Initially, this technology was designed with the aim of limiting the use of silicon, whose production in those years was still expensive, in PV devices. The drop of oil cost in the 80s, which decreased the interest in renewable energies, combined with a very marked decrease of the manufacturing cost of silicon for inorganic PV cells yielded to a near-abandonment of the research focused on LSCs.

However, in the early 21st century there has been a remarkable reawakening of interest in LSCs[8] mainly due to two factors. Firstly it is due to the increasing awareness in the general public of the dwindling fossil-fuel availability, resulting a in forward thinking public policies which is encouraging the development of renewable energy devices[9]. Secondly, LSC technology was able to carve out a novel spot in the renewable-energy device market, no longer as competitor of Si-based PV cells in the power energy production (solar farms), but rather as a new complementary technology[8]. This new approach could take LSC to integrate the PV technology in not yet explored contests of building integrated PV, as semi-transparent or transparent solar windows[10].

In the last years, building integrated PV is already transforming urban architecture by allowing to reach the ambitious goal of net zero energy consumption buildings[11]. However, the transition to fully renewable energy-based buildings has to be diversified taking into consideration the degree of urbanization and the number of inhabitants. On one hand, in environments where the population density is low, the zero energy consumption buildings goal is already possible through the use of self–sustaining houses, mainly based on the rooftop installation of PV modules supplying the energetic demands of the inhabitants[12]. On the other hand, in highly populated urban contests, where architecture is mainly developed in height, the extension of available horizontal surfaces for the rooftop installation of standard solar PV cells does not guarantee a sufficient energy supply[13].

In this scenario, one possible solution is represented by the exploitation of the abundance of vertical surfaces, in particular of large transparent or semi-transparent windows. In that context, luminescent solar concentrators (LSC) can play an important role as they provide a mean to realize energy-producing units that can be integrated into buildings facades without detrimental effects on their aesthetic and preserving the transparency required for the activities inside.[8, 13-16]

1.1.3 Working mechanism

The final efficiency of a LSC is related to the efficiency of the mechanisms which take place in its functioning. Differently from other opto-electronic devices, as organic solar cells, once the optical properties of the materials composing the LSC are known, the efficiency of those mechanisms can be generally predicted with good accuracy. The processes involved in the functioning of a LSC are mainly four, absorption, emission, transport and collection[17], and a brief description of each one of them will be provided in the following.

Absorption of incident sunlight depends on the absorption cross section (or molar extinction coefficient for organic molecules) of the chromophores embedded into the matrix. Even though this feature is easily controllable by adjusting the concentration of the absorbing species inside the slab, high absorption cross-section chromophores are preferred. The strategy of increasing the concentration of a low cross section species in the slab could lead to solubility problems such as phase separation or chromophores precipitation[18]. Secondly, in order to guarantee a proper coverage throughout the whole solar spectrum, the chosen chromophore should exhibit an absorption cross-section as high as possible in the visible spectral region, where the solar spectrum exhibits its maximum irradiance[19].

The matrix optical property also influences the absorbance of the device, since its reflectivity reduces the intensity of the incident radiation with a factor $1 - R(\lambda)$.

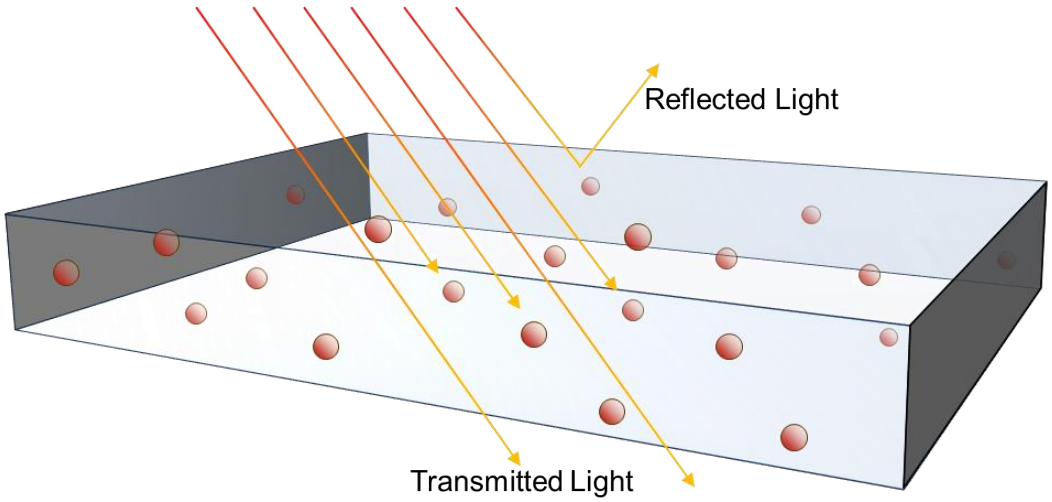

Figure 1.2: Illustration of the processes involved with absorsption in a LSC.

All these mechanisms are displayed in fig 1.2. and thus the efficiency of absorption process is expressed as:

$$\eta_{ABS} = \int \left(1 - e^{-\alpha \cdot (\lambda) C \cdot d}\right) \cdot (1 - R(\lambda))\, d\lambda$$

Where $\alpha_C(\lambda)$ is the absorbance cross section or molar extinction coefficient of the chromophore, C is its concentration, $R(\lambda)$ is the reflectivity of the matrix and d is the device thickness.

Emission is another process regarding mainly the chromophores (fig 1.3). In order to obtain high efficiency LSCs, the quantum efficiency of the chromophores should be close to unity, so that the losses because of non-radiative decays are minimized[20, 21]. As second important feature, which partially also includes the absorption process, the chromophores should exhibit a large energy separation between absorbance and photoluminescence profile, so-called Stokes Shift. A low Stokes Shift results in a strong overlap between absorption and photoluminescence profiles, which leads chromophores to re-absorb their own luminescence, through a process called self-absorption[12]. Self-absorption loss is the major efficiency-limiting factor especially in large area devices. In large are devices, the re-emitted photons travel for tens of centimetres inside the device before reaching the slab edges, with a consequent high probability of being re-absorbed by another chromophore[5, 22-24]. This latter chromophore in its turn re-emits photons isotropically with a probability determined by its quantum efficiency.

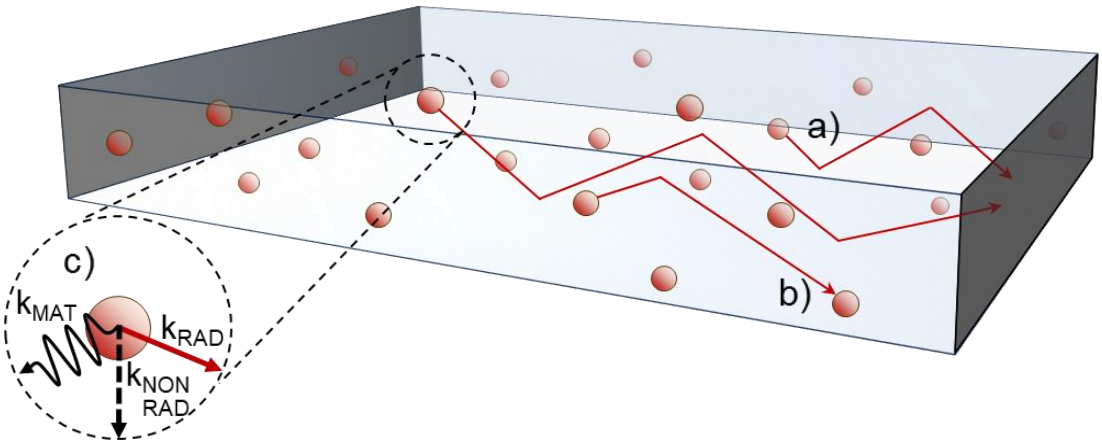

Figure 1.3: Illustration of the processes involved with emission in a LSC: a) emitted photons not experiencing re-absorption; b) re-absorbed emitted photons; c) decay mechanisms of a chromophore.

The randomization of the photons path by consecutive re-absorption/re-emission processes and the non-unity of the chromophores emission efficiency result in a progressive loss of the emitted photoluminescence and thus in a strong limitation for the device performance[25-27]. The efficiency of the emission phenomena inside the device can be expressed as:

$$\eta_{EM} = \int \Phi_{PL} \cdot (1 - \eta_{SA}(\lambda)) \cdot d\lambda$$

Where Φ_{PL} is the photoluminescence efficiency of the chromophore in the matrix, and $\eta_{SA}(\lambda)$ is the reabsorption efficiency. Φ_{PL} is the chromophore emission efficiency in the matrix because matrix may induce the generation of non-radiative decay paths[28], in particular considering that the fabrication of the device is typically performed by the incorporation of chromophores inside liquid monomer and subsequently polymerized. To avoid this kind of quantum efficiency drop as a consequence of the device assembly, several strategies have been adopted to protect chromophores from polymerization process, including capping with protective ligands or growth of a protective shell around the part of the chromophores assigned to emission[29, 30]. As mentioned above, η_{RA} is a process which involves both emission and absorption since it takes into account the possible sequential re-absorption/re-emission processes due to their spectral overlap and has to be calculated considering the dimensions and the shape of the device, since self-absorption is also dependent from the distance travel by photons inside the slab.

The choice of an emitting species with optimized optical features can minimize the losses related to absorption and emission. As far as the transport process is concerned, it is mainly determined by the hosting matrix. The choice of the hosting material is fundamental and it should be made primarily considering its optical properties, in particular its absorbance and its refractive index, since such features define the transport mechanism[28, 31]. On one hand, the overlap between absorbance of the matrix and photoluminescence profile of

chromophore may result in strong absorption, thus the hosting material should present a very high transparency in the spectral region of chromophore emission profile. This feature is fundamental if large area devices are considered, in which even very slight absorbance coefficients can generate huge re-absorbance for light travelling for tens of centimetres inside the matrix.

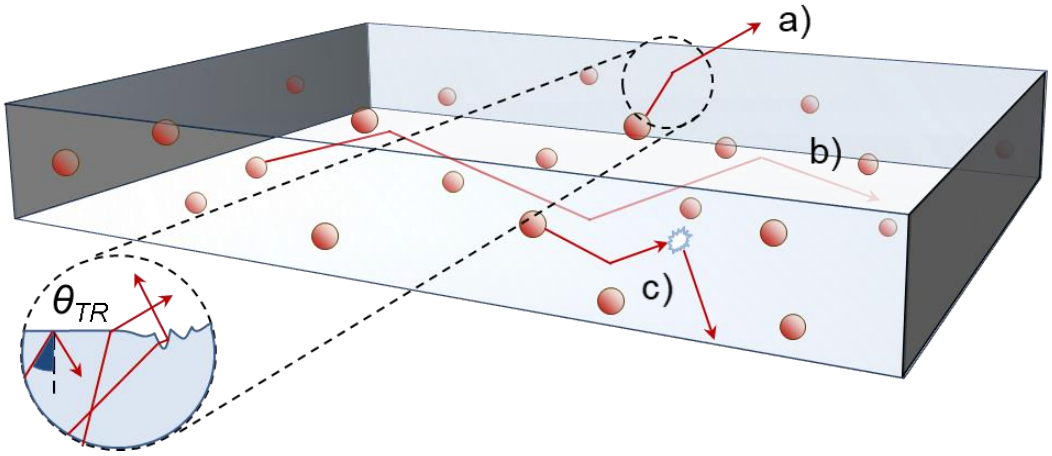

Figure 1.4: *Illustration of the processes involved with transport in a LSC: a) photon escaping from the LSC due to surface roughness/incident angle smaller than θ_{TR}; b) radiation absorption by the matrix; c) matrix-related photon scattering.*

If the chromophore luminescence is in the near infrared region of spectrum, even vibrational modes and their overtones have to be taken into consideration, especially for polymer-based matrix[26, 32]. On the other hand, the refractive index determines the LSC total internal reflection capability since the ratio between external environment and matrix refractive index determines θ_{TR}, which is the maximum incident angle to have total internal reflection. The fraction of photons approaching the surfaces with higher angle than θ_{TR}, experiences total internal reflection, whereas the others are lost passing through the surfaces. For a figure of merit, consider that a matrix of PMMA in air (refractive index of PMMA 1.5, of air 1) losses through the surface the 25% of the total light emitted inside the slab.

Similarly to matrix absorption, also the poor optical quality of the slab may worsen the transport properties of the device. Poor optical quality can be due to the presence of aggregates centres inside the slab, which can modify the

photons travelling direction through scattering, [13, 29, 33] or, similarly, a high surfaces roughness (processes depicted in fig 1.4)[34].The efficiency of the transport mechanism in the device can be summarized as:

$$\eta_{TR} = \int (e^{-\alpha_{WG}(\lambda)\cdot L}) \cdot \big(1 - \eta_S(\lambda)\big) \cdot \eta_{WG} d\lambda$$

Where $\alpha_{WG}(\lambda)$ is the absorption coefficient of the matrix, L is a distance parameter, $\eta_S(\lambda)$ is the scattering efficiency of the matrix and η_{WG} is the wave-guiding efficiency. L must take into consideration the distance travelled by the light inside the device, so it is dependent on the shape and dimension of the LSC, as well as on the distance travelled by light inside the slab, while η_{WG} must take into account the loss due to surface roughness η_{SR}, as well as the effect of total internal reflection. The latter is directly derived from the refractive index $(n_{MAT})$of the material as:

$$\theta_{TR} = \arcsin\left(\frac{n_{AIR}}{n_{MAT}}\right)$$

$$\eta_{TR} = \frac{1}{2\pi}\int_0^{2\pi}\int_0^{\theta_{TR}} \sin(\theta) d\theta d\varphi$$

$$\eta_{WG} = \eta_{TR} \cdot \eta_{SR}$$

The total efficiency of the LSC is the product of the efficiency of every described process[13]

$$\eta_{LSC} = \int \big(1 - e^{-\alpha_C(\lambda)\cdot d}\big)\big(1 - R(\lambda)\big)\, \Phi_{PL}\big(1 - \eta_{RA}(\lambda)\big)\cdot$$

$$\big(e^{-\alpha_{WG}(\lambda)\cdot L}\big)\big(1 - \eta_S(\lambda)\big)\, \eta_{WG} d\lambda$$

This equation takes into account all the processes taking place into the LSC, but in order to complete the photon to electron conversion, also the coupling with the PV cells on LSCs edges must be considered. Conversion of light into current relies on the PV attached to the edge of the device. The choice of the solar cell is

made with the purpose of maximizing the conversion of photons reaching the PV cell: emission band under 1000 nm (1,1 eV) can be efficiently converted by Si-based PV devices, whereas if the luminescence of the chromophore is centred in a higher wavelength, the necessity of GaAs cell use arises. Apart from conversion, it is also important to connect the PV system to the LSC through a material with proper refraction index, the so-called index-matcher. The use of index-matching interlayer material reduces the amplitude of critical angle for total internal reflection. Otherwise a portion of radiation carried to PV cell could experience the total internal reflection on the edge surface and could be reflected backwards inside the slab. In fig 1.5 all the processes above descripted are finally illustrated

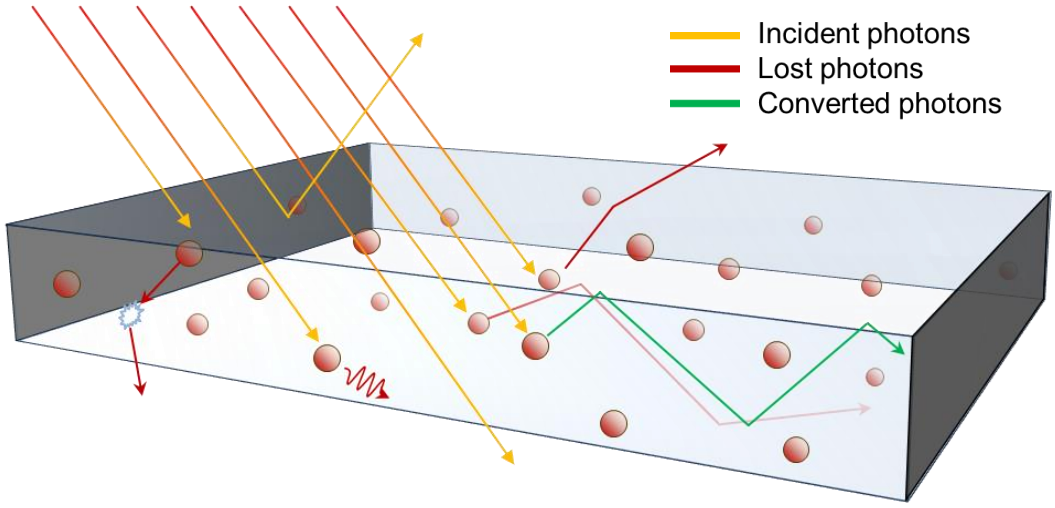

Figure 1. 5 : Illustration of all the processes involved in a LSC. Yellow arrows indicate incident sunlight, red arrows indicate photons absorbed and emitted by chromophores which are lost due to various loss processes and green arrows indicate photons correctly absorbed, emittend and converted.

1.1.4. Chromophores for LSCs

Organic and Organo-metallic Dyes

For many years since their first architecture reference in 1973 by Lerner, the major limitation of this technology has been represented by the difficulty in realizing chromophores species able to fulfil the above mentioned requisites. Initially, the research about chromophores for LSCs focused on organic small molecules or polymers[5, 24, 25, 35, 36]. However, these classes of materials typically exhibit narrow absorption profiles, limiting the solar spectrum coverage, and thus intrinsically the device efficiency.

One approach in order to broaden the absorption profile to the near infrared region is to extend the conjugation length of chromophores. However this strategy typically presents the drawback of progressively decreasing the emission efficiency[37]. Moreover, organic materials usually show a marked overlap between absorbance and luminescence spectra profile (moderate Stokes Shift), since these processes both involve the same molecular orbitals, the HOMO and the LUMO of the chromophores. This overlap causes a strong self-absorption, whose effects on device performances have been discussed above.

In order to overcome self-absorption losses, organo-metallic compounds presenting large Stokes Shift were adopted[26, 38]. In such metal complexes, the absorbance and emission features are assigned to different parts of the system, involving different initial and final energy levels. Light is absorbed by the high-absorbing organic ligands and then the excitation is efficiently transferred to the rare-earth element, where recombination occurs via a spin-forbidden transition[38]. Despite this strategy ensures the suppression of reabsorption losses using an appropriate ligand heavy-metal couple, LSCs based on these materials still suffer from low efficiency caused by a poor solar light collection. The absorbance profile of the chromophores is determined solely by the organic ligands and thus it typically extend only in the UV part of solar spectrum[29].

Recently, Stokes-shift-engineered quantum dots (QDs) have allowed to overcome these limitations. Similarly to organo-metallic compounds, these systems are designed to decouple their absorption and emission functions, a feature which can be obtained by using QDs with hetero-structure (CdSe/CdS or PbS/CdS)[29, 39-41], electronic doped II-VI QDs with Mn or Cu [31, 42], or ternary I-III-VI_2 QDs ($CuInS_2$ or $CuInSe_2$)[15, 19, 43].

In hetero-structured QDs a thick shell of high band gap semiconductor determines the absorption, which can be tuned by controlling the shell size, while a low-band gap semiconductor core provides emission. In electronic doped QDs and in ternary QDs absorption is dominated by host semiconductor band to band transition, while emission at lower energy occurs involving an intra-gap state associated to the doping element, in II-VI doped QDs, or to a native defect, in I-II-VI QDs. Stokes Shift-engineered QDs allow the device to extend its absorption to the red fraction of visible light, thus exploiting the whole visible fraction of the solar spectrum, while emission occurs at IR frequencies[19]. With this class of material used as chromophores, the first example of large area LSC with reduced self-absorption losses was realized, which exhibited a 3.24% record efficiency with active area of 150 cm^2 [15]. However, frequently hetero-structured QDs contain one or several elements with relatively low earth-abundance or already heavily used in existing mass-production technologies, which turns out to be one of the major large-scale production limit for LSCs technology based on these emitters.

Moreover, this kind of devices still suffers from a marked dimension-dependent efficiency, mainly caused by a matrix-related loss process. As a matter of fact, the absorbance profile of hosting materials show features due to the overtones of C-H and C-O bonds vibrational modes in the spectral region of infrared QDs emission, resulting in detrimental losses in LSC performance[32]. However the narrowing of emission bands of infrared QDs is not a viable strategy since such chromophores exhibit intrinsically broad emission profiles.

The width of their emission profiles depends on the local dispersion of defect states (dopant or native) responsible for optical transition, a feature which is not controllable through the synthesis. In order to obtain high performance LSCs with commercially interesting dimensions (2500 cm^2), the dimensions-dependence of their efficiency has to be overcome with the development of novel chromophores.

2. LSCs based on silicon quantum dots

2.1. Abstract

In this section of my thesis I studied the application of silicon Quantum Dots (Si-QDs) as novel chromophores in luminescent solar concentrators (LSCs). The use of these indirect-bandgap semiconductor nanostructures overcomes the limitations in terms of industrial scaling which is characterizing the QDs so far used in LSC application[15, 23, 44, 45]. Non-toxicity, low cost of the raw material and ultra-abundancy on earth crust make Si-QDs a promising chromophore species for large scale production of LSCs. Moreover, if their dimensions are properly engineered through nanoscale confinement, Si-QDs show ideal optical features to obtain high efficiency devices.

The size shrinkage significantly modifies their optical properties compared to bulk material, resulting in a large separation between absorption and emission profiles and a high quantum efficiency. The high optical quality of the nanocomposite combined with the chromophores optical properties results in an almost ideal LSC in which the losses related to photo-luminescence self-

absorption and scattering, typically the two most important efficiency-limiting factors in LSC, are strongly reduced. In the end, I demonstrate that similar characteristics can be achieved also in flexible Si-QDs-based LSCs, which allow the application of such devices in a wider range of architectural elements, but still preserve the efficiency and the optical properties of classical flat concentrators.

2.2. Materials

Si-based Quantum Dots

One interesting material design concept for achieving reabsorption-free LSC that is yet to be explored, is the use of semiconductor quantum dots which present an indirect optical transition, such as silicon. Moreover, from a scaling-up production point of view, there would be no limitations in large scale production of quantum dots based on Si, since it represents by far the most abundant element in the Earth crust[46, 47], and only a small percentage of its yearly production is sufficient to sustain the demand from the semiconductor and solar energy sectors. The unmatched availability of these raw materials, as shown in fig 2.1, could thus help avoiding the issues that affect the applicability of other existing types of Stokes-shift engineered quantum dots to large-scale LSC fabrication.

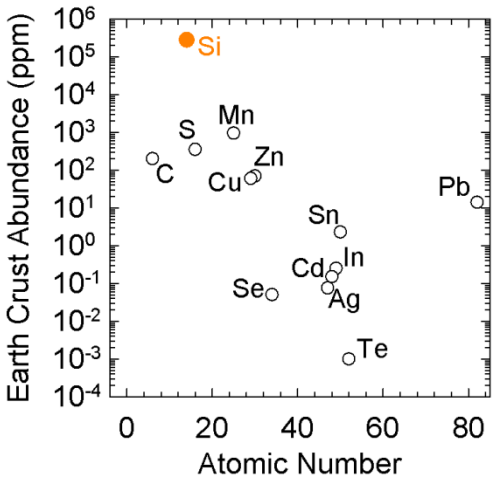

Figure 2.1:Earth crust abundance of materials typically used for the production of QDs.

The quantum confinement dramatically changes the optical properties of this material, otherwise not exploitable for LSC application. As a matter of fact, bulk silicon presents a very low transition probability and thus low luminescence because of its indirect band gap: the $X_{CB} \rightarrow \Gamma_{VB}$ transition requires the presence of transverse phonons to happen, resulting in a low transition probability (band-edge absorption atomic cross-section of $\sigma \approx 1 \cdot 10^{-22}$ cm^{-2}). However, when silicon is spatially confined below the diameter of Bohr exciton (8.6 nm)[48-50], its nanostructures present high luminescence owing to a partial relaxation of the selection rules for momentum conservation, which provides a small oscillator strength to the band-edge electronic transition[51-53].

It has been recently demonstrated that quantum confinement alters the per atom cross-section, enhancing it of almost one order of magnitude between 2 and 3 eV with respect to the bulk material[50]. As a result, optical absorption and emission of Si-QDs can be finely tuned from the visible to NIR spectral region by controlling their size while their quantum efficiency can be enhanced over 50% by passivating the Si-QDs surfaces[52, 54, 55] which typically generate an efficient non-radiative decay mechanism. Finally, a very important aspect for application in LSCs, Si-QDs still present an absorption edge with the very small absorption coefficient typical of indirect-bandgap semiconductor, resulting in high Stokes shift and thus negligible self-absorption capability[56, 57].

2.3. Results

2.3.1. Si-QDs Optical characterization

The first step of this study is to verify if the chosen Si-QDs properly fulfil the required optical features necessary to obtain high efficiency LSCs. Absorption and steady state luminescence of Si-QDs in a toluene solution were measured and are reported in fig 2.2. The solution concentration was chosen to mimic the desired optical absorbance of the final device, whose thickness is already fixed in 0.26 cm, following a previously tested device assembly protocol.

The absorption spectrum shows a typical profile of an indirect gap semiconductor[58] and there are no evidences of scattering components, indicating that the Si-QDs can be efficiently dissolved in organic solvents. Si-QDs absorbance is also reported together with the solar spectral irradiance, highlighting with the shadowed area the fraction of absorbed solar light, in order to verify if such chromophores exhibit a full exploitation of solar spectrum across a wide range of visible wavelength.

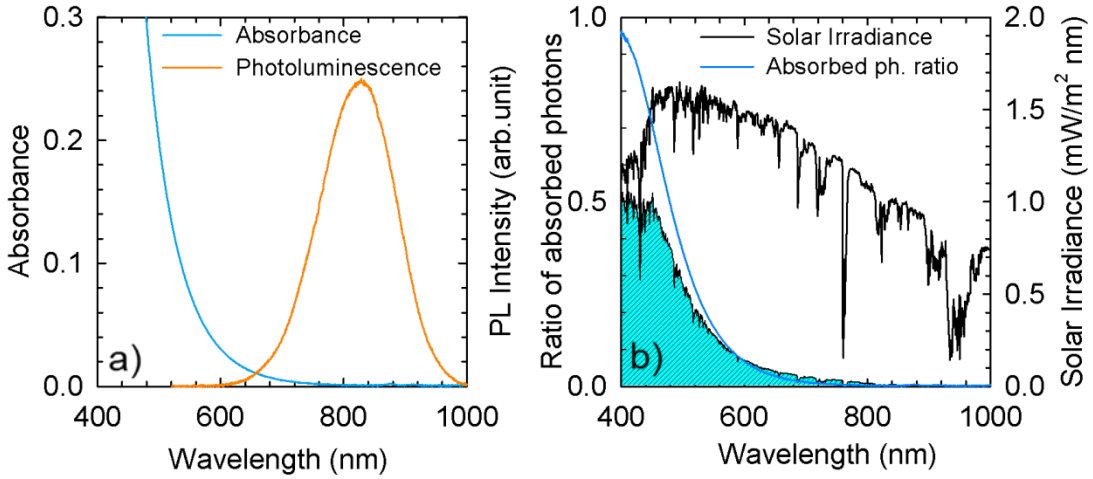

Figure 2.2.: a) Absorbance and photoluminescence of Si-QDs used in this study in toluene solution (exc. @ 473 nm); b) absorbed/incident photons ratio and fraction of solar radiation absorbed (light blue area).

This aspect plays an important role both for functional and aesthetic reasons: the collection of photons from a wide wavelength window is fundamental to obtain high efficiencies while maintaining a neutral colour of the device which does not preclude the installation in the urban context[15, 35, 59]. The photoluminescence is peaked at 835 nm, a feature which ensures minimal reabsorption losses thanks to the high "effective" Stokes Shift and in its turn does not alter the external hue of the device, since such wavelength range is invisible to human eye.

Here above, I referred to "effective" Stokes Shift because in Si-QDs the transition which generates photo luminescence ($X_{CB} \rightarrow \Gamma_{VB}$) is the same also for a possible absorption transition ($\Gamma_{VB} \rightarrow X_{CB}$), which would result in a real Stokes

Shift of zero[56, 60]. However, the $\Gamma_{VB} \rightarrow X_{CB}$ transition is partially forbidden and thus the absorption coefficient of Si-QDs above 630 nm is limited below 0.1 cm^{-1} at the Si-QDs concentration employed in LSC application, resulting in an "effective" Stokes Shift of 400 meV. As far as emission is concerned, the charges collected by photon absorption via all the other possible VB → CB can be efficiently re-emitted from the conduction band minimum (X_{CB}) from which the transition is possible thanks to a relaxation of selection rules which produces a small, but yet not negligible, oscillator strength[58, 61]. This feature is visible from fig. 2.3.

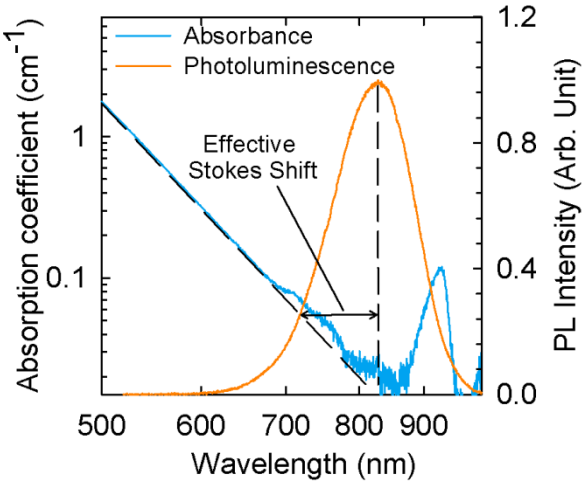

Figure 2.3: Absoption coefficient and emission spectrum of Si-QDs in toluene solution at the same concentration of that used in the device, reported in logaritmic scale to enahnce the comparison between real Stokes Shift (absorption coefficient below 0.1 cm^{-1} above 680 nm) and "effective" Stokes Shift.

It is not unusual that the insertion of luminescent species inside a polymer obtained through radical polymerization induces detrimental modification in the optical features of the QDs[15, 29], an aspect which needs to be taken into consideration particularly for the fabrication of high efficiency LSCs. To probe the stability of Si-QDs to the radical polymerization of the matrix, the same spectroscopic studies performed on QDs in solution were reproduced on the nano-composites. The optical absorption and photoluminescence spectra are depicted in fig 2.4a and b, which shows no modification in spectral properties for the Si-QDs in solution and in polymeric matrix. The two small features of

absorption spectrum at 927 nm and 1040 nm are relative to the vibrational overtone of the CH stretching mode bond of the matrix [32].

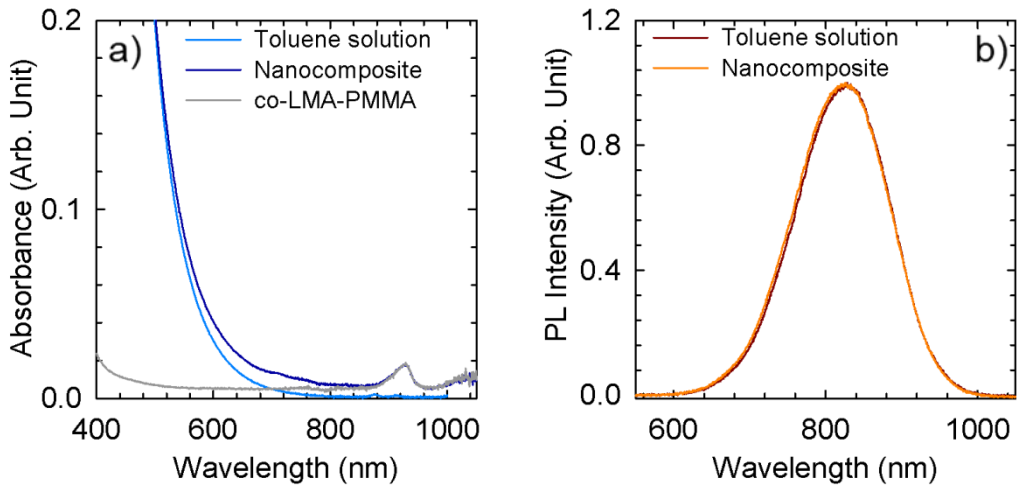

Figure 2.4.:a) Absorbance spectra of Si-QDs in toluene solution, Si-QDs in the polymerized matrix and absorbance of the matrix without QDs: b) photoluminescence spectra of Si-QDs in toluene solution and in the polymerized matrix.

This is confirmed by the absorption spectrum of a slab of pure co-PLMA-EGDM with same thickness of LSC, which shows the same features. It is interesting to point out that the Si-QDs photoluminescence almost perfectly matches the transparency window arising from the combination of the absorbance of Si-QDs with the absorbance of the matrix. This peculiar feature ensures both minimal reabsorption with the chromophores themselves and minimal matrix-related reabsorption losses for large area devices, as shown in the following.

Also time resolved luminescence was collected for the Si-QDs in solution and in the nano-composite and reported in fig 2.5. The time-resolved luminescence traces reveal a similar emission dynamics for the two systems, with a weak-acceleration for the Si-QDs in the polymer matrix, probably due to an activation of non-radiative decay channels related to interactions between Si-QDs non-passivated surfaces and the polymeric chains.

Such hypothesis is also confirmed by the small reduction of emission efficiency going from toluene solution ($\phi_{PL}^{Tol} = 50\%$) to the polymeric matrix

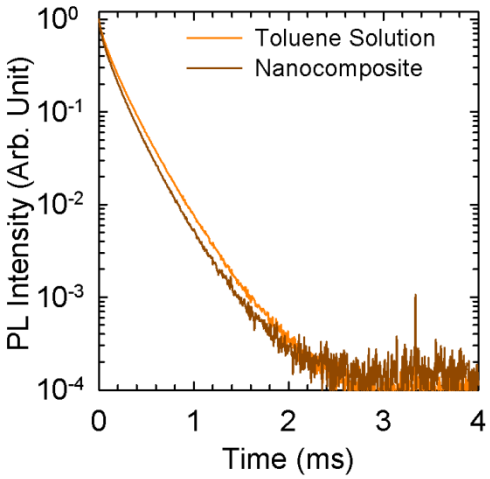

Figure 2.5.: Time resolved photoluminescence of Si-QDs in solution and in the polymerized matrix.

($\phi_{PL}^{Mat} = 46\%$). A reduction in the order of 10% is a remarkable result considering both the exposure to ultra-violet light in presence of radicalic initiator species during the polymerization and the absence of any additional protective coating on the Si-QDs.

2.3.2. LSCs efficiency

The efficiency of a 144 cm^2 (12x12 cm^2 x0.26 cm thickness, photos in fig 2.6) LSC was calculated by coupling the four edges with calibrated silicon solar cells using an index-matching gel and perpendicularly illuminating the LSC with a calibrated solar simulator in standard conditions (AM 1.5G 100 mW/cm^2). The experiment was performed in conditions which could simulate the use of LSC in real contest, thus no back reflectors were placed at the bottom of the waveguide. A power conversion efficiency of $\eta = 2.85 \pm 0.15\%$ was calculated as $\eta = P_{OUT}/P_{IN}$ where P_{OUT} is the luminous power collected by the solar cells coupled to the LSC perimeter, while P_{IN} is the incident solar power on the LSC surface. This result is particularly relevant considering the high transparency of the device across the visible spectrum, the lateral size of the device and the fact that Si-QDs present a non-optimized quantum efficiency (46%).

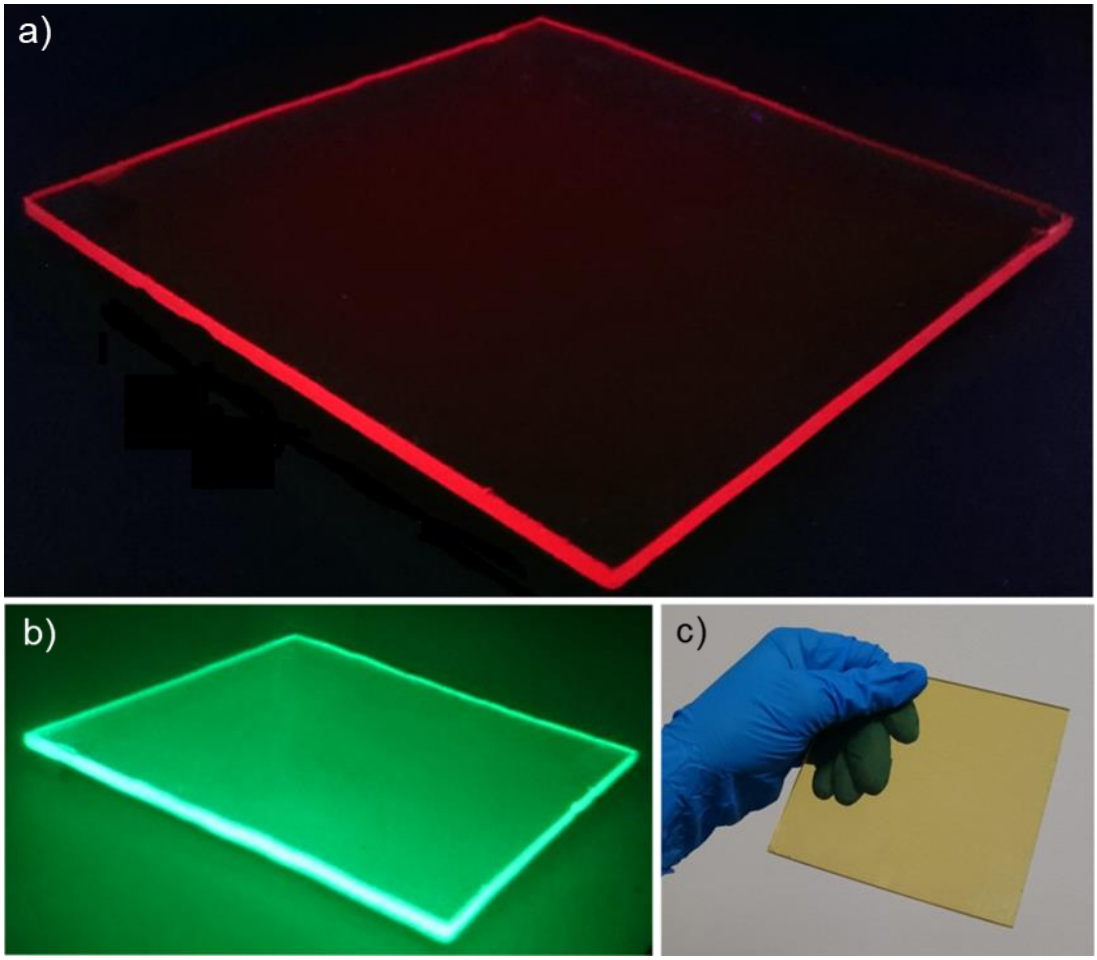

Figure 2.6: a) Photo of the LSC under UV illumiation collected with a visible camera through a UV filter; b) photo of the LSC under UV illumiation collected with a infrared camera; c) photo of the LSC under indoor light. It is worth highlight how the luminescence of Si-QDs is mainly emitted from the edges (clear in photos a and b).

The optical quantum efficiency of the device, expressed as $\eta_O = N_{OUT}^{ph}/N_{ABS}^{ph}$ where N_{OUT}^{ph} is the number of photons collected from the LSC edges and N_{ABS}^{ph} is the number of total absorbed photons, is $\eta_O = 30\pm4\%$. This value is in good agreement with the theoretical value $\eta_O^{TH} = 35\pm6\%$, which was calculated considering also the scattering, re-absorption and transport efficiency as $\eta_O^{TH} = \Phi_{PL}\cdot\eta_{TR}\cdot(1-\eta_{RA})\cdot(1-\eta_S)$.

A second efficiency measurement was performed using a back reflector, a semi-transparent layer which helps the recycling of the photons not absorbed by the chromophores or escaping from the back of the waveguide. In this case an aluminium coated silica surface with >95% reflectivity was used as back

reflector, obtaining an efficiency of $\eta = 4.0 \pm 0.2\%$ but still preserving a degree of transparency suitable for application as semi-transparent windows.

2.3.3. Si-QDs LSC Scattering evaluation

Scattering phenomena can play an important role in limiting the efficiency of large area LSCs. As a matter of fact, the randomization of the path of emitted light due to scattering results in an enhanced probability of escaping through the large area surfaces of LSC instead of being concentrated on the slab edges, as schematically reported in fig 2.7.

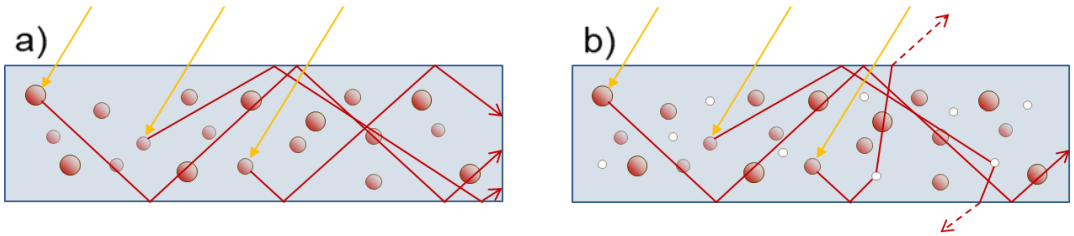

Figure 2.7.:Working mechanisms of a LSC non affected (a) and affected (b) by scattering losses. Si-QDs are depicted as red dots, scattering centres are depicted as white dots.

The evaluation of scattering losses is necessary to define the optical quality of the nano-composite. The evaluation of scattering effect can be performed by measuring the fraction of the emitted photons which escapes through the large area surfaces. In absence of scattering, the luminescence escaping from the device surfaces is solely determined by the waveguide efficiency of the slab; otherwise, if scattering losses are not negligible, the fraction of PL lost through the surfaces should exceed this theoretical calculation. The measurement was performed exciting with a c.w. laser and collecting the PL emitted from the device with an integrating sphere (see the scheme in fig 2.8c). In order to distinguish between the light correctly emitted through the edges from the light scattered and lost through the large area surfaces, the PL measurement was performed in two different configurations, showed in fig. 2.8: d) with blackened edges and e) with clear edges.

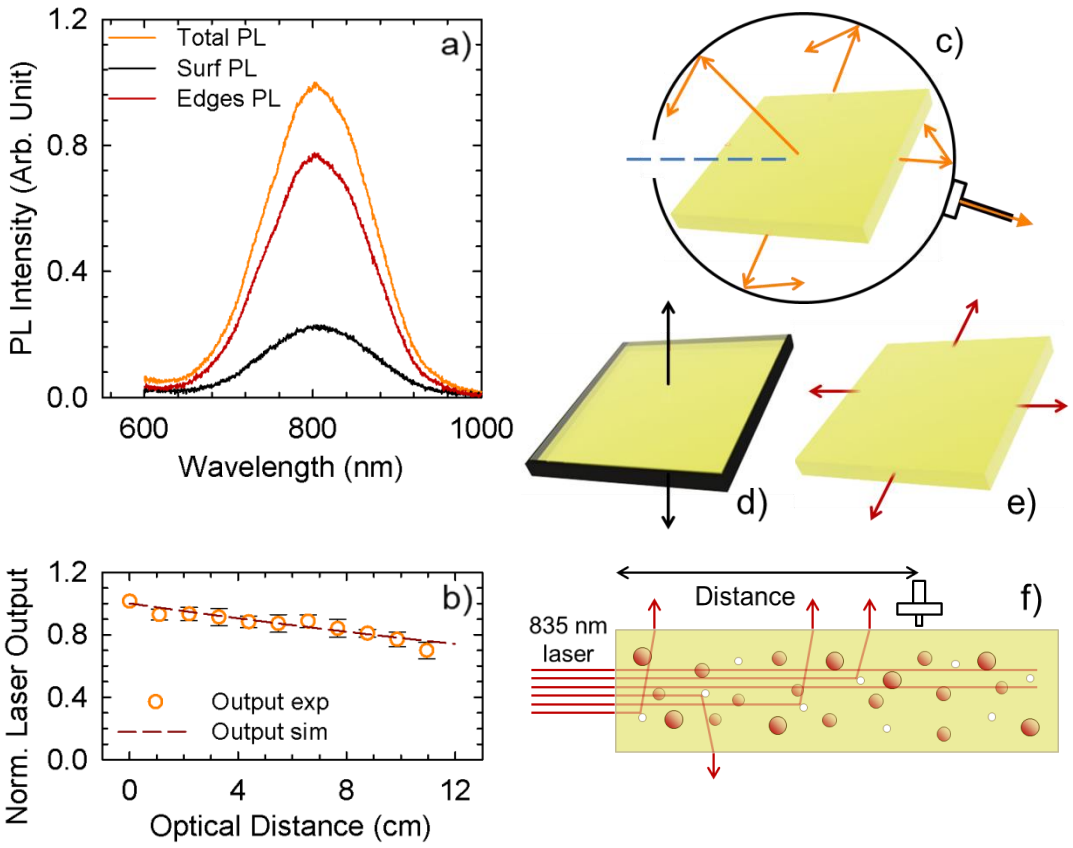

Figure 2.8.: a) Photoluminescence spectra collected with a integrating sphere with the setup depicted in (c) for a device with blackened edges (config. d) and without blackened edges (config. e). Orange lines refer to total PL (orange arrows in (c)), black line to PL emitted from surfaces (black arrows in config. (d)) and red line to PL emitted from edges (red arrows in (e)); b) plot of the intensity of a 835 nm laser intensity output collected from the surface as a function of distance travelled inside the device (config. f).

The comparison between these PL measurements revealed that only 25% of total PL is escaping from the faces of LSC (calculated from configuration d), while 75% is correctly concentrated on the edges (calculated from the difference of configuration d) and e)). This result is in great accordance with the theoretical waveguide efficiency of the device which is calculated considering the refractive index of the copolymer matrix n through the Snell law as $\eta_{WG} = (1 - 1/n^2)^{1/2} = 0.741$, revealing that the device does not suffer from losses induced by scattering phenomena.

To evaluate in an even more accurate way the scattering losses, a light propagation measurement was performed. A laser source with emission close to Si-QDs PL peak wavelength (835 nm) is directed perpendicular to one slab edge,

which simulates the propagation of the light emitted from the chromophores inside the matrix. In this configuration, laser light travels parallel to the surfaces, thus the light lost through the surface is caused only by scattering phenomena. Light escaping from LSC surface is collected as a function of the source-collector distance, as shown in fig 2.8f. The choice of this configuration and of a laser light with emission wavelength centred in the transparency window of the device avoids to account two contributions which could alter the scattering evaluation. The first is due to the slab surfaces roughness, which could randomize the incident light path direction if laser hits the slab surfaces. The second arises from the small, but yet not negligible, re-absorbance of the higher energy fraction of Si-QDs PL. The re-absorbed photons are indeed isotropically re-emitted and a fraction of them (25.9%) passes through LSC surfaces and would be wrongly accounted as scattering.

This measurement revealed that light scattered from the surfaces represents only 0.06% of input light per centimetre, confirming that in this kind of device scattering losses are definitely negligible. The decreasing of laser light intensity with the distance from the source is an effect due to the non-zero absorption of the nano-composite at 835 nm. As a matter of fact, experimental data are perfectly consistent with the trend calculated with Lambert-Bier equation for linear propagation of light along the waveguide using the absorption coefficient of the nano-composite, as reported in fig 2.8 b.

2.3.4. Reabsorption losses

The evaluation of re-absorbance was performed by measuring the photoluminescence spectrum varying the distance between the excitation spot and the slab edge (surface of 3.12 cm^2) where the luminescence is collected (the measurement set-up is depicted in fig 2.9e). In Figure 2.9a the absorption spectra of the device and the photoluminescence spectra of the LSC collected with 0 and 12 cm distance between laser pump and edge are reported.

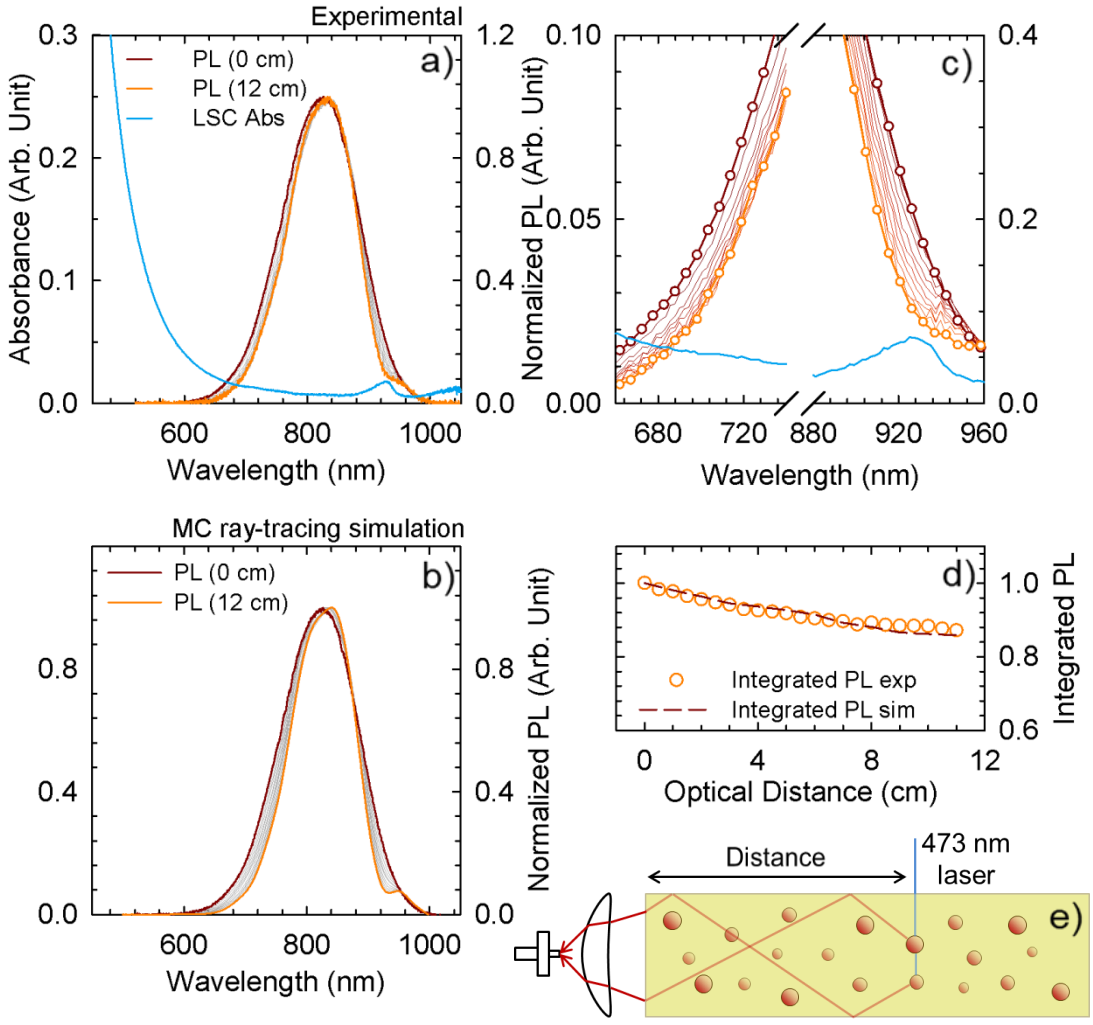

Figure 2.9.: Experimental (a) and simulated (b) normalized photoluminescence spectra as a function of distance between the excitation spot and the collection edges; c) enlargment of PL spectra shown in a) to highlight the simmetrical narrowing of PL; d) integratel experimental and simulated PL as a function of excitation-collection distance; e) scheme of the experimental setu-up.

The experimental data are in perfect agreement with the Monte Carlo ray-tracing simulation reported in fig 2.9b, which was calculated using the same absorption/emission profile (reported in fig. 2.4 a and b) and photoluminescence efficiency ($\phi_{PL} = 46\%$) of the Si-QDs in the nano-composite. The variation of the source-collection distances induces also a modification of the solid angle subtended to the collection. The measured PL spectra were normalized to their maximum value in order to highlight possible variation in their profile, since re-absorbance may induce a non-homogeneous modification of PL profile. The normalized photoluminescence profiles collected at 12 cm from the excitation spot (orange curve) show only a slight symmetrical narrowing compared to the photoluminescence collected directly at the slab edge (dark red curve).

The narrowing of the spectra at high wavelength is due to the presence of the C-H bond vibrational overtones at 927 nm, while at low wavelength it is due to the residual, yet not negligible, re-absorption of the Si-QDs (fig 2.9c). Such similar contributions to the narrowing of photoluminescence profile demonstrates that the loss due to reabsorption is heavily reduced and that the exploited Si-QDs represent an appropriate emissive species with a luminescence which perfectly matches the transparency window of the polymeric matrix.

From the collected photoluminescence spectra as a function of excitation/collection distance, it is possible to evaluate the losses exclusively due to reabsorption phenomena. To do such evaluation, the different geometries related to the different excitation/collection distances have to be taken into account. In particular, the solid angle subtended from the excitation spot when luminescence is collected from one edge varies with the distance and thus, for a correct evaluation of the reabsorption losses, the PL profiles have to be normalized for the subtended solid angle.

The integrated photo-luminescence after normalization as a function of the excitation distance is reported in fig 2.9d. The data show a very small drop (~13%) in 12 cm which is consistent with the theoretical expectation, as

reported in fig 2.9d, representing a further confirmation of what found in the quantitative photoluminescence measurements in fig. 2.8 a. As a matter of fact, 25% of photoluminescence escaping from the LSC surfaces, almost identical to the theoretical wave guide efficiency of the matrix, indicates that there are no contributions by reabsorption/emission or scattering phenomena to this loss mechanism.

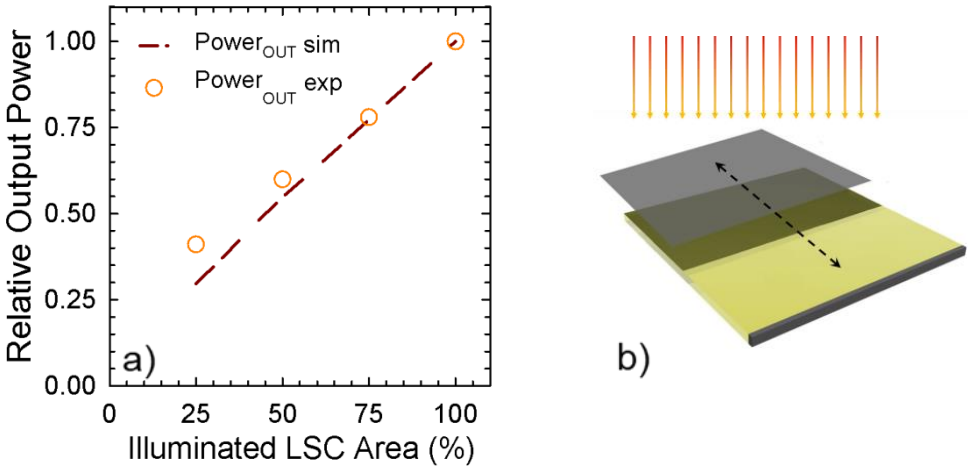

Figure 2.10: a) Power extracted from an edge as a function of the fraction of LSC illuminated area; b) set up of the experimental measurements.

The limitation of the randomization of the light propagation direction through reabsorption suppression combined with the optical high quality of the matrix, which prevents scattering phenomena, leads to the ideal situation in which all portions of the device area equally contribute to the total power output of LSC. Fig. 2.10 shows the output power collected from one of the LSC edges (12×0.3 cm^2) measured with the same set-up adopted for the measurements of η described above (single edge coupling to the photodiodes and no back-reflector), but in this case the portion of the area exposed to illumination under solar simulator is progressively increased. The theoretical trend calculated through Monte Carlo ray tracing is also reported in the figure, which reveals a very good agreement with experimental data, underscoring the fact that the fabricated nano-composite is very close to an ideal LSC device.

The simulation was performed considering a device unaffected by scattering or reabsorption losses, embedding a chromophores species with same optical features of the Si-QDs, in which the light power collected at the edges is therefore determined solely by the numeric opening of the illuminated area of the device. The output measured by illuminating the quarter surface of the device closer to the edge is slightly larger than the theoretical prediction, which is in agreement with the narrowing of the spectral linewidth already commented. As a matter of fact, the photoluminescence collected in this device section includes emitted photons which do not experience reabsorption or scattering due to the short path inside before reaching the edge.

2.3.5. Monte Carlo ray tracing simulations

The very good agreement between the calculated optical power conversion by Monte Carlo ray-tracing simulation ($\eta_{CALC} = 2.67 \pm 0.17\%$) and the measured value of $\eta = 2.85 \pm 0.15\%$ on the assembled device allows to use the optical parameters of the fabricated device (absorption and luminescence spectra and ϕ_{PL}) to estimate its achievable potential by modifying its geometric dimensions, respectively area and thickness (reported in fig 2.11).

To estimate the ultimate device performances achievable using these LSCs, a second simulation in which the emission efficiency of the Si quantum dots reaches the fully optimized value $\phi_{PL} = 100\%$ was performed. In this regard, I highlight that a recent study by Linnros and co-workers[62] has made a critical step towards this fundamental milestone for LSC technology, by reporting colloidal Si quantum dot ensembles with external $\phi_{PL} = 70\%$, which is among the highest efficiencies reported for Stokes shift engineered quantum dots emitting in the NIR spectral region[15, 39].

The calculation (orange surfaces) indicates that, with QDs used in this work, an efficiency as high as $\eta \geq 6\%$ would be achieved in a $1 m^2$ LSC by increasing the LSC thickness to 2 cm considering the same Si-QDs concentration. In the

same geometry, using Si-QDs with optimized emission (100%), the LSC would exhibit an impressive $\eta = 15\%$. However, this remarkable result implies that

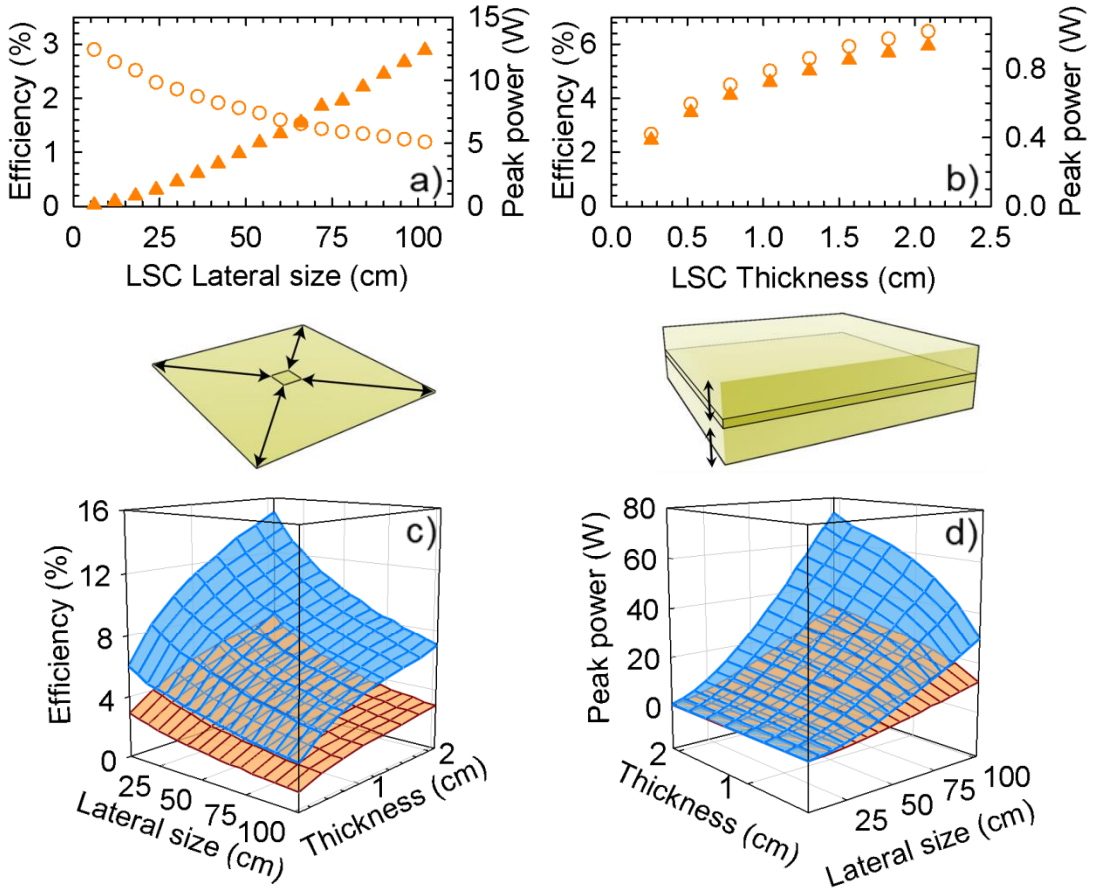

Figure 2.11: a), b) Theoretical trends of η (empty circles) and peak power (filled triangles) for square LSCs with experimental thickness (0.26 cm) and increasing lateral size (a) and with experimental lateral size (12x12 cm^2) and increasing thickness (b); c), d): 3D plot of optical power efficiency and peak power output (at AM 1.5 irradiance) calculated through Monte Carlo simulations. Orange plots ferer to Si-QDs usedin this work, blue plots refer to optimized Si-QDs with 100% emission efficiency.

the device transparency is strongly reduced corresponding to a 35% of transparency in the visible spectral region.

An LSC preserving the same thickness as experimental measurement (0.26 cm) and lateral size of 1 meter still shows an efficiency of 1.18% with non-optimized Si-QDs, and 2.87% with Si-QDs with 100% emission efficiency, but preserving high transparency in the visible region of the spectrum. Interestingly, if the fabricated device is compared with the device containing the fully optimized Si-QDs, the LSC performance are enhanced by slightly more than

a factor two, as expected by increasing the emission efficiency from 46% to 100%: this effect is a further confirmation of the effectiveness of the mitigation of the, yet small, reabsorption losses.

2.3.6. Flexible device

Finally I tested the potentiality of Si-QDs-based LSC as curve of flexible energy conversion element[42, 63]. For this purpose, a rectangular LSC (4.5×20 cm^2) doped with Si quantum dots (0.09 wt%) following the same procedure used for the rigid devices was assembled. However, to ensure a high degree of flexibility to the matrix structure, the, a monomer:crosslinker P(LMA-co-EGDM) ratio was modified to 90:10% w t/wt, (from 80:20% wt/wt of the original squared LSC). The variation in the matrix composition yielded a flexible waveguide that can be easily bent from flat to semi-cylindrical configurations.

Fig. 2.12a and b reports two sets of images of the LSC with increasing bending under ultraviolet illumination collected with ultra-violet filtered visible photocamera and ultra-violet filtered infrared camera. From both sets of pictures it is evident that the output photoluminescence is primarily emitted from LSC edges, highlighting the good optical quality of the flexible device. In order to experimentally verify the effect of slab curvature on the waveguiding properties of the LSC, the photoluminescence collected from the 4.5x0.26 cm^2 edge was measured as a function of the distance from the excitation. The same measurement was repeated for increasing LSC curvatures, quantified by the amplitude of the central angle θ, being θ=0° the configuration of a flat LSC and θ=180° the configuration in which the device presents an arch-like shape.

For every measurement, using the experimental device parameters (dimensions, absorption and luminescence profiles and quantum efficiency), a Monte Carlo ray tracing simulation was also performed in order to compare experimental results with theoretical trends.

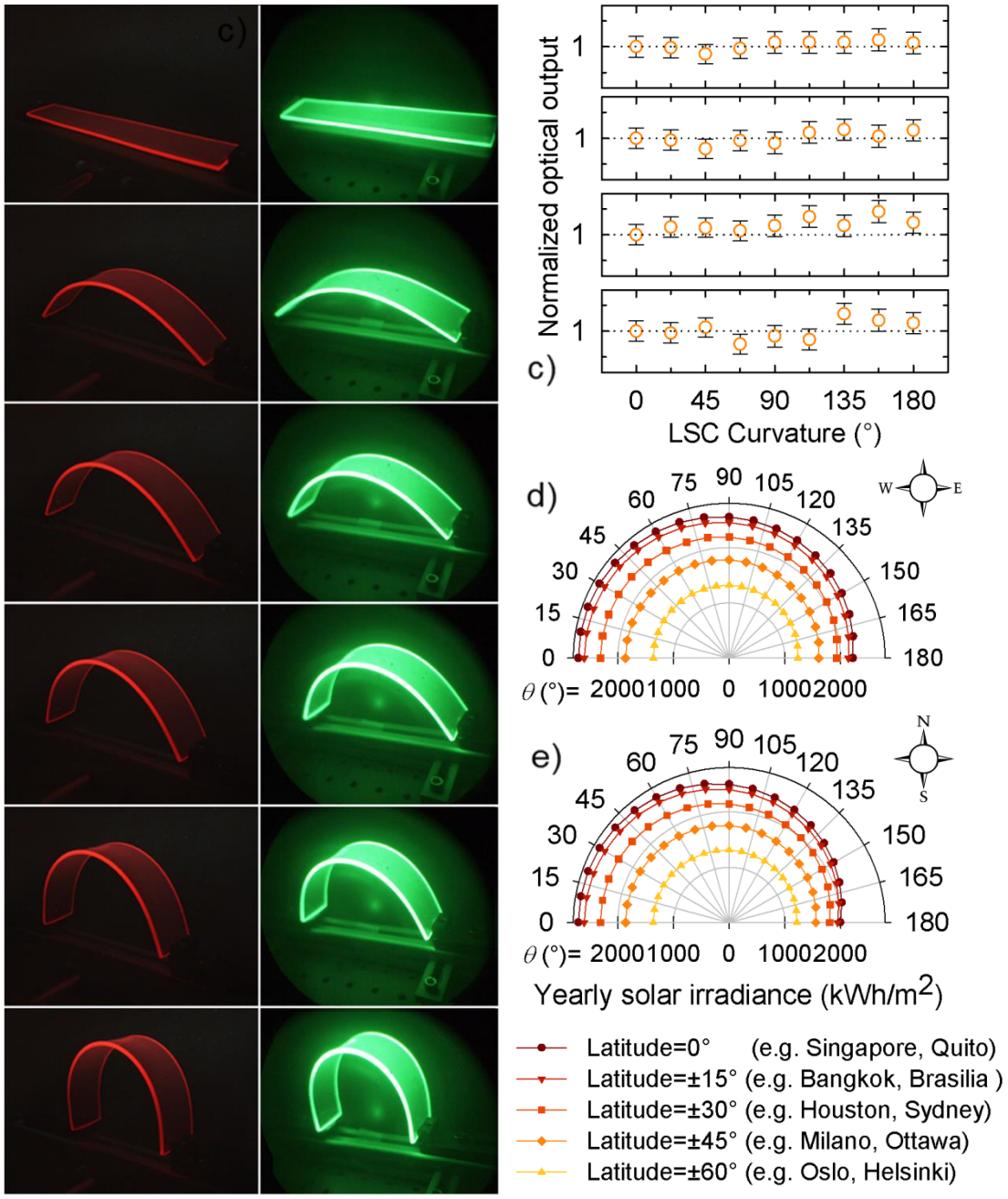

Figure 2.12.: Photographs of a flexible Si-QDs based LSC (dimensions of 4.5 cm × 20 cm × 0.26 cm) under ultraviolet illumination taken with an ultraviolet-filtered visible camera (a) and an ultraviolet-filtered infrared camera (b). c, Optical output as a function of device curvature expressed in terms of the central angle θ for increasing optical distance d between the excitation spot and the slab edge from where the signal is collected. Data are normalized for the intensity at
θ = 0; d) Total yearly solar irradiance in kWh per square meter as a function of θ for a curved LSC in east–west orientation (azimuth angle) at different latitudes (representative geographic locations are reported in correspondence to each latitude); e) The same plot for a device in south–north orientation.

The photoluminescence spectra collected at the same excitation-collection distances (5, 10, 15 and 20 cm respectively) for progressively increased θ were normalized for the photoluminescence collected at the same distance from the device in the θ=0 configuration and are reported in fig 2.12c. The results of these measurements show an essential constant output for every θ, which suggests that the waveguiding properties of LSC are unaffected by the LSC curvature.

This invariance of the transport properties for different configuration of the device suggests that flexible LSCs could find an application also as semi-transparent architectural elements windows with complex curvature without the drawback of incurring in optical losses due to a reduction in photon transport property.

Such an expanded building integration capability can be achieved with minimal losses in terms of yearly production of PV electricity with respect to a horizontal flat device. This effect is shown in Fig. 2.12d,e, where I reported the total annual solar irradiance in kWh per square metre as a function of θ for a curved LSC in south–north or east–west orientation (azimuth angle). The largest effect is observed at the lowest latitudes, where the maximum drop in the yearly irradiance for a curved LSC with respect to a horizontal device (θ = 180° versus θ = 0°) ranges between 20 and 25% depending on the orientation. The drop decreases gradually to ~10% with increasing latitudes up to 60°.

2.4. Conclusions

I realized the first example of a LSC based on indirect bandgap colloidal quantum dots exclusively composed of ultra-abundant earth materials. With this new approach I overcome the low-availability limitation of elements used in high-performing hetero-structured QDs and subsequently I demonstrate the suitability of silicon based nanostructures as chromophores for high efficiency LSCs. The device was assembled by incorporating the Si-QDs into a mass polymerized acrylic matrix which resulted in a high-optical-quality waveguide. Owing to the large effective spectral separation between the optical absorption and luminescence spectra of the quantum dots, the LSCs are essentially unaffected by optical losses due to reabsorption of the guided luminescence. As a result, the fabricated devices exhibit power conversion efficiencies as high as 2.85% (corresponding to an optical quantum efficiency of 30%), despite their large area (144 cm_2) and high degree of transparency across the visible spectrum (70% transmittance), which makes them good candidates for the realization of BIPV elements such as PV windows.

The assembled LSC behaves as a nearly ideal device, in which all portions of the illuminated surface contribute equally to the total power output. Monte Carlo ray-tracing simulations enabled us to model the optical performances of the LSCs increasing lateral dimensions and slab thickness. Self-standing flexible LSCs were also fabricated and tested with the aim of evaluating the effects of bending on the waveguiding properties and thus to assess the suitability of such devices for the realization of PV-active architectural elements of complex curvature. Light propagation experiments together with numerical modelling data indicate that the LSC performances are independent on device curvature, similar to what is observed with plastic optical fibres. These results extend the building integration ability of LSCs.

2.5. Materials and Methods

2.5.1. Materials

Lauryl methacrylate (LMA, 99%, Aldrich) and ethylene glycol dimethacrylate (EGDM, 98%, Aldrich), purified with basic activated alumina (Sigma-Aldrich), were used as monomers for the preparation of polymeric nanocomposites. IRGACURE 651 (BASF) was used as a photo-initiator without purification.

2.5.2. Si-QDs Synthesis

The Si quantum dots used in this study were synthesized following the procedure reported in ref.[64]. Briefly, argon (30 s.c.c.m.) and 5% silane in helium (14 s.c.c.m.) were upassed through the length of a borosilicate glass tube reactor with hydrogen injected into the afterglow (100 s.c.c.m.). A nominal power of 45 W at 13.56 MHz was applied via copper ring electrodes placed 4 cm before the afterglow region, where the inner tube diameter expanded from 0.5 to 2 cm. Pressure in the afterglow region was maintained at 1.4 torr by an adjustable orifice downstream of the plasma, after which the hydrogen-passivated Si quantum dots were collected by inertial impaction on glass substrates.

These quantum dots underwent hydrosilylation in oxygen-free conditions as described in detail in ref. [65]. The quantum dots were dispersed into a 5:1 (vol/vol) mixture of mesitylene and 1-dodecene at a concentration of ~0.8 mg ml−1. The solution was refluxed in a sand bath at 215 °C for 4 h, after which it was stirred while irradiated with a 100 W mercury vapour lamp in excess of 12 h to improve photostability of the quantum dots43. The clear solution was filtered through a 0.2 μm PTFE filter and dried. Excess organic polymers formed during hydrosilylation were removed in a centrifugation washing process with acetonitrile as the antisolvent. The Si-QDs underwent an additional ultraviolet light treatment in order to establish higher photo-stability of the covalently bonded surface species.

2.5.3. Device Assembly

As first step, quantum dot powder was dispersed in a small volume of LMA monomer for 3 h to wet the nanoparticle surface and ensure fine dispersion of the individual quantum dots. The monomer–quantum dot mixture was then added to a large volume of LMA together with a secondary monomer, EGDM (LMA:EGDM 80:20% wt/wt for rigid devices and 90:10% wt/wt for flexible ones) that acts as a crosslinking agent, and a radical photoinitiator (IRGACURE 651; 1% wt/wt). After stirring the mixture for 20 min and sonication for 10 min to facilitate quantum dots dispersion, the homogeneous mixture was poured into a mould made of two low-roughness pieces of tempered glass linked by a PVC gasket, and irradiated with 365 nm light from an ultraviolet lamp for 15 min to trigger radical polymerization. The polymerization was then completed by keeping samples in dark for 40 min while leaving them in the mould to avoid the creation of cracks. After completion of the procedure, the slabs were removed from the mould, cut into pieces of desired sizes, and polished. The slabs were cut using an ultra-thin (0.35 mm), high-precision diamond blade and polished with a Logitech LP50 precision lapping and polishing system.

2.5.4. Experimental

All spectroscopic studies were carried out using toluene solutions of quantum dots loaded into quartz cuvettes and Si-QDs/PLMA nanocomposites. In the measurements of photoluminescence dynamics, the samples were vigorously stirred to avoid the effects of photocharging. The absorption spectra of quantum dot solutions and Si-QDs–polymer composites were measured with a Perkin Elmer LAMBDA 950 UV/Vis/NIR spectrophotometer. Photoluminescence spectra and transient photoluminescence measurements were carried out using excitation with <70 ps pulses at 3.1 eV from a pulsed diode laser (Edinburgh Inst. EPL series). The emitted light was collected with a Si charge-coupled device (CCD) camera for the photoluminescence spectra or a

Hamamatsu photomultiplier tube (PMT) coupled to time-correlated single-photon counting (TCSPC) electronics (time resolution ~300 ps) for the time decay dynamics. Photoluminescence quantum efficiency measurements were conducted using a c.w. laser source at 473 nm and the same detection set-up coupled to an integrating sphere. Specifically, the sample was mounted vertically at 45° with respect to the incident beam in antireflection geometry with respect to the output window, with the CCD fibre-coupled to the sphere and shielded by a buffer layer. The same set-up was used for the scattering measurements, in which the LSC edges were either clear or blocked using black paint. For light scattering measurements in the linear propagation configuration, 835 nm light from a laser diode was injected into the LSC edge through a 0.5 mm pin hole and the light scattered from the LSC surfaces was collected using a calibrated photodiode. Optical measurements on the LSCs were carried out by coupling the output edge of the slab to an integrating sphere and using a 473 nm c.w. laser as an excitation source. As for the curved LSCs, the excitation beam was kept perpendicular to the slab surface at any curvature to maintain the penetration depth constant for all measurements. Photoluminescence was detected with the same CCD.

PART II

1. Polymeric solar cells

1.1 Introduction

1.1.1. Solar cells: through generations of photovoltaics

Solar cells can be classified into three categories, depending on their architecture and on the materials used. The first generation includes large-scale, single-junction devices, typically based on crystalline silicon. The 90% of current photovoltaic production is based on this type of solar cells[66, 67]. Such devices performances were improved and could reach 25% of efficiency, but the high cost of material (silicon wafers) and related processing motivated a continuous research to alternatives to this type of devices.

The second generation of solar cells was designed to reduce the high cost of the active materials without losing efficiency. Primarily this aim was pursued by reducing the amount of semiconducting materials, resulting in thin-film based devices. Amorphous silicon, CuInSe, CuGaSe and CdTe are the most successful materials used in this category obtaining PV devices with efficiencies around 20%[68]. Among them, CdTe is one of the most interesting thanks to its low production energy requirements and short energy payback time. [69, 70].

Finally, the third generation of solar cells faces the challenge of lowering the cost through a novel strategy. Besides limiting the amount of active material, the

material itself has to be as cheap as possible, in terms both of cost of raw material and preparation. New concepts and materials led to the development of unconventional devices, such as dye-sensitised solar cells (DSSCs)[71] and organic solar cells. An impressive amount of functional materials for this application was boosted by the infinite possibilities of molecular design ensured by organic chemistry , attracting enormous academic and industrial interest in the last few decades.

Organic photovoltaics offers the possibility of obtaining lightweight, flexible and coloured PV modules. Besides these mechanical advantages compared to the rigid devices of the first two generations, the possibility of fabricate the third generation devices inexpensive through inexpensive all-solution process printing production procedures (roll to roll) makes this technology particularly attractive[72]. Organic photovoltaic has experienced a rapid growing, as it generate big expectations as a low-cost technology[73]. Third generation solar cells also includes multi-junction devices, which are based on the superposition of semiconducting materials each one absorbing, and thus converting, photons with different energy. This strategy can be pursued using both organic materials or inorganic semiconductor. The latter ones allowed to reach the highest efficiency value for solar devices: 46.0% coupled with a concentrator system (at 508 suns with GaInP/GaAs/GaInAsP/GaInAs structure) and 37.9% without concentration (InGaP/GaAs/InGaAs at 1 sun)[74]. However the production cost of these high efficiency devices typically limits them to space and aerospace applications[75].

In recent years another 3rd generation low cost solar cells alternative has emerged: perovskites solar cells. The results related to this kind of device were encouraging in their beginning and in a few years the research on perovskites led to even higher efficiencies compared to OPV, solving many of the drawbacks of its first stage, like device fast degradation[76, 77]. Despite the impressive rapid growth of perovskites-based solar cell efficiency (fig 1.1), polymeric solar cells continue to be particularly attractive thanks to their easy integration on flexible

substrate, as in tissues and coatings. Moreover, their high conversion efficiency at low-intensity light combined with the non-toxicity of their composing materials make them particularly suitable for indoor installation, where the device is illuminated with low light power and is in contact with human life [78-

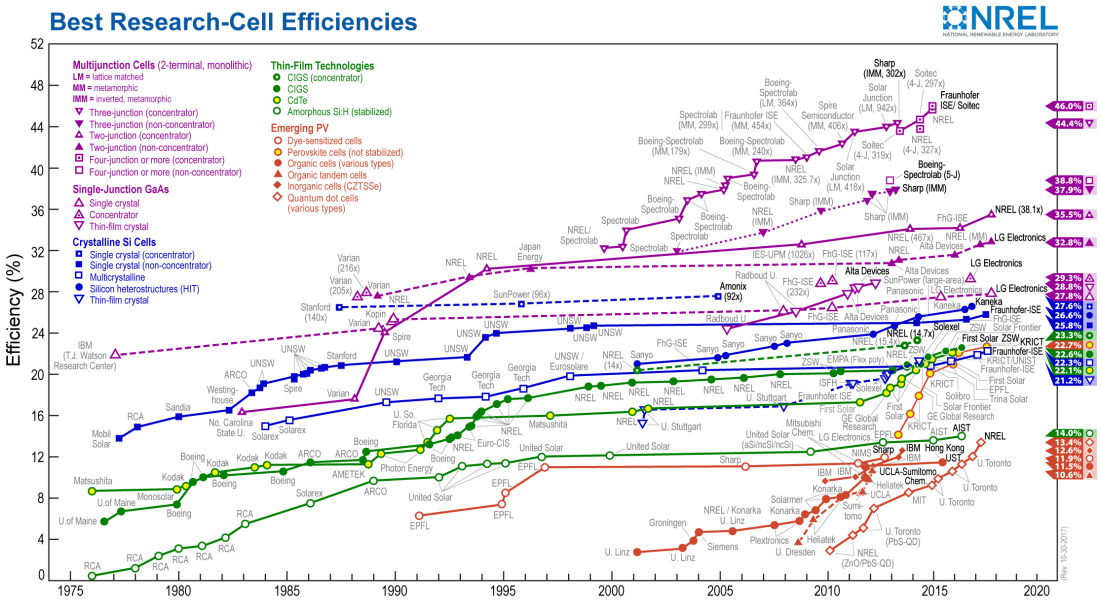

Figure 1 1.: Progress in efficiency for different photovoltaic technologies according to the National Renewable Energy Laboratory. Updated at 30/10/2017
(source https://www.nrel.gov/pv/assets/images/efficiency-chart)

80].

1.1.2. History of PSC

For the first time in 1956, Nelson observed that organic dyes adsorbed on the surface of inorganic semiconductors had an effect on the photo-response of the semiconductor in the dye spectral range[81]: this results was explained arguing that the dissociation of photogenerated hole-electron pair (exciton) was due to the different electronic properties (a p-type semiconductor or “electron donor” and a n-type semiconductors or “electron acceptor”) of the two materials in contact with each other. This concept would become the basic working principle of heterojunction solar cells.

It was successfully applied in a complete device in 1979 by Tang [82], then published on Applied Physics Letters in 1986, who assembled the first bi-layer heterojunction solar cell, consisting of copper phthalocyanine and a perylene derivative, obtaining a device with 1% photovoltaic efficiency[83]. Tang found that the splitting of the photogenerated exciton in elementary charges is facilitated at the hetero-interface between organic materials where the abrupt change of potential energy causes high electric local fields. Thus two materials with different electronic properties, one p-type and one n-type semiconductor, were stacked one on top of the other in a thin layer forming the bi-layer structure[83].

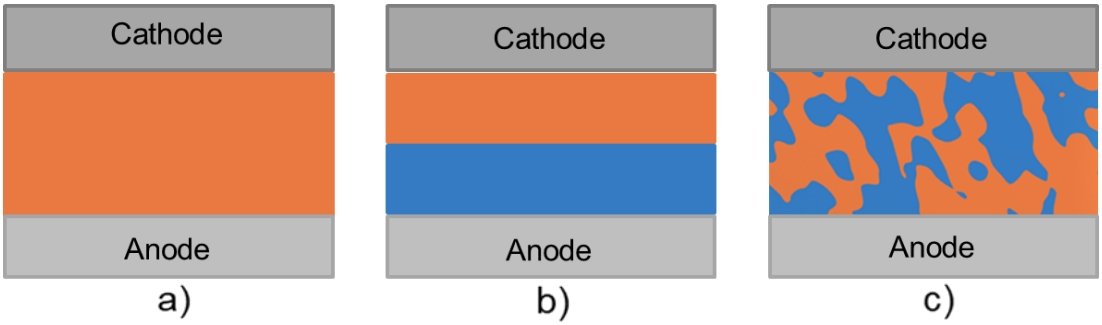

Figure 1.2: Evolution of the structure of polymeric solar cell from single material structure (a) to bilatyer structure (b) to bulk heterojunction (c).

However, the lower dielectric constant of organic materials (in the range of 3-5 [84]) compared to inorganic semiconductors (Si~11.7, CdTe~10.2)[85] results in a stronger electrostatic interaction between electron and hole and thus in a shorter diffusion length, in the order of 10 nm[86]. As a consequence, only the excitons photogenerated in the proximity of the hetero-interface can reach it and be efficiently split into separated charges[87-89],while the excitons generated in the other parts of active layer are lost through recombination[90], without contributing to the total photocurrent. The thinning of bilayer to a thickness of the order of exciton diffusion length, some tens of nm, is not a viable strategy, since so thin active layers exhibit very poor photon harvesting, resulting in low devices efficiency.

The described limiting factors led to the development of a new kind of architecture, the bulk heterojunction (BHJ)[91, 92], illustrated in fig 1.2, in which the p-type and n-type semiconductors are intermixed in a single layer of some hundreds of nm (100-400 nm), where the abundance of interfaces between the two materials facilitate the excitons separation, preserving a good absorbance of incident light.

1.1.3. Structure of a BHJ solar cell

The basic organic solar cell structure consists of two electrodes with different work function, at least one of them being transparent, and an active layer sandwiched between them, where the photon to electron conversion takes place. However, this very simple and basic geometry showed some issues: poor selectivity of the contacts and recombination process in the active layer [93] strongly limited device efficiency. For this reason, in order to increase the compatibility of the active layer with electrodes and to improve the charge extraction property of the device two further layers of functional materials were introduced[94]. These interlayers usually have the function of blocking holes or electrons or enhancing transport of one charge carrier. Moreover, interfacial layers can sometimes provide further advantages, as reduction of surface traps due to better contact between active layer and electrodes or enhancing the harvested light by optimising the optical properties of the multilayer structure[93, 95]. As a result, the typical organic solar cell architecture has become a multilayer stack, where the energy level alignment of the materials used in the structure determines the current flow direction, and thus the type of architecture.

In standard or direct configuration electrons are collected by the top metallic electrode, which acts as the cathode, while holes are collected by the transparent bottom electrode, which acts as anode (fig 1.3a). In inverted configuration, the current flows in the opposite direction, thus the transparent bottom electrode acts as cathode, while the top electrode as anode (fig 1.3b).

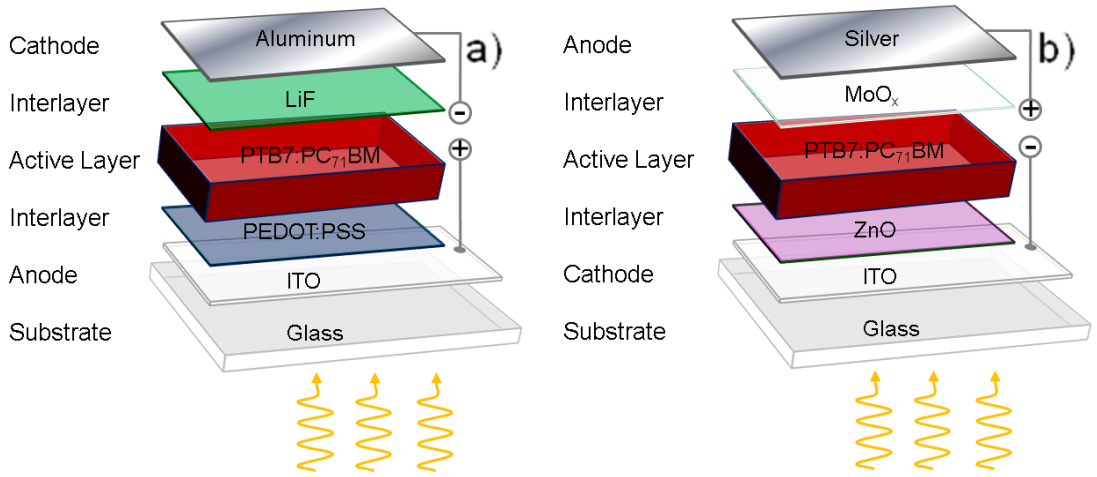

Figure 1.3.: Structures of BHJs solar cells with direct (a) and inverted (b) geometry

The development of the of inverted structure[96] was stimulated by the low stability of direct architecture devices. In particular, the frequently used PEDOT:PSS interlayer typically exhibits high hygroscopic, which leads to the formation of acid species, which degrades both the underlying oxide and the active layer[97]. Moreover, the top electrode may suffer from oxidation processes, which lowers device performance with time. Normal structured devices are, therefore, usually encapsulated to prevent degradation due to moisture or oxygen. Inverted structure avoids the use of PEDOT:PSS replacing it with ZnO, TiO_X or with polyelectrolytes, and of Al, using Ag instead, which exhibits a work function more suitable to work as anode and lower oxidation rates.

1.1.4. Working Mechanism of a BHJ solar cell

The process of conversion of light into electricity by an BHJ organic solar cell can be schematically described by the following steps [98](illustrated in fig 1.4):

a) Absorption of a photon leading to the formation of an exciton;

b) Exciton diffusion to a hetero-interface;

c) Charge transfer from donor to acceptor;

d) Charges separation;

e) Charge transport at electrodes;

f) Charges extraction at respective electrodes.

Absorption mechanism involves the two semiconducting materials blended in the BHJ which typically shows high absorption coefficients (up to 10^5 cm^{-1})[72, 98], thus thicknesses around 100 nm are enough to absorb the majority of the incident photons when a reflective back contact is used. Once a photon is absorbed, an exciton (bounded hole-electron pair) is created in the band of the semiconductor. As explained before, the conversion of exciton into separated charges occurs when the exciton reaches an interface within its diffusion length (10-20 nm). These first two mechanisms, absorption and exciton diffusion, are determined by the nature of the semiconductor material, especially by its electronic configuration and conjugation, while the mechanisms from here on are heavily dependent on the morphology of the blend film.

Once the exciton reaches the interfaces, the abrupt change in electric potential due to the different electrostatic potential of the semiconductor forming the BHJ induces a strong local electric field ($E = -\nabla U$)[72], which separates the exciton in an electron and a hole in the bands of the two materials, called photoinduced charge transfer. In the case of polymer:fullerene based PSC this mechanism happens on a time scale of some tens of fs, much faster than other competing relaxation processes, in the order of ns[99].

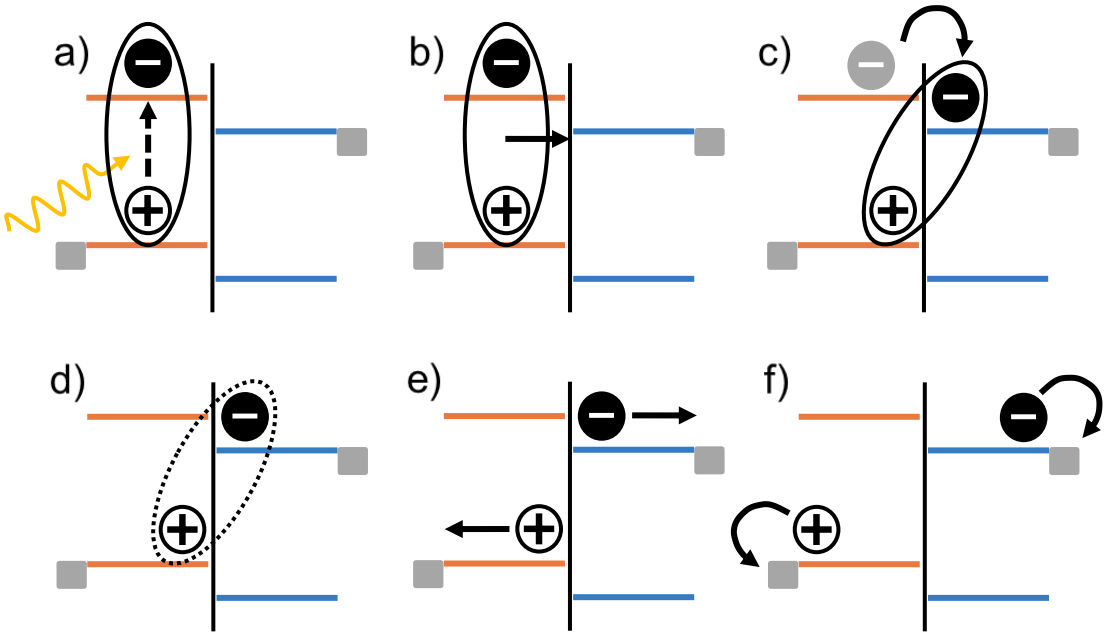

Figure 1 4.: Charge generation and extraction in organic solar cells: a) absorption of light resulting in exciton formation, b) exciton diffusion towards the donor:acceptor interface, c) charge transfer from the donor to the acceptor, d) dissociation of the electron-hole pair into free charges (charge separation), e) charge transport of free carriers towards the electrodes, f) charge collection.

The separated charges in blends can be transported through the BHJ to the proximity of the electrodes. However, electrons (holes) transport can take place only if there is a continuous network of the acceptor (donor) semiconductor from the photoinduced charges transfer point to the corresponding electrode[100]. Additionally to an appropriate pathway, charge carriers need a driving force to reach the electrodes. The difference between the HOMO level of the donor (quasi Fermi level of the holes) and the LUMO level of the acceptor (quasi Fermi level of the electrons) builds up a gradient in the chemical potentials of electrons and holes. This internal electrical field contributes to a field-induced drift of charge carriers., which are correctly transported to their corresponding electrode.

As a last step, charge carriers are extracted from the device through two selective contacts. The selectivity of the contact is determined by the work function of the electrodes, which should match the quasi-Fermi level of electrons (for the cathode) and the quasi-Fermi level of holes (for the anode).

This level alignment favours the charge transfer from the blend to the electrodes, while the morphology of the blend film rules the rest of mechanisms.

As explained above, suitable layer morphology assists an efficient charge transfer and separation at donor-acceptor interface, while free charges will be efficiently transported and collected to appropriate electrodes if adequate percolating pathways are present in the film structure. In contrast, unsuitable morphology results in losses in charge extraction because recombination mechanisms become predominant[101].

1.1.5. Parameters of a BHJ

The efficiency of a BHJ solar cell is calculated from the parameters extracted from its current-voltage (J-V) characteristics. A typical J-V curve of a BHJ under illumination is reported in fig 1.5. Under illumination, the J-V curves crosses each axis in one point, defining the V_{OC}, on the voltage axe, and the J_{SC}, in the current axe. The efficiency of the cell is calculated as the maximum power extracted from the device, which is defined as the maximum power point in the fourth quadrant– the point of the curve where the product of J and V is the maximized[102, 103].

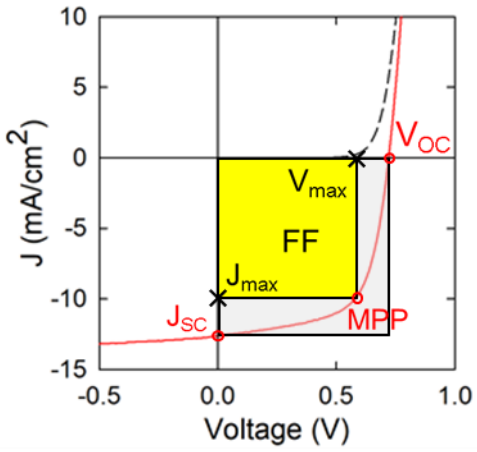

Figure 1 5: Typical JV curve of a polymeric solar cell under light (continuos red line) and under dark (dashed black line). The values for the calculation of the device efficiency are highlighted. Note as the FF can be geometrically expressed as the ratio between the light grey and yellow area. MPP represent the point where the product of J and V is maximized

The photovoltaic power conversion efficiency (PCE) of a solar cell is defined as the property of a PV device of converting solar energy into electric energy and is calculated as the ratio between the output electric power and the input solar power, as reported in the following formula:

$$\eta = \frac{V_{OC} \cdot J_{SC} \cdot FF}{P_{INC}} \qquad FF = \frac{V_{max} \cdot J_{max} \cdot}{V_{OC} J_{SC}}$$

where V_{OC} is the open circuit voltage, J_{SC} is the short circuit current, FF is the fill factor, and P_{INC} is the incident light power density.

This light intensity is standardized at 100 mW/cm^2 with a spectral intensity distribution matching that of the sun on the earth's surface at an incident angle of 48.2°, which is called the AM 1.5 spectrum[104]. In the dark, there is almost no current flowing, until the applied voltage exceeds the V_{OC} and thus the contacts start to inject charges inside the device, as visible from the diode-like trend of the J-V curve.

The electric functioning of every solar cell can be expressed through the use of an equivalent circuit: such circuit is useful to represent the many-variable-dependent property of the device in terms of simple parameters.

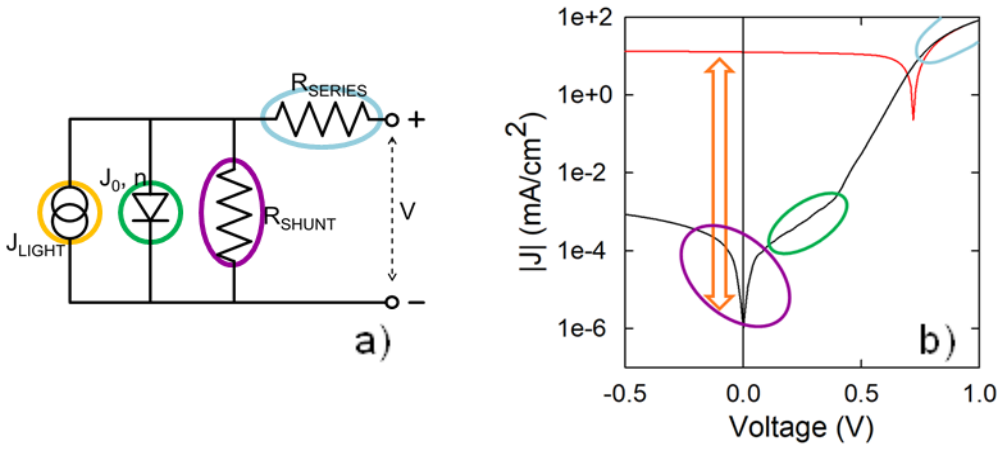

Figure 1 6.: a) equivalen circuit of a typical polymeric solar cell; b) Typical JV curve of a polymeric solar cell under light (continuos red line) and under dark (black line) in logaritmic scale: the region of influence of the electrical equivalent element of a) are marked with the same color.

The simplest equivalent circuit proposed for solar cells is depicted in fig 1.6a and it consists of: a source that provides (photo)current J_{LIGHT}, under illumination; a diode that gives saturation current J_0 (dark current at reverse bias), with an ideality factor n; parallel (or shunt) resistance R_{SH}, which considers current leakage through the device; a series resistance R_S, that takes into account the resistivity of the semiconductors and electrodes as well as the resistance at interfaces[105].

Open Circuit Voltage

The value of the open circuit voltage is strictly connected to the alignment of energy level of the compounds of the BHJ. In case the quasi Fermi level of electrons (holes) lies above (below) the cathode (anode) work function level, the device structure can be simplified with a metal-insulator-metal (MIM) structure and the V_{OC} can be easily calculated as the difference in work functions of the two metal contacts[100]. In case the level alignment of electrodes and active layer compounds is opposite, the maximum available voltage is dependent on the difference between the quasi Fermi levels of holes (HOMO level of donor) and of electrons (LUMO level of acceptor)[106, 107].

For polymer:PCBM based cells, an empiric formula for the calculation of the V_{OC}, given the energy levels of donor and acceptor, was derived by Brabec[106] by varying the donor polymers with different energy levels blended with PCBM:

$$V_{OC} = \frac{1}{e}(E_{DONOR}^{HOMO} - E_{PCBM}^{LUMO}) - 0.3$$

Where e is the elemental charge and 0.3 is an empirical constant which takes into account the energy of the bounded exciton[108-110]. However, the descripted general rule for the determination of V_{OC} is heavily dependent on the effect of the recombination processes inside the device, which in its turn varies with the morphology of the blend.

Short Circuit Current

The J_{SC} relies on all processes occurring from the absorption of a photon to the collection of process. In the ideal of loss free contacts, the short circuit current, J_{SC}, is determined as:

$$J_{SC} = \frac{n \cdot e \cdot \mu \cdot E}{S}$$

where n is the density of charge carriers, e is the elementary charge, μ is the mobility, E is the electric field and S is the area of the device. However, as in the case of V_{OC}, typically the measured J_{SC} value differs from its calculated value because of recombination processes. If n, which takes into account the efficiency of the photo-induced charge generation in the bulk, is determined by the nature of the semiconductors materials, the mobility μ can't be considered a material parameter but rather a device parameter which depends on the nanoscale morphology of the organic semiconductor thin film[111, 112]. As a matter of fact, the four subsequent processes which complete the conversion of a photon into a collected charge at electrode, thus concurring to the J_{SC} (charge transfer from donor to acceptor, charges separation, charge transport at electrodes charges extraction at respective electrodes) are all morphology-dependent.

Fill Factor

The fill factor is probably the most difficult factor to parametrize since its trend is determined by the simultaneous effect of morphology, energy levels and charge carrier dynamics. Fill factor is an indication of how much a cell is close to an ideal photodiode, thus represents how much a device is capable to transport charge carriers to the electrodes, when the built-in field is lowered toward the open circuit voltage[113]. There are two competing processes concurring to charge carriers dynamics, that are recombination and transport,

and the FF is an indication of which one is dominant[114]. Hence, the product of the lifetime τ and of the mobility μ determines the distance d that charge carriers can drift under a certain electric field E as:

$$d = E \cdot \mu \cdot \tau$$

The product $\mu \cdot \tau$ has to be maximized in order to favour transport rather than recombination. This product is strictly dependent on the morphology of the blend, since, as mentioned above, μ is the mobility of the materials in the device, while τ is influenced by all charge recombination mechanisms, which are determined by the nanoscale morphology of the film. Furthermore, energy levels alignment can influence the FF value since it determines the ohmicity of the contacts, thus the series resistance of the device, which should be minimized. Finally, finite conductivity of the ITO substrate clearly limits the FF on large area solar cells.[115]

1.1.6. Role of the processing

As described above, the final efficiency of BHJ devices relies on the optimization of V_{OC}, J_{SC} and FF parameters, all of them heavily dependent on the morphology of the blend. Thus the transition from materials with good design for potential BHJ application to a device with good performance goes through the optimization of the morphology of such material in the blend. which is hard to predict but can be controlled through the correct choice of the processing. The choice of the processing is influenced by the macromolecular properties of the material, thus, batch to batch variation of the same material could result not only in intrinsically different optical and electro-optical features, but also in a different active layer morphology once blended[116].

The optimization of the morphology is performed by the combination of a plenty of parameters. In the case of the active layer, some of them are chosen to optimize its deposition: the choice of solvent, temperature of the substrate and

casting solution, use of additives, concentration. Others can be used to improve the initial morphology: the use of thermal treatment, solvent annealing and surface treatments[117].

1.1.7. Materials for PSC

Acceptors

The great advances in BHJ solar cells since the beginning of this technology have been largely driven by the development of conjugated polymers, used as electron-donating materials. On one hand, fullerene derivatives have been used as acceptors in blends since the very beginning of OPV[118]. Among them, the most widely used are [6,6]-phenyl-C61-butyric acid methyl ester ($PC_{60}BM$), [6,6]-phenyl-C71-butyric acid methyl ester ($PC_{71}BM$) and Tetrahydro-di[1,4]methano naphthalene [1,2:2′,3′,56,60:2′′,3′′] [5,6]fullerene-C60. They show high solubility in organic solvent, which enables them to be compatible with the large majority of polymeric donors[119].

However, these two acceptors suffer from some intrinsic shortcomings such as limited absorption, difficult functionalization, and high production cost. Therefore, recently novel non-fullerene acceptors based on functionalized polymers that can overcome the above-mentioned disadvantages were developed. As a matter of fact, research on non-fullerene acceptors has made considerable progress in the last few years and a highest PCE of around 12% has been achieved [120].

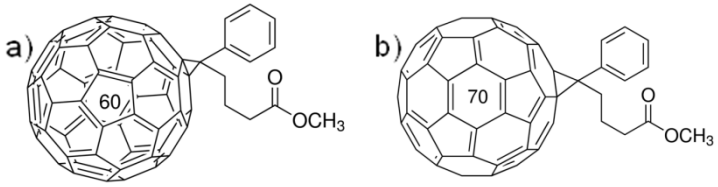

Figure 1 5.: Chemical structures of $PC_{60}BM$ (a) and $PC_{71}BM$ (b).

On the other hand, the infinite possibilities offered by organic chemistry allowed to develop an impressive number of functionalized conjugated polymers, used as electron donating materials. The first family of conjugated polymers that were used successfully as donor materials were based on poly(phenylenevinylene)s (PPV), reaching efficiencies up to 3.3%[121].

Later, regioregular poly(3hexylthiophene-2,5-diyl) (P3HT) emerged as a more efficient material, showing superior charge mobility and efficiencies reaching 5%[122].

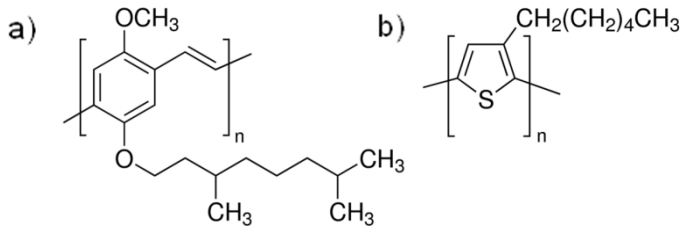

Figure 1.6.: Structure of a) MDMO-PPV and b) P3HT

The main limitation of these classes of polymers is the poor matching of their photon absorbance with the photon flux solar spectrum[123]. Further development was afterwards focused on lowering the band gap of the polymer, in particular following the strategy of using structures bearing an electron acceptor unit alternated to an electron donor unit (A-D copolymers). The incorporation of alternating donor-acceptor units in the polymer backbone as well as conjugated bridging units has been used to modulate the properties of the polymers, including, of course, their energy band gap. This approach leads to the production of several polymers with efficiency exceeding 9%.

However, in order to make an OPV polymeric material suitable for large-scale production, four requirements have to be fulfilled: high efficiency, low production cost, sufficient stability of the resulting device, the compatibility with roll to roll fabrication[124].

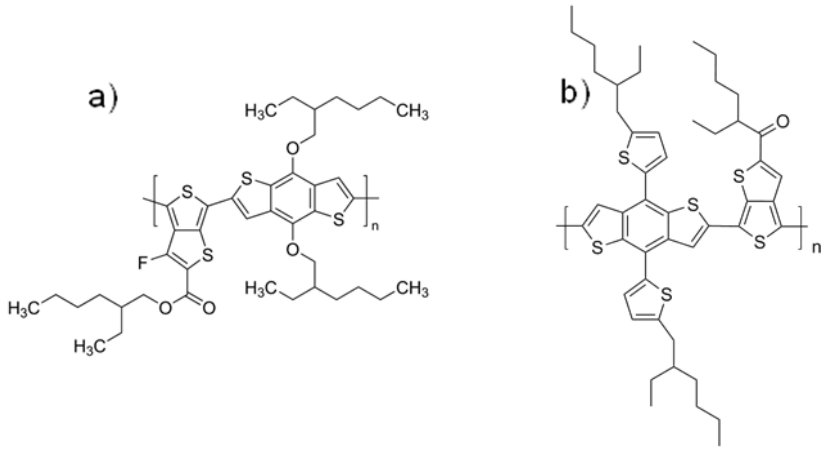

Figure 1 7: Chemical structure of a) PTB7 and b)PTB7-Th

In the last decade a great research effort was put into increasing the efficiency of the PV polymers, reaching the remarkable result of efficiency exceeding 10% using D–A copolymers, while much less research effort was spent in limiting the active material production cost in the perspective of a large scale production. This aspect includes both the synthesis of the monomers and the polymerization process, thus it relies on the availability of raw materials, the number and the complexity of the synthetic steps and on the scalability of the purification processes. An acceptable cost of polymers, which could lead to commercially viable modules is around 10 €/g[124]. Considering these aspects, poly(3-hexyl)thiophene (P3HT), in spite of its lower performances compared to those of other D–A copolymers, still remains the material which better fulfils the scalability requirements.

Other functional materials for PSC - Interlayers

Beside the great effort in designing novel high-performing materials for the active layer, the development of devices exceeding 10% efficiency was possible also thanks to the careful optimization of device interfaces [96, 125]. As a matter of fact, the control of charge transport through interfaces is fundamental, and interfacial engineering is a useful approach to obtain high efficiency device. For this purpose, PSCs structure complexity is increased by inserting functional

materials between the active layer and the electrodes. An electron extracting layer near the cathode and a hole extracting layer near the anode are integrated in the multilayer structure[126]. These interlayers can improve the device PCE by different mechanisms, depending on the class of material adopted. A better ohmicity of the contacts between electrodes and active layer can be obtained through the use of interlayers which reduces the barrier height between the quasi Fermi level of charge carriers and electrodes work functions. This better energy levels alignment not only improves the charge extraction efficiency, but also maximizes the V_{OC}. The most common materials for such levels alignment are low work function metals, as Ca, Ba or Mg .

Another effect induced by interlayers is the modification of the electrode work function which directly influences the built-in potential. An increase of built in potential increases the internal electric field and thus the charge separation efficiency. Such modification usually also leads to a reduction of charge carriers recombinations. The modification of electrodes work function is usually performed by inserting materials containing dipoles (PFO derivatives, zwitterionic molecules or polymers, modified acceptors) [127-132] or with preferential alignments (self-assembled monolayer)[133].

Finally interfacial layers can prevent from the detrimental effect of electrode metal ions diffusing into the organic layer, which typically results in a shunting of the device. The use of interlayers avoids the direct contact between the active layer and the electrodes where a high density of traps can lead to charges recombination. Robust inorganic metal oxides (ZnO, TiO_2, MoO_X) [105, 128] are typically used for this purpose. However, low work function metals, alkali compounds and a part of metal oxide requires deposition by evaporation, a strong limitation with the roll to roll fabrication of the device. A higher interest from a scaling-up prospective are gaining solution-processed interlayers, which can be deposited from orthogonal solvent respect to the casting solvents of the active layer.

2. PBDTTPD-based polymeric solar cells

2.1. Abstract

In this section of my thesis I performed a comparative study about the photovoltaic performances in bulk hetero junction (BHJ) solar cells of poly[(benzo[1,2-b:4,5-b']dithiophene)-alt-(4H-thieno[3,4-c]pyrrole-4,6(5H)-dione)]) (PBDTTPB) blended with $PC_{71}BM$ as acceptor. PBDTTPD shows an acceptable trade-off between device performances and structural complexity, which makes it a promising candidate for a future industrial scale production, particularly in terms of production costs of scalable process. However, the preparation of this polymer is typically performed via Stille reaction, a synthesis which involves the use of high toxicity organo-tin compounds, requires the pre-functionalization of the monomers and produces stoichiometric amounts of heavy-metal containing waste, three critical aspects that still have to be addressed to make this technology suitable for massive production. Recently, Direct (Hetero)Arylation Polymerization (DHAP) has emerged as an alternative synthetic route to conventional cross-coupling reaction, such as Stille, without the requirements of-pre-functionalizing of the reagent monomers and avoids the use/production of heavy-metal-containing reagents/waste.

The PV performances of BHJ based on PBDTTPB obtained via DHAP and Stille synthesis (one produced in laboratories and one commercially available) were compared. This study highlighted that the polymer synthetized via DHAP blended with $PC_{71}BM$ exhibits a power conversion efficiency comparable with that of the commercially available PBDTTPD. Through the use of optical and morphological characterizations and charge recombination analysis, I studied the relationship between the molecular characteristics of these polymers and their functionality as active components in BHJ solar cells

2.2. Materials

PBDTTPD

Among the polymers with D-A structure, one with an interesting efficiency/complexity trade-off is the poly[(benzo[1,2-b:4,5-b']dithiophene)-alt-(4H-thieno[3,4-c]pyrrole-4,6(5H)-dione)]) (PBDTTPB)[124, 134]. In terms of monomers preparation cost, the first of its composing monomer, thienopyrroledione (TPD), is already being prepared with an optimized synthesis, which likely makes this monomer the most suitable unit for highly efficient and scalable OPV[124], while the second, benzodithiophene (BDT), shows preparation cost in the average of donor monomers.

In addition to the scalability of monomers preparation, also the polymerization to obtain the final D-A polymer has to be taken into consideration[124, 135]. As a matter of fact, these monomers are typically polymerized via Stille coupling, a synthetic route which involves highly toxic

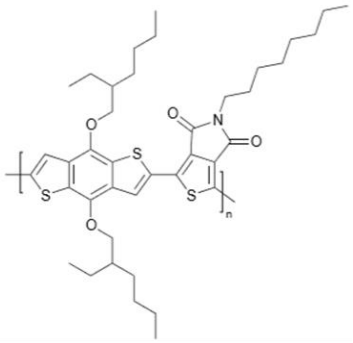

Figure 2.1.: PBDTTPD structure

arylstannanes as monomers and produces stoichiometric amounts of trialkyl-tin bromide.

However, Direct (Hetero)Arylation Polymerization (DHAP) has recently emerged as an alternative synthetic method to conventional cross-coupling reactions for the synthesis of organic electronic materials[136-138]. DHAP avoids the pre-functionalization of both monomers involved in the polymerization and does not generate waste containing highly toxic heavy materials as tin[139, 140].

This novel synthetic approach fulfills the requirements necessary for large-scale production polymer for OPV. Moreover, the synthesis involves a cheaper $Pd(PPh_3)_4$ catalyst, used for the first time to obtain OPV grade PBDTTPD. The choice of using a less common Pd(0) catalyst such as $Pd(PPh_3)_4$ instead of classic quite expensive palladium(II) catalysts, may represent a significant improvement in this synthetic approach, especially with the aim of further decreasing the production costs.

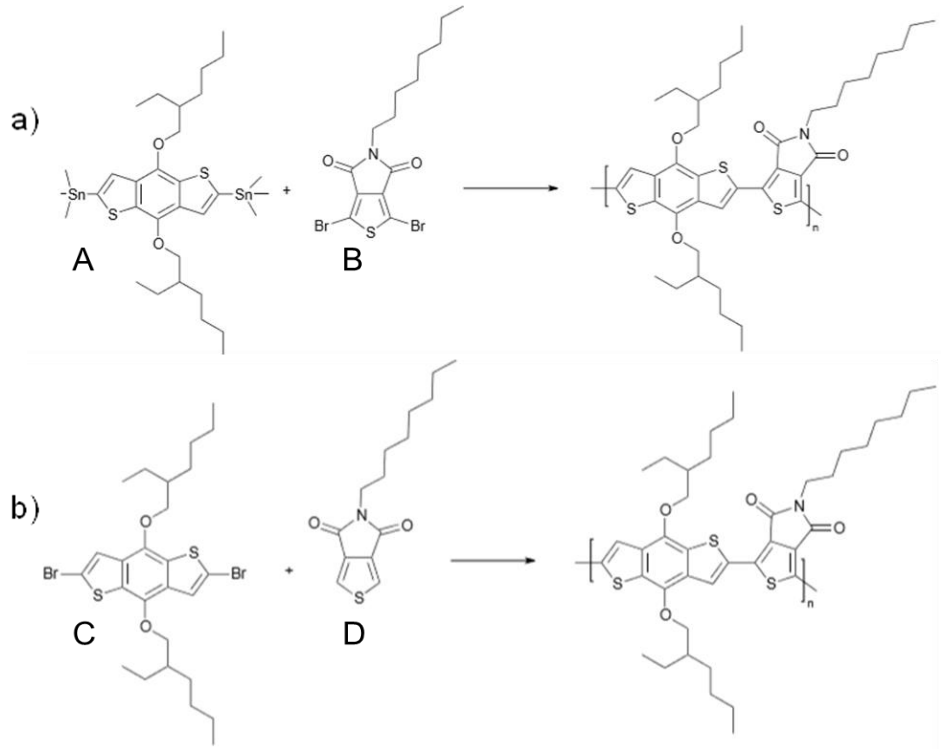

Figure 2.2.: Illustration of the two synthetic routes for PBDTTPD preparation: Stille coupling, is performed usind bis-trimethyl-stannyl- BDT and dibromo-TPD (a); DHAP requires dibromo-BDT and TDP (b)

The synthesis and macromolecular characterization of the polymers used in this study were carried out respectively at the chemistry department of the University of Bari and at ENI s.p.a. Istituto Donegani in Novara. PStille was prepared via the above described Stille coupling reaction, while pDHAP was prepared with the novel approach for PBDTTPD of hetero arylation using $Pd(PPh_3)_4$ as catalyst. The third polymer included in the comparison is a commercially available PBDTTPD obtained through Stille coupling and purchased from 1-Materials (pComm).

2.3 Results

2.3.1. Optical properties

The polymers used in this comparative study were at first characterized in terms of molecular mass distributions. The polymers obtained via Stille synthesis exhibit a weight average molecular weight (M_W) respectively of 34 KDa for the reference polymer and of 45 KDa for the commercial available polymer. Considering also the number average molecular weight (M_N) reported in tab 2.1, it can be noticed that the two polymers prepared via Stille have a similar weight distribution, with a slightly higher average polymer chain length for the pComm. On the other hand, the polymer obtained via DHAP shows a much higher M_W (72 KDa), indicating the presence of longer polymerized chains, but its limited M_N denotes a very broad molecular weight distribution compared with the PBDTTPD obtained via Stille. The poorer control on molecular weight distribution is a typical feature of direct-Arylation polymerizations.

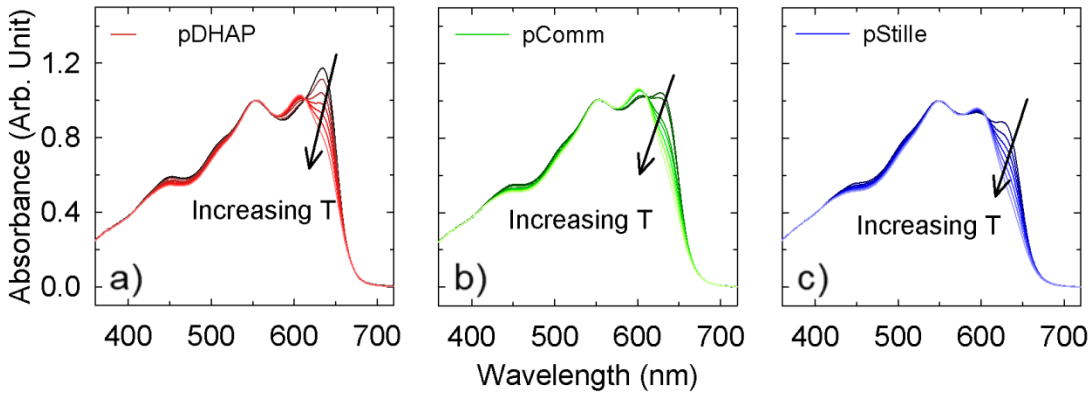

Figure 2.3.:Absorbance spectra of pDHAP (a), pComm (b) and pStille (c) in chlorobenzene solution (0.2 mg/ml) as a function of the temperature. Solutions temperature was varied from 25°C (dark curves) to 85 °C (light curves)

Polymer	M_N (KDa)	M_W (KDa)	PDI
pStille	10	34	3.4
pComm	15	45	3
pDHAP	12	72	6

Table 2.1.: Number average molar mass, mass average molar mass and polydispersity index of the polymers included in the comparison.

Such differences may strongly influence the behaviour of the polymers in terms of aggregation and solubility, so in order to get some insight on those properties, I recorded the temperature-dependent UV-VIS absorption spectra of PDHAP pStille and pComm dissolved in chlorobenzene (fig 2.3). The spectra show common features, as the absorption peak between 626 and 634 nm, which progressively decreases with increasing temperature in all three samples. Such feature can be ascribed to the aggregation phenomena, also in highly diluted solutions, which is inhibited upon heating the solution. Interestingly, at room temperature the polymer behaviour is quite different as evident from the relative intensity of the aggregation peak, which is higher going from the pStille to pComm to pDHAP. The increasing trend towards aggregation can be essentially explained by the M_W values of the polymers, 34 KDa, 45 KDa and 75 KDa for pStille, pComm e pDHAP respectively. Moreover, since the highest M_W polymer also has the highest polydispersity index, the pronounced aggregation peak of the pDHAP could be explained also considering an important contribution from the higher molecular weight chains of its distribution in the solution behaviour.

2.3.2. Device Optimization

At first, the optimization of the device was performed through the one-by-one variation of the processing parameters (additives, acceptor:donor ratio, active layer thickness), starting from a literature recipe described by LeClerc (ref. [141]), used as reference. This section of the study was performed only for the pDHAP polymer and subsequently it was verified if the established optimized conditions for the device preparation were also valid for other two polymers included in the comparison. All devices were assembled with the same architecture ITO/PEDOT:PSS/Active Layer/Calcium /Aluminium.

Starting recipe

The starting recipe for the assembly of the devices was based on the recipe descripted by LeClerc in 2010,(ref [141]) when PBDTTPD was used for the first time as donor in direct architecture BHJ. In this recipe the polymer was blended with $PC_{71}BM$, in order to ensure a higher absorption in the 440-530 nm region, and dissolved in 1,2-Dichlorobenzene (ODCB). However ODCB requires high temperatures of deposition (180°C) and long drying time (24-36 hours) due to its high vapor pressure and boiling point. These two assembly steps requirements are difficultly compatible with a large scale devices production. Moreover, the high temperature excludes the use of ITO-covered flexible plastic substrates instead of ITO-covered glass, since polymeric substrates typically cannot be processed at a temperature higher than 150°C. For these reasons, 1-Chlorobenzene (CB) was preferred as casting solvent, since it typically shows a better filmability also at lower casting temperature (<100°C) and requires shorter drying processes (<1 hour).

Moreover, calcium was chosen as electron buffer layer instead of LiF reported in the reference. This variation was done considering that the strong tendency of the polymer to aggregate could lead to a high surface roughness of the active layer, a feature which makes it difficult to perform an uniform coverage by a thin LiF layer(2 nm).

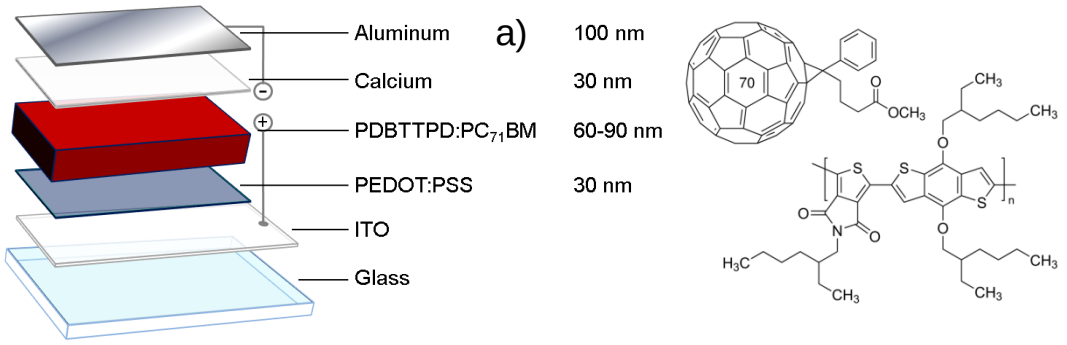

Figure 2.4.:a) Device structure and corresponding average thickness of layers composing the multilayer; b) structure of donor and acceptor

On the other hand, a thick layer of Calcium (30 nm) deposited on top of active layer before Aluminium ensured a uniform coverage of the active layer and thus an efficient electrons extraction capability. The structure of the devices is reported in fig 2.4.

Additive concentration

As a general trend I found out that the pure CB devices exhibit low performances, achieving a power conversion efficiencies of 3.08% for the pDHAP based solar cells. These efficiencies are considerably lower than the reference 5.5% efficiency that was reported in the literature for PBDTTPD with comparable molar mass to the polymers here under study. The observed gap in efficiency is mainly due to the difference in the J_{SC} parameter, which in the literature reference recipe is 50% higher than in the pDHAP-based device.

It is worth noting that such poor J_{SC} characteristics could arise from the non-optimal blend morphology of the active layers prepared from CB. The addition of a small amount of 1-Chloronaphthalene (CN) is known to be an effective tool to improve the performances of PBDTTPD:$PC_{71}BM$ solar cells through the optimization of the blend morphology[142-144].

The PV characteristics of devices prepared with different concentration of

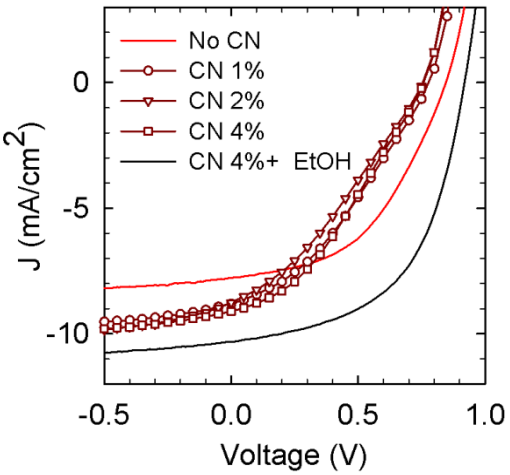

Figure 2.5.: JV characteristics of pDHAP:$PC_{71}BM$ based device without additive (red curve) and with different concentration of CN additive (line with markers). Black lines referes to a device which was treated with Ethanol.

CN highlighted that an addition of 4% V/V to the blend solvent induces an improvement of the J_{SC}, filling up its gap with the device reported in ref [141] which was processed from ODCB. However, upon addition of CN to the blend solvent, the JV of the device shows a prominent drop in the FF. As shown in fig 2.5 the JV curve of the pDHAP device casted from CB+CN, showed a kink near the V_{OC} which is believed to be related to poor charge extraction[113]. A post-deposition surface treatment of the active layers with ethanol (EtOH), whose effect will be discussed later, was performed as a further processing step, since it was reported as a valuable method to engineer the active layer/electrode interfaces in BHJ solar cells[145, 146] . Actually, upon EtOH treatment, the kink in the JV curve of the pDHAP cell disappeared.

Donor:acceptor Ratio

The best donor:acceptor ratio was determined by measuring the efficiency of the devices through their current-voltage characteristic (JV) and External Quantum Efficiency (EQE) spectra. The total concentration of the donor:acceptor solution was modified in order to get a similar viscosity with different donor:acceptor ratio, in particular maintaining constant the $PC_{71}BM$ concentration in the solution, since $PC_{71}BM$ is the component that mostly influences this feature of the solution. The thickness of the devices is maintained constant at ~80 nm. The JV curves are reported in fig 2.6a and show that 1:1.5 polymer:$PC_{71}BM$ was the best performing ratio, particularly for the better photon-to-electron conversion of the blend, as it could be deduced from the higher value of the J_{SC}. On the other hand, the FF and V_{OC} do not show any significant variations with different donor:acceptor ratios. Such results are in agreement with the experimental observations from the EQE profile and the absorbance spectra of the three device, respectively reported in fig 2.6b and c.
The device with 1:2 blend ratio shows a higher intensity of absorbance in the $PC_{71}BM$ band range (400-550 nm) which, however, is not matched with a higher EQE profile in the same wavelength range.

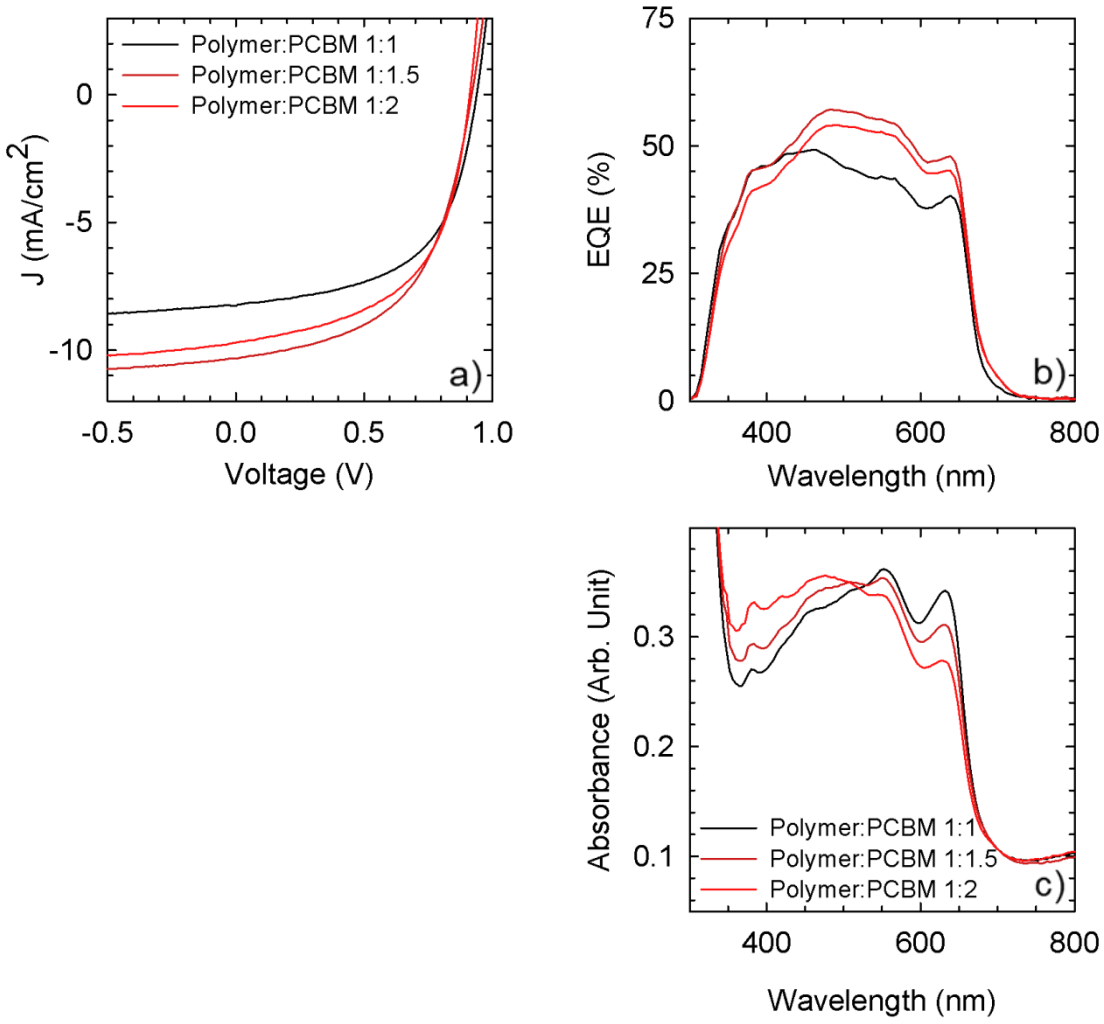

Figure 2.6.: a) JV characteristics b) EQE spectra and c) absorbance spectra of devices with pDHAP:$PC_{71}BM$ as active layer with different polymer:PCBM ratio.

Such result indicates that the lower photocurrent is not due to a lower photon harvesting, but rather to a limited conversion which could be ascribed to a non-optimized blend morphology. The 1:1 blend ratio device has a EQE comparable to the best performing device in the low wavelength region, but it displays a notable drop in the other visible spectra range, which leads to a 20% J_{SC} loss (7.97 against 10.10 mA/cm^2) if compared with the 1:1,5 blend ratio. Even though a larger fraction of light is absorbed by the PBDTTPD, the poorer transport properties of the film due to a non-optimized morphology and to lower charges mobility results in a lower photon to electron conversion efficiency, thus in a lower J_{SC}. Therefore a better blend morphology could explain the better performance of the device with 1:1.5 blend ratio

Polymer: PCBM ratio	V_{OC} (V)	FF	J_{SC} (mA/cm²)	η [%]	η* [%]
1:1	0.93	0.56	7.97	4.16	4.41
1:1.5	0.92	0.54	10.1	5.14	5.31
1:2	0.91	0.55	9.70	4.91	5.11

Table 2.2.: PV parameters of pDHAP:$PC_{71}BM$ based devices with different polymer:PCBM ratio. Average value out of 6 devices; (*) referes to the best value.

Active layer thickness

Secondly, the active layer thickness was optimized taking into consideration both the peak efficiency and the reproducibility of the results. In order to avoid experimental batch to batch errors in the weighing of components and in the volume of chlorobenzene, the thickness was varied by casting all the devices from the same 1:1.5 polymer:$PC_{71}BM$ mother solution and changing the speed of casting procedure.

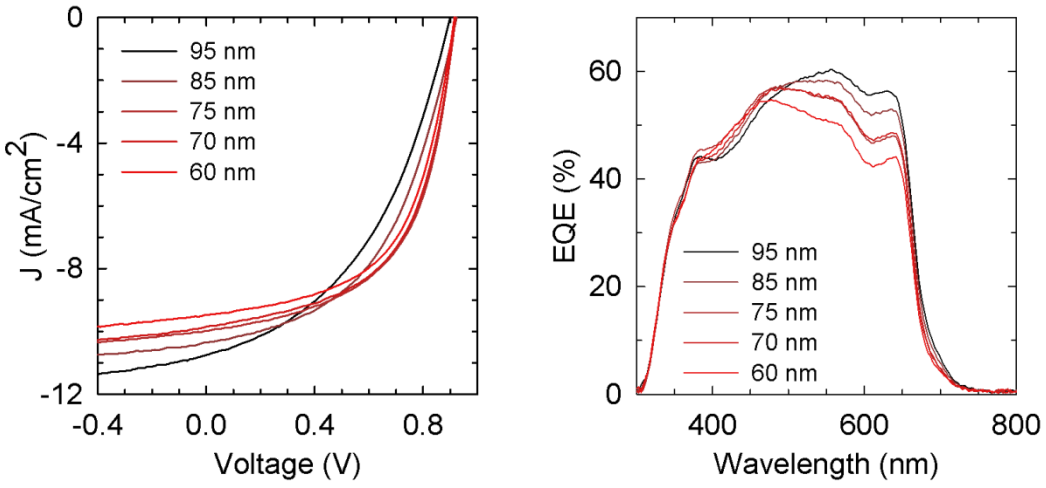

Figure 2.7.:a) JV spectra and b) EQE spectra of of devices with pDHAP:$PC_{71}BM$ as active layer with different active layer thicknesses.

Thickness (nm)	Deposition speed (rpm)	V_{OC} (V)	FF	J_{SC} [mA/cm²]	η(%)	η (%)*
95	1200	0.9	0.43	10.81	4.24	4.80
85	1500	0.92	0.49	10.44	4.74	4.85
75	1800	0.92	0.54	10.31	5.14	5.31
70	2100	0.92	0.56	9.85	5.14	5.27
60	2400	0.92	0.57	9.48	4.96	5.07

Table 2.3.: PV parameters of pDHAP:$PC_{71}BM$ based devices with different active layer thickness.. Average value out of 6 devices; (*) refers to the best value.

The JV curves and the EQE spectra of devices with different active layer thickness are shown in fig 2.7. The best trade-off between efficiency and reproducibility was obtained with an active layer thickness of 75 nm. Interestingly the trend of the PV parameter, reported in tab 2.3, shows that FF increases with decreasing thickness, while the J_{SC} increases with increasing thickness of active layer. Such feature can be explained considering that the rise of J_{SC} is generated by a better photon harvesting capability due to a higher absorbance of the active layer. On the other hand, the FF of the devices decreases with increasing thickness due to a more difficult charge transport, since photo-generated charges have to travel for longer distances in the device before reaching the electrodes. No modification of blend morphology induced by a different blend thickness is expected, therefore a longer charge carrier path inside the blend results in a higher probability of recombination and in a lower charge collecting at electrodes compared to thinner device, which explains the FF reduction.[147]

2.3.3. Comparison of devices performance

In this chapter I will discuss modification of PV parameters of pStille, pComm and pDHAP based device through processing. The study of the performance of the different polymers through processing gave the opportunity to highlight some peculiar aspects of pDHAP and to show the relationship between the polymer morphologies in the blend and the PV characteristics of related devices. Such analysis was performed by measuring the features of the devices through a combination of opto-electrical, optical and morphological characterization.

Devices performance through processing

Cells were first investigated using pure CB as the processing solvent. As general trend I found that the CB devices exhibit the lowest performances, achieving efficiencies around 3% for the three polymers in the comparison.

However, it is worth nothing that at this processing stage, the devices made with pDHAP exhibit a higher J_{SC} compared to polymers obtained via Stille (7.80 mA/cm² versus 6.88 mA/cm² and 5.46 mA/cm² for pComm and pStille respectively) observed from the JV measurement (fig 2.8a) and confirmed by the EQE spectra (fig 2.8d).

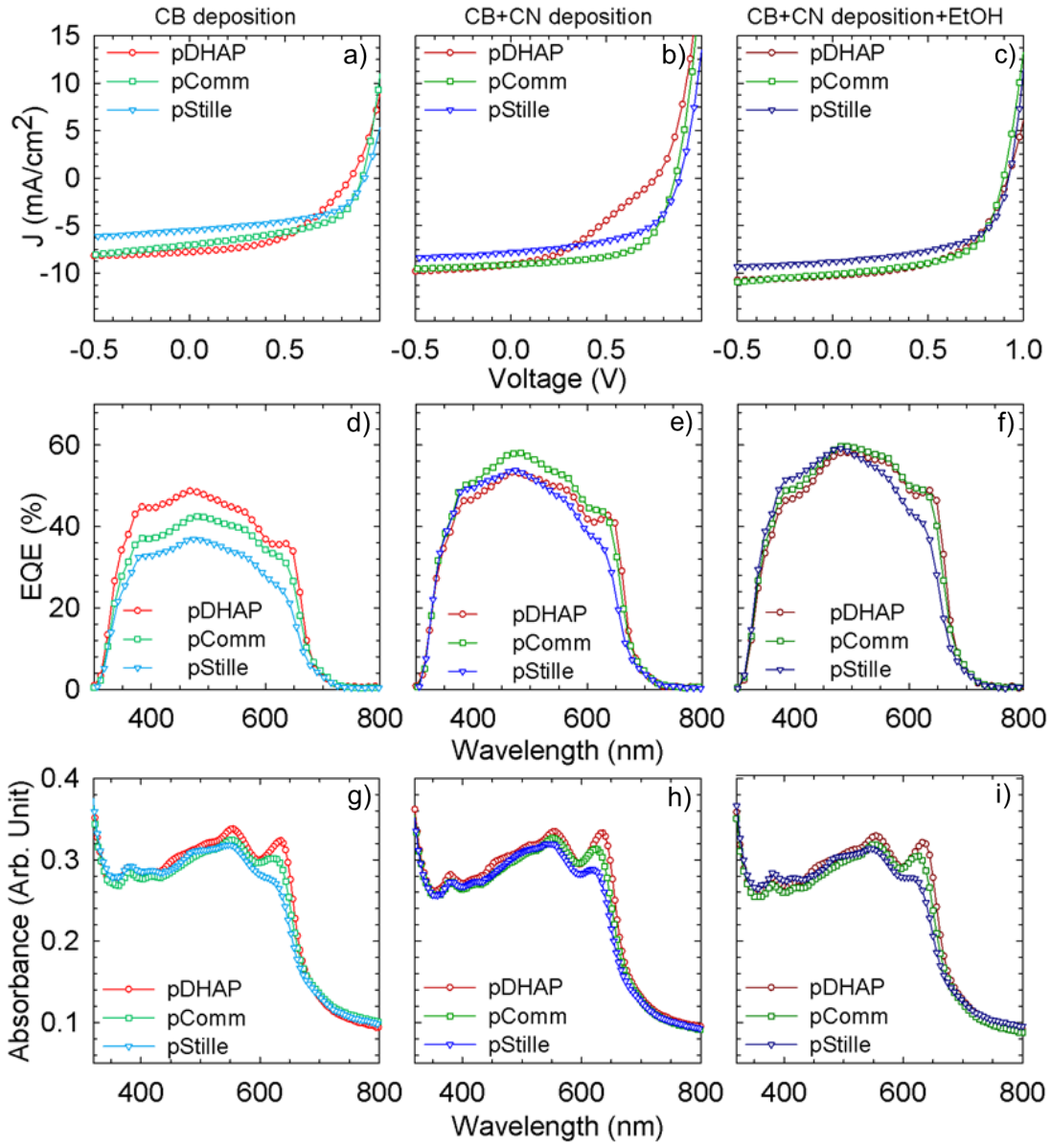

Figure 2.8: JV characteristics (a,b,c), EQE spectra (d,e,f) and absorbance spectra (g,h,i) of PBDTTPD:$PC_{71}BM$- based devices. Red lines refer to pDHAP, green lines to pComm and blue lines to pStille.

A higher J_{SC} value might be due to a higher absorbance of the active layer. However from the absorbance spectra of the active layer blends casted from CB (fig. 2.8g), no differences in the maximum OD max values are observed in the blends total absorption. On the other hand, they show different relative intensity of the absorbance band at 630 nm which is more pronounced for pDHAP and decreases going to pComm and pStille.

Such feature is the fingerprint of polymer aggregation (see fig 2.3), therefore, aggregate formation in the films is in agreement with the degree of aggregation of the polymer chains in solution. This indicates that the aggregates in solution can act as crystallization/aggregation seeds during the film formation process[144].

As already introduced in the device optimization section, the addition of a small amount of CN (optimized at 4%) was used to improve the blend morphology. In the three devices, I observed that CN processing induces a general enhancement of the J_{SC}.

Such enhancement is particularly relevant in pStille and pComm, which show a rise of around 30% (from 6.88 mA/cm^2 to 9.12 mA/cm^2 and from 5.46 mA/cm^2 to 7.82 mA/cm^2 for pComm and pStille respectively) compared to a moderate rise from pDHAP base device (from 7.80 mA/cm^2 to 8.84 mA/cm^2). This enhancement observed in the JV measurement (reported in fig 2.8b) is also confirmed by the EQE spectra (fig 2.8e). From the absorbance spectral patterns reported in fig 2.8d and e it is evident that the peaks of aggregates at 630 nm show a pronounced enhancement in blends containing pComm and pStille, while no significant modification is observed in pDHAP device. Therefore, similarly to the device casted from CB, these results highlight that there is a relationship between the degree of aggregation of the polymer in the film and the photocurrent in the device.

Finally, a post deposition ethanol treatment was performed on the devices, whose JV characteristic, EQE spectra and absorbance spectra are reported in the third column of fig.2.8. With this processing, 10% increment of the J_{SC} was

observed on the three polymer-based devices. However, their absorbance spectra do not show significant differences when compared to devices casted from CB+CN. The observed increment in the J_{SC} is not related to a higher aggregation state of the polymers in the blends. Therefore the extent of polymer aggregation in the active layer is not affected by ethanol treatment. As it will be discussed later, the enhancement of the JSC upon EtOH treatment appears rather due to a modification of the recombination mechanisms. Since the EQE spectral patterns change accordingly to absorbance spectra and all the active layers exhibit similar OD, the observed differences in the JSC values are related to different the exciton-to-electron conversion efficiency (IQE – internal quantum efficiency).

The photovoltaic characteristics of BHJs are strongly dependent on blend morphology, directly responsible for charge photo-generation processes, such as exciton dissociation and charge transport. Initially, the surface morphology of blends through processing was analysed by means of AFM measurements.

The tapping mode images of pDHAP, pComm and pStille through processing are reported in fig 2.9. Interestingly, there is a drastic change within the three polymer blends of the AFM morphologies upon CB deposition (line 1). The pStille blend shows a large micro-scale segregation, going to pComm, the extension of these micro-domains is reduced, while in the pDHAP active layer their presence is not detected. This type of pattern has been already observed in other polymer:$PC_{71}BM$ systems and has been ascribed to the formation of large $PC_{71}BM$-rich domains that limit the photon-to-electron conversion[142, 148].

In the PBDTTPD:$PC_{71}BM$ systems, it has been reported that the lower is the tendency of the polymer to aggregate in the blend, the larger is the size of acceptor-rich micro-domains.[144]

The morphology of the active layers casted from CB is the result of the competition between the aggregation of PBDTTPD and the micro-scale segregation of $PC_{71}BM$.

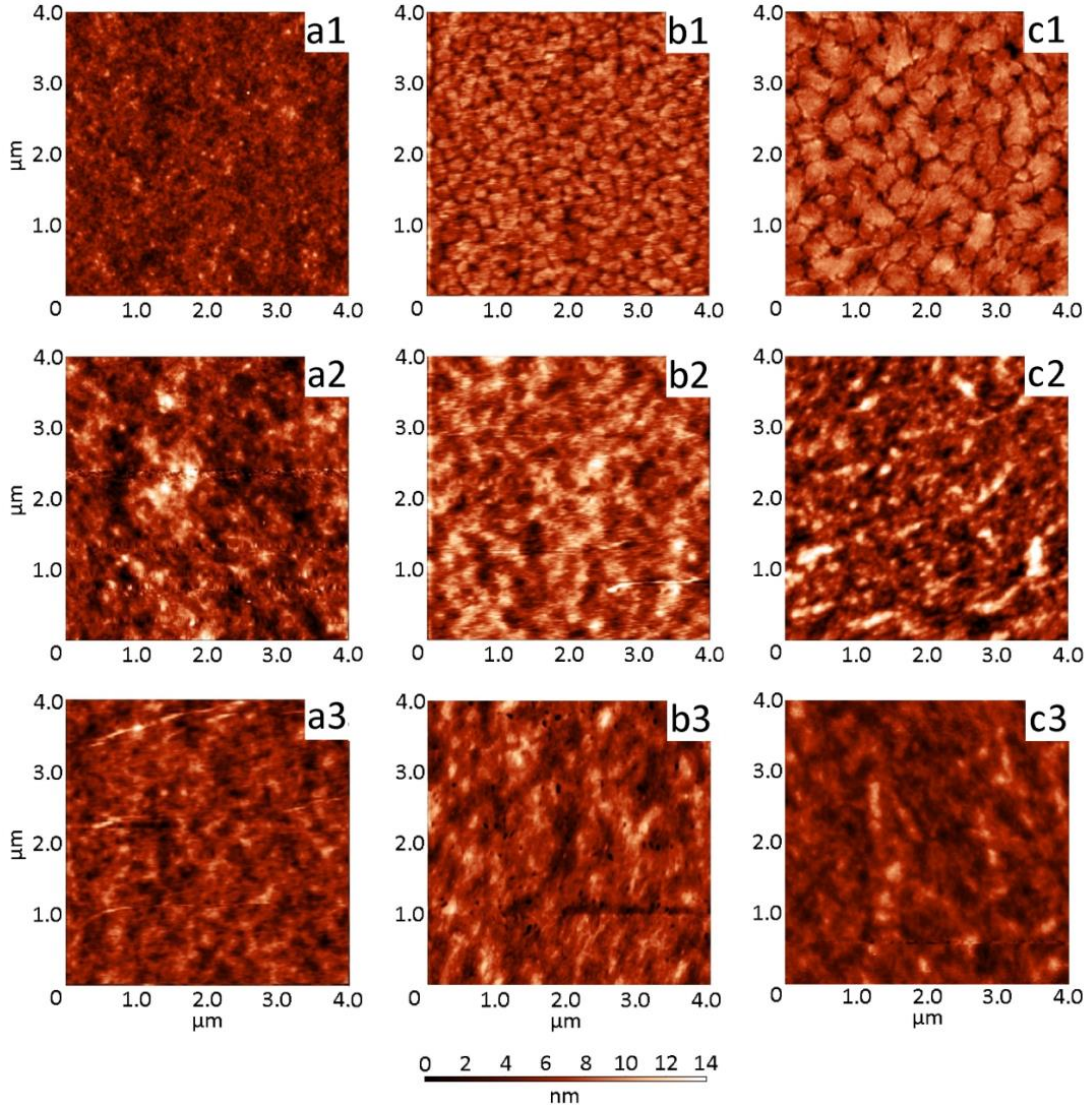

Figure 2.9: AFM images in tapping mode of a 4x4 μm surface of blend of pDHAP (a), pComm (b) and pStille (c) casted from 1-Chlorobenzene (1), 1-Chlorobenzene with 4% w/w of 1-Chloronaphtalene (2) and 1-Chlorobenzene with 4% w/w of 1-Chloronaphtalene subsequently treated with Ethanol (3).

The previously discussed polymer aggregation trend upon CB processing can be related to the J_{SC} values and to the micro-scale morphology. Upon CB+CN processing, (line 2) there is no formation of any micro-segregation pattern, a result in accordance with the general increase of J_{SC}, while no further modification of surface morphology is observed with the further ethanol treatment (line 3).

Subsequently, I verified the possible changing through processing of the nano-morphologies of the blends. The nano-morphology was probed through

photoluminescence quenching measurements, a technique which provides some information about the nano-segregation of donor and acceptor domains in the blend.

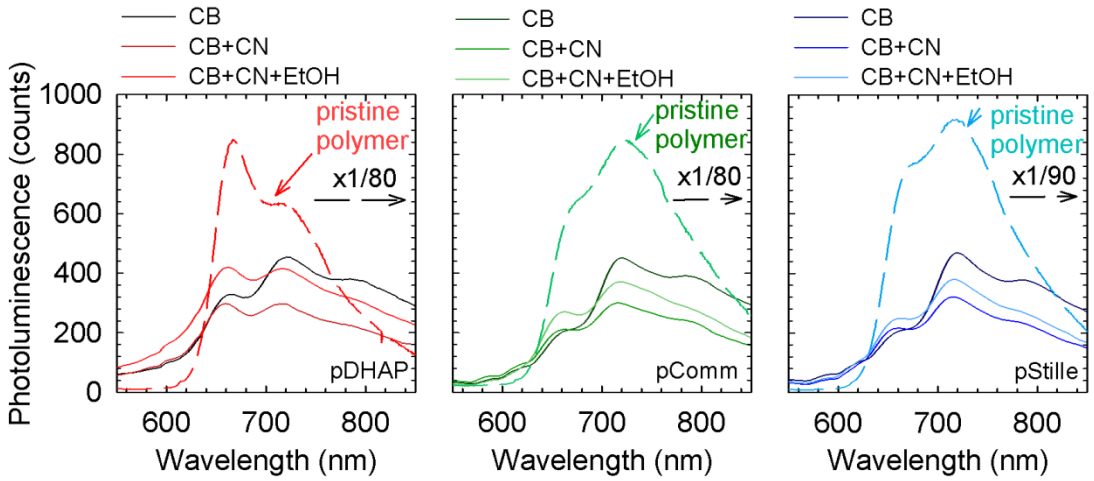

Figure 2.10:. Photoluminescence spectra of blends of pDHAP (red curves), pComm (green curves) and pStille (blue curves) through processing. Pristine polymer photoluminescence spectra are reported in dashed lines. The scale factor between PL spectra in the same plots is reported.

The photoluminescence spectra of the pDHAP, pComm and pStille blended with $PC_{71}BM$ and of the pristine polymers are reported in fig 2.10. The ratio between the photoluminescence intensity of pristine polymer and polymers blended with $PC_{71}BM$ is over 150, indicating that the emission of the donor is heavily quenched, irrespective of the polymer or the processing step. This suggests that, even in blends casted from pure CB where microdomains are observed in the surface morphology, the polymer and fullerene components are very well intermixed at the nanoscale.

Thus the processing has no influence on the nano-morphology of the blend in the three polymers under study. Therefore the lower J_{SC} values cannot be ascribed to a lower exciton harvesting at the donor/acceptor interface, but should be related to a hindrance to charge transport or collection.

Finally, to get some insight on the processes involving charge carriers recombination, the dependence of the photocurrent on incident light power and on internal field was studied. The plots of photo-generated light (the difference between the J measured from JV under illumination and in dark condition) as a

function of electric field inside the cell S (V_0-V where V_0 is the voltage at which J_{PH}=0) for the three blends through the processing are reported in fig 2.11.

Comparing the cells containing PBDTTPD synthetized via Stille (pComm and pStille) with the polymer obtained via DHAP casted from pure CB, it is observed that at high internal fields (near the short circuit condition or at negative bias) the J_{PH} exhibits an elevate dependence on electric field S (dashed line). The internal field dependence of the photocurrent could be due to geminate recombination of charge carriers, i.e. to a hindrance to charge separation of the

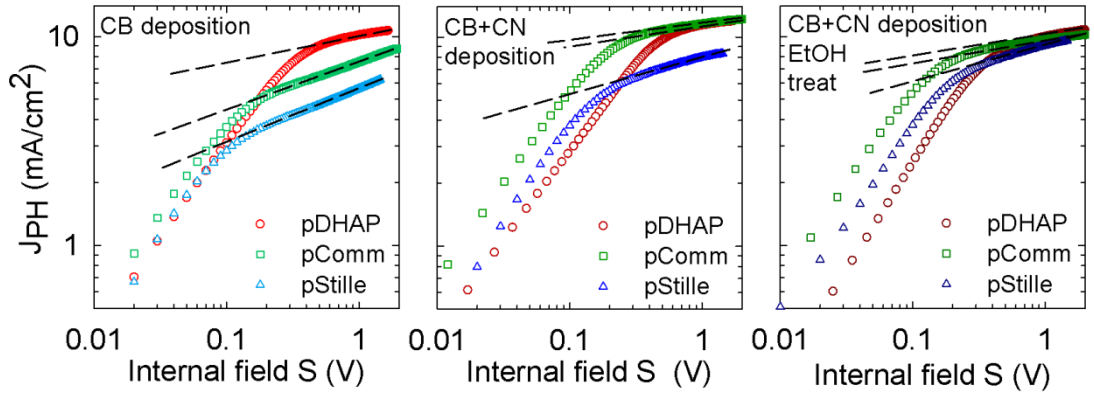

Figure 2.11.: Plot of photo-generated light as a function of internal electric field S for pDHAP (red markers), pComm (green markers) and pStille (blue markers) through the processing

exciton. Since such samples showed a micro-scale segregation (see fig 2.9 b1, c1), it is possible to assume that the geminated recombination of charge carriers is favoured in blends with large $PC_{71}BM$-rich domains. Note that a similar behaviour has already been found in PBDTTPD based devices with low molecular weight by McGehee, who assessed that J_{SC} is limited by the geminate recombination when the absence of polymer aggregation favours the formation of acceptor rich domains[134, 144].

The micro-morphology, as discussed before, is dependent on the molecular weight of the polymer, which in its turn limits the photon-to-electron conversion, resulting in lower J_{SC} for the pComm and pStille-based cells casted from CB. Going from CB to CB+CN and CB+CN+EtOH, no difference in the field dependence of photo-current within the samples is observed. This result

indicates that the J_{SC} is not limited by geminate recombination when the blend is processed by CB+CN or CB+CN+EtOH., which is in accordance with the disappearance of micro-domains, and thus with the enhancing of the J_{SC}, through the processing.

Finally, it is worth analysing more deeply the different evolution of open circuit voltage and fill factor through processing of the pDHAP-based device compared to polymers prepared via Stille coupling.

Here I reported the table 2.4 with the PV parameters. In the pDHAP device casted from pure CB lower values of V_{OC} and FF are observed compared to pComm and pStille (FF: 0.46 for pDHAP versus 0.54 for pComm and pStille; V_{OC}: 0.85 for pDHAP versus 0.91 and 0.92 for pComm and pStille respectively).

Polymer	Processing Solvent	Voc (V)	FF (%)	Jsc (mA/cm²)	η
pDHAP	CB	0.85 (0.86)	0.46 (0.48)	7.80 (7.86)	3.09% (3.27%)
pComm		0.91 (0.91)	0.54 (0.54)	6.88 (7.25)	3.37% (3.55%)
pStille		0.92 (0.93)	0.54 (0.54)	5.46 (5.57)	2.70% (2.80%)
pDHAP	CB + 4% CN	0.77 (0.78)	0.35 (0.36)	8.84 (9.31)	2.39% (2.54%)
pComm		0.86 (0.87)	0.62 (0.62)	9.12 (9.63)	4.84% (5.02%)
pStille		0.89 (0.89)	0.55 (0.56)	7.82 (8.07)	3.82% (4.01%)
pDHAP	CB + 4% CN+EtOH	0.92 (0.92)	0.55 (0.56)	10.07 (10.41)	5.14% (5.31%)
pComm		0.90 (0.92)	0.59 (0.63)	10.1 (10.2)	5.40% (5.71%)
pStille		0.93 (0.93)	0.57 (0.57)	8.82 (9.17)	4.65% (4.82%)

Table 2.4.: PV parameters of optimized devices through processing (casted from 1-Chlorobenzene, 1-Chlorobenzene with 4% w/w 1-Chloronaphtalene, and 1-Chlorobenzene with 4% w/w 1-Chloronaphtalene with further Ethanol treatment) for pDHAP, pComm and pStille. Average value out of 6 devices; values in brackets are the highest values.

This feature might be ascribed to the weak contribution to charge carrier transport arising from the fraction of low weight chains of pDHAP, (PDI=6) .The addition of CN has deeply different effects on the three polymers. In the pComm and pStille based devices the FF shows a slight enhancement, reaching respectively 0.62 and 0.56, while V_{OC} shows a very slight decrease, whereas the pDHAP-based device shows a decrease of FF 0.35 and a V_{OC} drop to 0.77.

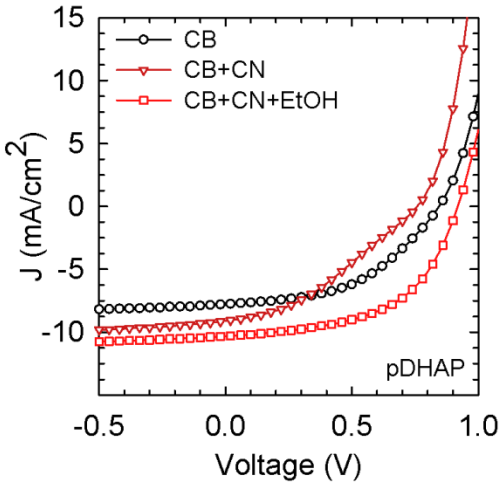

Figure 2.12.: JV characteristics of pDHAP-based devicse through processing.

The J–V curve of the pDHAP-based device casted from CB+CN shows a marked "kink" near the V_{OC} as reported in fig 2.25 (dark red curve). Such feature in the JV plot is a fingerprint of a poor charge extraction property of the device, which might be due to bimolecular recombination. To verify this hypothesis a study about the photocurrent dependence on the incident light power as a function of electrical field was performed.Even though the proposed analysis does not provide a quantitative evaluation of the bimolecular recombination degree, it is a useful tool to get some information about the charge recombination behavior through processing.

The plots of the photocurrent as a function of device internal field S at different incident power were collected and the proportional coefficient α between photocurrent and incident light power ($J_{PH} \propto P_{light\ inc}^{\alpha}$) were calculated at short circuit (S=0.2) and at open circuit (S=1). In fig 2.13 I reported, for instance, the curves for the pDHAP-based cells, while the summarized results of this analysis for the three polymers are reported in table 2.5. At high internal field, i.d. near short circuit (S=1), the values of α coefficient within the samples do not show significant discrepancies and are very close to unity. The almost linear behaviour of J_{PH} with P_{INC} indicates the absence of bimolecular recombination in this condition[149, 150]. At low internal field, i.e.

near open circuit condition (S=0,2), the α coefficient is generally lower as the extraction of charges is less effective.

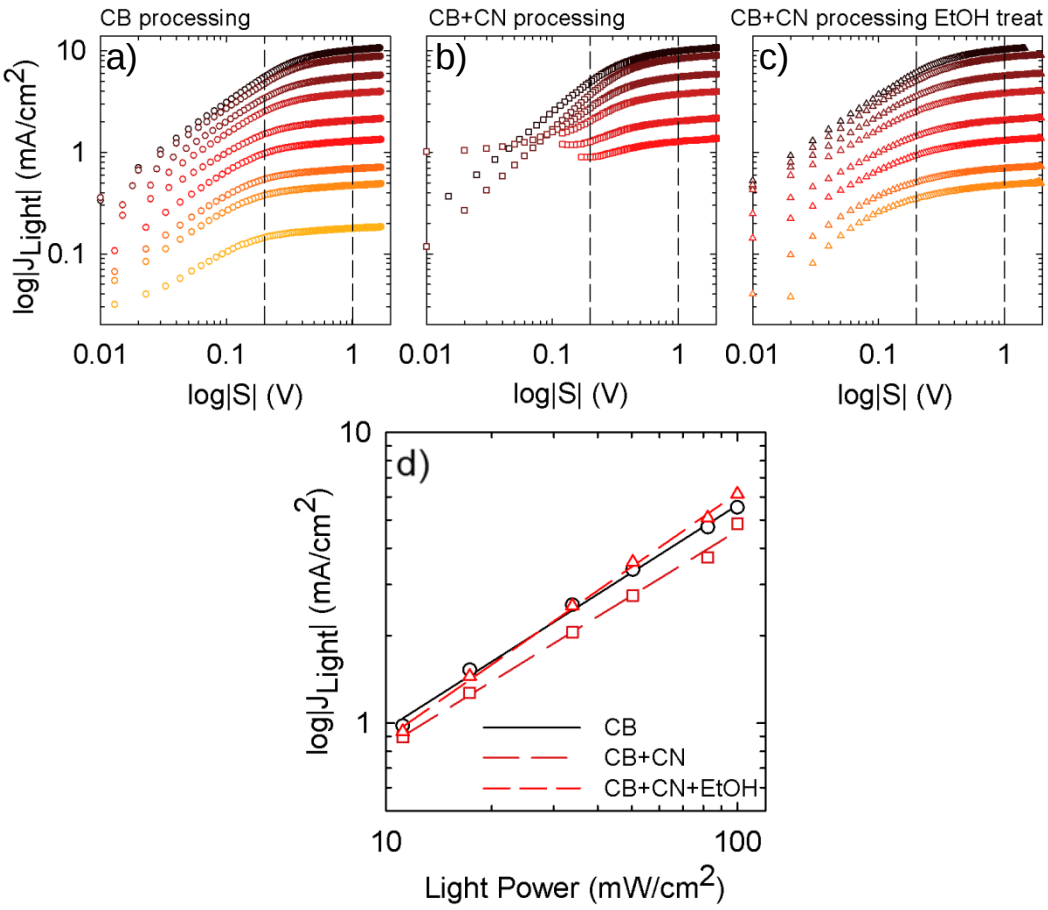

Figure 2.13:a), b) and c) are plots of the photocurrent as a function of internal electrical field S for different incident light power (black 100 mW/cm^2 – orange 8 mW/cm^2). Dashed lines indicated the S values for the calculation of α coefficient; d) plot of the photocurrent as a function of incident light power extracted from a), b), c) with S= 0.2V. Lines indicate the linear fitting for the calculation of α coefficient.

In this condition, there is a higher density of charges, which results in a more pronounced bimolecular recombination. However, in this comparison the α coefficient of pDHAP device casted from CB and CB+CN is significantly lower than pComm and pStille. The different behaviour of recombination in pDHAP-based device can be attributed to its larger molecular weight distribution.

Polymer	Internal field S (V)	α coefficient		
		Processing from CB	Processing from CB+CN	Processing from CB+CN + EtOH
pDHAP	1	0,949	0,970	0,969
	0.2	0,774	0,748	0.913
pComm	1	0,976	0,974	0,979
	0.2	0.940	0,943	0,948
pStille	1	0,967	0,963	0,974
	0.2	0,940	0,882	0,917

Table 2.5.: Values of the α coefficient calculated for pDHAP. pComm and pStille through the processing at different internal electric field (S=0.2V and S=1V)

The very large molecular weight distribution of pDHAP (PDI=6) likely favours a vertical distribution of the polymer in which the short chains fraction tends to be more abundant closer to the top surfaces of the active layer, in proximity of the cathode. Such distribution turns out to be disadvantageous as the short chain fraction typically shows higher concentration of residuals catalyst possibly acting as trapping centres. The employed post-deposition ethanol treatment has the effect of washing the top surface of the active layer resulting in a partial removal of the residual catalyst and the lowest chains fraction. EtOH treatment also positively affected the performances of pStille and pComm devices, enhancing their V_{OC} to 0.90 and 0.93 respectively, without significantly modifying the other PV parameters.

2.4. Conclusions

The photovoltaic performances of PBDTTPD obtained via DHAP, a synthesis fulfilling the scaling-up requirements, were evaluated in comparison with those of the polymers obtained via the Stille cross-coupling reaction, which currently represents the synthetic way of choice for the most performing D–A copolymers. The development of an appropriate experimental condition allowed to obtain optimized devices with all the polymers included in the comparison. The photo-conversion efficiency of optimized devices is 5.14% for

the pDHAP, 5.31% for pComm and 4.65% for pStille. Moreover, through the combination of optical, electro-optical and morphological characterizations, I could highlight the relationship between the macromolecular characteristics of these polymers, which are strongly related to their synthetic preparations, and the PV performance through the processing of the corresponding devices.

Above findings demonstrate comparable photovoltaic performances for the three PBDTTPDs under study, revealing that the DHAP approach is a viable synthetic route to obtain PV grade PBDTTPD. This is particularly remarkable considering the much higher polymer dispersity index of pDHAP compared to the polymers prepared via Stille, which typically does not represent an advantage for PV polymers. On one hand I found that the presence of polymer chains aggregation in pDHAP has a positive influence on the blend morphology, which favours the photon-to-electron conversion. On the other hand, the large broad molecular weight distribution induces a high charges recombination effect, which is a detrimental factor for the device efficiency. However, I found that these recombinations can be effectively reduced through the addition of a supplementary ethanol surface treatment, perfectly compatible with the device solution-processing preparation. This processing allows to reach photo-conversion performances in line with those reported in the literature for OPV grade PBDTTPDs with similar M_N.

2.5. Materials and methods

2.5.1. Materials

(4,8-bis((2-ethylhexyl)oxy)benzo[1,2-b:4,5-b0] dithiophene-2,6-diyl) bis (trimethylstannane) **A,** 1,3-dibromo-5- octyl-4H-thieno[3,4-c]pyrrole-4,6(5H)-dione **B,** 2,6-dibromo-4,8-bis((2-ethylhexyl)oxy)benzo[1,2- b:4,5-b0]dithiophene **C** and 5-Octyl-4H-thieno[3,4-c]pyrrole- 4,6(5H)-dione **D** were purchased from Sunatech Inc. and used without further purification. Pivalic acid, cesium carbonate, tris(o-anisyl) phosphine [P(o-OMePh)3], tri(otolyl)phosphine[P(o-MePh)3], palladium-tetrakis (triphenylphosphine) Pd(PPh3)4 and tris(dibenzylideneacetone) dipalladium(0) Pd2(dba)3 were purchased from Sigma Aldrich and used without further purification.

2.5.2. PBDTTPD Synthesis

Direct Hetero Arylation Polymerization

In a three-necked round-bottomed flask (25 mL), monomer **C** (500 mg, 0.83 mmol), monomer **D** (220 mg, 0.83 mmol), cesium carbonate (541 mg, 1.66 mmol), pivalic acid (26 mg, 0.25 mmol), tris(o-anisyl) phosphine (23 mg, 0.07 mmol) and Pd(PPh3)4 (48 mg, 0.04 mmol) were added. The system was purged three times by vacuum/nitrogen cycles and anhydrous toluene (8 mL) was added. The reaction mixture was heated at reflux for 48 hours. After this time, the polymer was end-capped by adding monomer D (220 mg, 0.83 mmol). The whole mixture was cooled to room temperature and poured in methanol. The solid product was washed with water, recovered by filtration and purified by Soxhlet extraction using methanol, acetone, hexane and chloroform, respectively. The solid residue was dissolved in chloroform (5 mg mL1) and an aqueous ammonia solution (NH4OH) was added (volumetric ratio ¼ 1 : 1). The mixture was refluxed for 5 hours under vigorous stirring and then it was cooled to room temperature. The organic phase was separated and concentrated and the polymer re-precipitated from methanol. A dark solid was recovered by filtration and dried under vacuum at 60 C to yield the target polymer (470 mg,

80%). dH (400 MHz, C2D2Cl4, 90 C) 9.13–7.87 (1H, br s), 4.88–3.17 (3H, br s), 2.49–0.31 (43H, br s).

Stille polymerization

In a three-necked round-bottomed flask (25 mL), monomer **A** (641 mg, 0.83 mmol), monomer **B** (351 mg, 0.83 mmol), tri(o-tolyl) phosphine (10 mg, 0.07 mmol) and Pd2(dba)3 (15 mg, 0.02 mmol) were added. The system was purged three times by vacuum/nitrogen cycles and anhydrous toluene (8 mL) was added. The reaction mixture was heated at reflux for 48 hours. After this time, iodobenzene (93 mL, 0.83 mmol) was added to the reaction mixture and reacted for 4 hours. To complete the end-capping procedure, 2-(tributylstannyl)thiophene (264 mL, 0.83 mmol) was added and reacted for 4 hours. The whole mixture was cooled to room temperature and poured in methanol. The solid product was recovered by filltration and purified by Soxhlet extraction using methanol, acetone, hexane and chloroform, respectively. The solid residue was dissolved in chloroform (5 mg mL1) and an aqueous ammonia solution (NH4OH) was added (volumetric ratio ¼ 1 : 1). The mixture was refluxed for 5 hours under vigorous stirring and then it was cooled to room temperature. The organic phase was separated and concentrated and the polymer re-precipitated from methanol. A dark solid was recovered by filtration and dried under vacuum at 60 C to yield the target polymer (523 mg, 90%). dH (500 MHz, C2D2Cl4, 90 C) 9.20–7.92 (1H, br s), 4.97–3.22 (3H, br s), 2.46–0.32 (46H, br s).

2.5.3. Device fabrication

The devices were assembled with a standard geometry glass/ITO/ PEDOT:PSS/active layer/cathode. Each ITO-glass substrate, Kintec 15 U/sq , was mechanically cleaned with wet paper and then washed in an ultrasonic bath at 55 C, sequentially with water, acetone and isopropanol. Subsequently, the substrates were left in an isopropanol bath for 1 h. After drying under a compressed nitrogen flow, the substrates underwent 10 minutes of plasma

treatment. Next, PEDOT:PSS (Clevios VP Al 4083) was spin coated at 2000 rpm for 60 seconds (40 nm thick) and dried in air on a 100 C hot plate for 10 min. After annealing, the hot substrates were inserted into a glovebox where the device assembling was completed. The polymers and PC71BM (Solenne BV, 99% purity) were dissolved at the composition of 1:1.5 weight ratio in chlorobenzene (CB), with a solute concentration of 20 mg/mL . The solutions were stirred overnight at 85° C, prior to spin coating deposition. Some active layers were prepared by adding 4% in volume of 1-Chloronaphthalene (CN) to the CB solutions. The active layers were spin coated at 1800 rpm for 90 seconds: under these conditions film thicknesses were ~70 nm. Some samples underwent a further surface treatment with ethanol: 200 mL of ethanol were dropped on active layers immediately after its deposition. Ethanol treated devices were subsequently spin coated at 2000 rpm per 60 seconds in order to remove the excess solvent. The films were left in a glovebox for 1 hour before the cathode evaporation. Finally, a 30 nm calcium layer and a 100 nm Al layer were thermally evaporated, through a shadow mask under a pressure of 2.10^{-6} mbar. The deposition rates were respectively 0.1 nm s1 and 0.7 nm/s for Ca and Al. There were 6 devices on a single substrate and each with an active area of 6.1 mm^2 .

2.5.4. Experimental

13C NMR spectra were acquired on a Varian INOVA 400 spectrometer at 100.61 MHz and 1 H NMR spectra were acquired on a Varian INOVA500 spectrometer at 500.13 MHz. Molecular weight calibration was carried out using polystyrene standards. GPC analysis of the commercially available PCOMM was performed under the same conditions of PDHAP and PSTILLE in order to carry out a homogeneous comparison. UV-Vis spectra of the polymers were recorded on a SHIMADZU UV-2401PC.

Atomic force microscopy (AFM) investigations were performed using a NT-MDTNTEGRA apparatus in tapping mode under room conditions.

The current density–voltage measurements were performed directly in the glovebox where the solar cells were assembled, with a Keithley 2602 source meter, under AM 1.5G solar simulation (ABET 2000). The incident power, measured with a calibrated photodiode (Si cell + KG5 filter), was 100 mW cm^2. The EQE spectral responses were recorded by dispersing a Xe lamp through a monochromator, using a Si solar cell with a calibrated spectral response to measure the incident light power intensity at each wavelength. The devices were taken outside the glovebox for the EQE measurements, after mounting them on a sealed cell to avoid moisture and oxygen exposure.

3. Poly-fluorene-based cathodic interlayers for PSC

3.1. Abstract

In the last section of my thesis I studied a novel poly-fluorene-based (PFN) material as cathode interfacial material (CIM) for polymeric solar cells with direct geometry. The conjugated polyfluorene backbone was functionalized with two side groups: alkyl-ammonium bromide (NBr) and ethyl-phosphonate (EP) groups. The proposed CIM was designed considering the features of both NBr and EP functionalities: the first exhibits a dipole moment which ensures high solubility in polar solvent and an effective work function modification, while the latter is reported to exhibit a selective interaction between the phosphonate group and aluminium. The complete study through photoelectric, electric and morphologic characterization techniques highlighted an enhancement of charges extraction and a reduction of active layer/electrode interfacial recombinations due to the effective surface engineering upon insertion of a thin layer of PFO-NBr-EP. Consequently the BHJ solar cells based on PTB7:$PC_{71}BM$ blends with CIM/Al as cathode showed an enhancement of the PV parameters compared to the pristine bare Al devices, resulting in 7.24% PCE, (60% improvement). The inclusion in the study of a third device, on which a surface

treatment with alcohol was performed, allowed to discriminate the contribution of EtOH surface treatment from the effect of CIM insertion to the increased photovoltaic performance of the finale device.

In the last section, I will discuss the effect of the side group moieties on the device stability, through a comparison with other PFN-based not yet used as CIM for PTB7:$PC_{71}BM$-based solar cell devices.

3.2. Materials

Water/alcohol soluble conjugated polymers are a class of interlayer materials that and have shown great success in the interfacial engineering of PLEDs and BHJ[127, 151-153]. For solar cell device in particular, among the several classes of conjugated functional polymer, polyfluorene-based (PFO) interlayer have shown great success as cathodic interlayer material (CIM) in increasing device efficiency in direct and inverted structures[154, 155]. Their structure, which is composed by a π-conjugated PFN backbone and a surfactant-like solubilizing side chain (amino phosphonate, phosphonate, carboxyl or sulfonic groups) offers a series of advantages regarding both their processability and their optical/electrical properties[156-160]. Firstly. the side groups confer an excellent solubility in high polar/polar solvents, which meets the growing demand for environmental friendly materials and allows a deposition from orthogonal

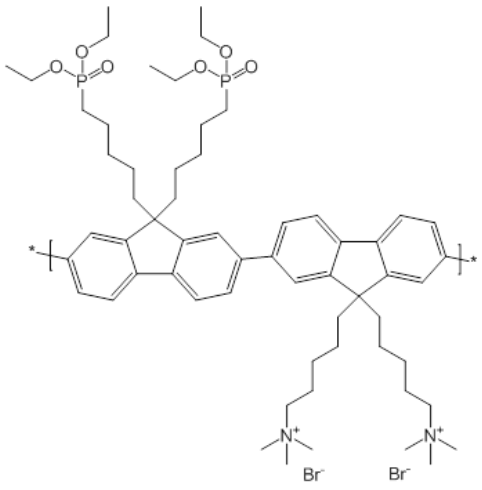

Figure 3.1.: PFO-NBr-EP structure

solvents compared to those used for active layer deposition. Secondly, the high polar side groups effectively induce a work function modification of electrode[96] which is an efficient strategy for the surface engineering of BHJ devices by increasing contact omhicity, and the built-in voltage. Finally their presence avoids the damaging of underlying active layer by the deposition of metal electrode.

In this study I used a novel PFO-based interlayer material, poly[(2,7-(9,9'-bis(6'-diethoxylphosphorylhexyl)-fluorene)-alt-(2,7-(9,9′-bis(6″-trimethylammonium bromide) hexyl)- fluorene)])] (PFO-NBr-EP) bearing alkyl side chains with alternated-ammonium bromide (NBr) and ethyl-phosphonate (EP) groups. On one hand, NBr functionality, which has already been used as side chain terminal group in several copolymeric interlayer[157, 161-163], is reported to induce a large interfacial dipoles between the active layer and the high work-function metal cathodes[164, 165]. On the other hand, EP functionality shows an intense coordination ability with Aluminium, the typical metal for cathodes in direct devices, which can be exploited to obtain a protective effect on the interface with the electrode[152]. Despite the apparent complexity of the copolymer, its synthesis requires just one additional step compared to PFO-based polymers with one side chains functionalization. The increasing commercial availability of its reagent and the easy synthetic routes make PFO-NBr-EP a good candidate as high-performing non-expensive CIM for BHJ[127].

In the last section of the study, a second PFO-base polymer with only EP functionalization (poly[(2,7-(9,9'-bis(6'-diethoxylphosphorylhexyl)-fluorene)-) is used as term of comparison. The synthesis of PFO-NBr-EP and PFO-EP was performed at the chemistry laboratories of ISMAC group at Consiglio Nazionale delle Ricerche CNR in Milan.

3.3. Results

3.3.1. Photovoltaic study

CIM was tested using a conventional device configuration, consisting of Glass/ITO/PEDOT:PSS/PTB7:$PC_{71}BM$/PFO-NBr-EP/Al whose structure and layers thickness are shown in fig.3.2.

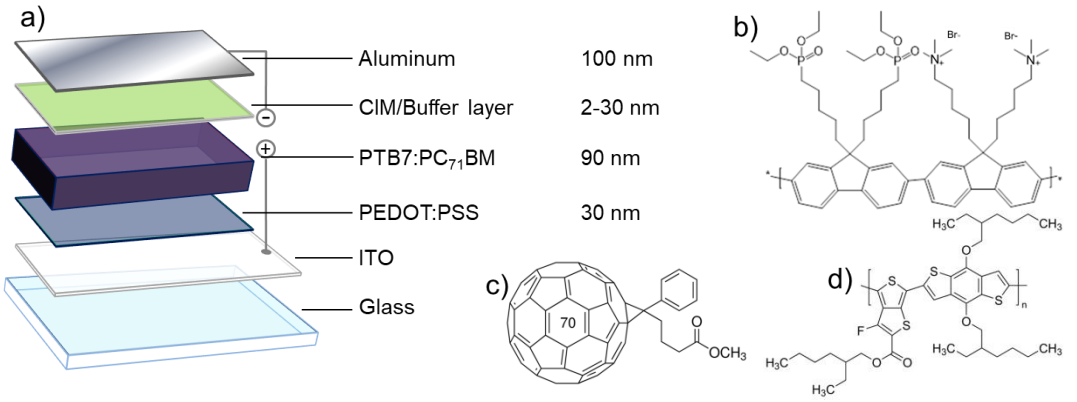

Figure 3.2.: Structure of the assembled device and corresponding average thicknesses (a); structures of interlayer (b), acceptor (c) and donor (d.)

The recipe used for the PTB7:$PC_{71}BM$ processing was taken from ref [166]. 4-Anisaldehyde (AA) was chosen as additive to chlorobenzene for processing the active layer. In PTB7:$PCBM_{71}$ blends, AA was reported to be almost as effective as 1,8-Diiodooctane (DIO) additive in terms of device performance, but its higher vapour pressure ensures a faster and more complete drying of active layer, resulting in a better morphological stability in time without the necessity of further washing step to remove additive residues[166].

PFO-NBr-EP was deposited on top of active layer from ethanol solution and its thickness was optimized by varying the solution concentration and measuring the JV characteristics of the corresponding device, which are reported in fig Fig 3.3, while the related PV parameters are reported in table 3.1. From this initial result, it is evident that PFO-NBr-EP thickness does not significantly affect the open circuit voltage (V_{OC}), since all values are in the range 0.73-0.75 V, while the fill factor (FF) and short circuit current (J_{SC}) are

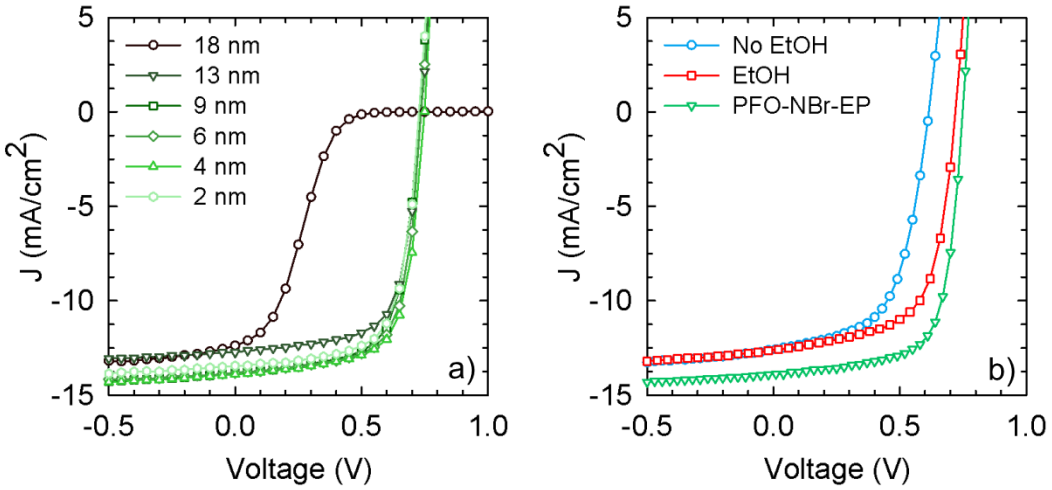

Figure 3.3.:a) JV characteristics of PTB7:$PB_{71}BM$ solar cells with different PFO-NBr-EP thickness; b) JV characteristics of PTB7:$PC_{71}BM$ solar cell without CIM (blue line), with EtOH treatment (red line) and with optimized PFO-NBr-EP thickness (green line)

Sample	CIM Thickness (nm)	V_{oc} (V)	FF	J_{sc} (mA/cm²)	Eff (%)	Eff *(%)
No EtOH	-	0.61	0.591	12.54	4.53	4.69
EtOH	-	0.7	0.64	12.85	5.81	5.97
5 mg/ml	18	0.74	0.205	12.37	1.88	2.09
2 mg/ml	13	0.73	0.545	12.54	4.92	5.12
1 mg/ml	9	0.74	0.682	12.75	6.44	6.55
0.7 mg/ml	6	0.74	0.691	13.83	7.07	7.24
0.5 mg/ml	4	0.75	0.693	13.86	7.24	7.38
0.2 mg/ml	2	0.73	0.686	13.44	6.73	6.88

Table 3.1.: PV parameters of a PTB7:PC71BM solar cells with different PFO-NBr-EP thickness. Average value out of 6 devices; values in brackets are the highest values.

dependent on the CIM thickness (table 3.1). The solar cell containing layer of PFO-NBr-EP casted from a 0.5 mg/ml solution (corresponding to a 4 nm PFO-NBr-EP thickness) was found to be the best performing device, with a 7.24% PCE which most studied PFN based cathode interlayers in direct solar cells with PTB7:$PCBM_{71}$ blend were reported in literature to provide improvements in the range 30-65% compared to device without interlayer[167].

PFO-NBr-EP films casted from solutions with concentration lower than 0.5 mg/ml do not uniformly cover the active layer, resulting in devices with very low reproducibility. PFO-NBr-EP films casted from solutions with concentrations higher than 2 mg/ml, results in JV curves exhibiting a marked S-

shape with an evident drop in FF, a fingerprint of hindered charges extraction[145]. This feature can be explained considering that electron extraction through interlayer material takes place by tunnelling. Too thick CIMs (>10 nm), beside preserving the interface engineering act as electron blocking layer, forming a barrier which hinders charges extraction[162, 168].

To get some insight on how the presence of PFO-NBr-EP affects the PV performance of the device, I compared the best performing device with PFO-NBr-EP with a device without CIM (untreated sample). However, since the deposition of PFO-NBr-EP on active layer is performed by spin-coating from an ethanol solution, I included in the comparison also an ethanol treated (ET) device. Washing the top surface of active layer with bare methanol or ethanol is a well-established tool to engineer the active layer interfaces[145, 169, 170]. In many reported papers, this effect is enhanced by subsequent alcohol washings or even by soaking the active layer with alcohol drops[170]. In my case, these two techniques did not show any further benefit compared to simple ethanol treatment. For this reason I limited the comparison to a device which underwent a single surface washing with ethanol.

In fig. 3.3b, JV curves under solar simulator of untreated sample, ET sample and sample with optimized PFO-NBr-EP thickness are reported, while the corresponding PV parameters are listed in table.3.1. The comparison between untreated devices with ET device highlights a large increase in V_{OC} (from 0.61 V to 0.71 V) and in FF (from 0.591 to 0.640) and a reduction of series resistance (from 7.69 to 5.20 $\Omega \bullet cm^2$). The JV curves in dark condition, shown in fig. 3.4, highlight a lower dark current for the ET device compared with untreated device at low positive bias, which combined with the rise of FF and the reduction of series resistance indicates an enhanced charge extraction capacity.

A similar trend in a PTB7:PC71BM system which underwent methanol treatment was reported by Kumar et al. who addressed these modifications to a suppression of recombination at the electrode, resulting in a better holes-

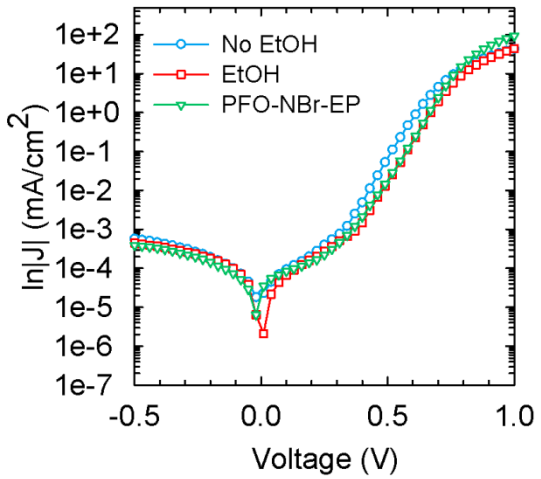

Figure 3.4.JV characteristics in dark condition of PTB7:$PC_{71}BM$ solar cell without CIM (blue line), with EtOH treatment (red line)and with optimized PFO-NBr-EP thickness (green line)

extraction ability of the device, mainly due to an increased conductivity of PEDOT:PSS layer after methanol treatment[145]. However, as some paper reported, it has also been proposed that alcohol treatment could positively affect also the top interface of active layer[170]. The device containing the PFO-NBr-EP layer shows a higher increase in V_{OC} (0.75V), FF (0.693) and a reduction in series resistance (4.23 Ω •cm^2).

The rise of V_{OC} combined with the reduction of series resistance and the rise of FF are hints of an improvement in charges extraction as will be shown in the following from the impedance spectroscopy measurements. The further rise of V_{OC} upon PFO-NBr-EP deposition can be ascribed to the presence of an interfacial dipole layer between active layer and Aluminium which shifts the vacuum level of Al cathode. The polarity of the PFO-NBr-EP layer is due to the presence of its side chains terminal polar groups.

For what J_{SC} modification is concerned, the device containing PFO-NBr-EP shows an improvement of photocurrent (13.86 mA/cm^2) compared to the untreated device and the ET device (12.54 mA/cm^2, 12.85 mA/cm^2 respectively). The enhancement of J_{SC} induced by the presence of PFO-NBr-EP

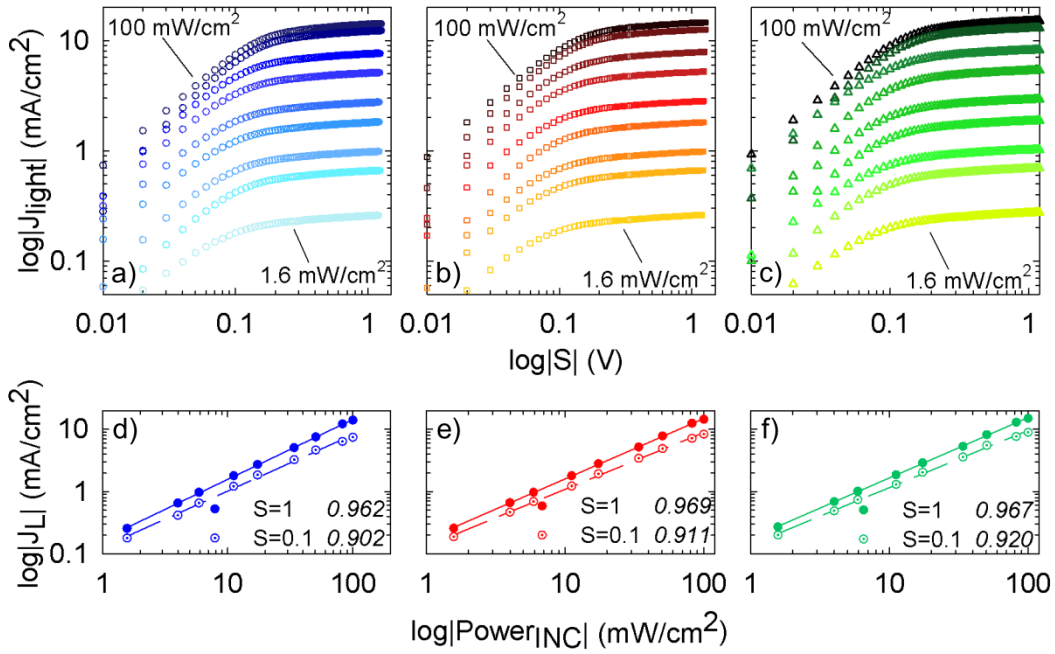

Figure 3.5.: a), b) and c) are plots of the photocurrent as a function of internal electrical field S at different incident light power (dark lines 100 mW/cm^2 – light lines 1.6 mW/cm^2); d), e) and f) are plot of the photocurrent as a function of incident light power extracted from a), b), c) with S= 1 V (filled circles) and S=0.1V (dotted circles). Lines indicate the linear fitting for the calculation of α coefficient.

layer can be explained considering that also a very thin CIM layer could act as optical spacer, modifying the interference phenomena of incident light inside the multilayer structure as demonstrated by Li et al. in similar PFO derivatives[171].

The modification of charge extraction with interfacial engineering should also influence the charges recombination[126]. In order to assess if the interfacial engineering has a positive effect also on hindering charge recombination, I measured and compared the relation between photo-generated current and incident light intensity, $J_{LIGHT} \propto P_{INC}^{\alpha}$, reported in fig 3.5. Even though the proposed analysis does not provide a quantitative evaluation of the bimolecular recombination degree, it is a useful tool to get some information about recombination phenomena in relation with the interfacial engineering.

In the proximity of short circuit condition, i.e. at high internal fields (S=1), the proportional coefficient α does not show relevant differences, being respectively 0.962, 0.969 and 0.967 for untreated device, ET device and device

with PFO-NBr-EP respectively. When V is shifted to the proximity of the V_{OC}, i.e S=0.1V. at low internal fields, the α decreases respectively to 0.902, 0.911 and 0.920. The general decrease of α at low internal electric field suggests that the bimolecular recombination at low internal field is generally more pronounced, which is an expected result when the density of charges inside the device is higher.

However, differently from what happens at high internal electric field, where no significant difference among α coefficients is observed, interestingly in this conditions a trend of α is noticed. Going from untreated device to PFO-NBr-EP containing device, the α coefficient increases, a feature which is coherent with the improved charge extraction capability of the devices and proving that the recombinations are partially curtailed by ET and, even more effectively, by PFO-NBr-EP. This beneficial effect correlates with the improved charges extraction imparted by the active layer/CIM interfacial engineering[126]. These features show how the poor charge extraction feature of untreated device, thus favouring recombination processes at the interfaces, can be improved through the deposition of PFO-NBr-EP from ethanol, which can relieve those mechanisms with an engineering active layer interface.

3.3.3. Electrical properties

The beneficial effects of PFO-NBr-EP as interlayer were probed also through Impedance Spectroscopy (IS) measurements, a non-invasive technique which can be used to study the electrical modification of the BHJ induced by the interfacial engineering[172].

Initially, Nyquist plots of the untreated, ET and PFO-NBr-EP containing devices were collected and reported in fig 3.6. From the Nyquist plots, a fitting with a proper electrical circuit has to be done in order to highlight the electrical functioning of the cell and obtain the values for resistance and capacitance of the device[173, 174]. The electrical circuit used in this case is reported in fig 3.7. The inverse squared parallel capacitance of the equivalent circuit is plotted as a function of external applied voltage in the so-called Mott-Schottky. From Mott-Schottky plot two parameters are finally extracted: the built-in voltage (V_{BI}) which, in organic devices, can be interpreted as the external applied potential necessary to reach the flat band condition, and the relative dielectric constant (ε_R) of the multilayer material sandwiched between the electrodes. Fig. 3.8 shows the Mott-Schottky plots of untreated device, ET device and device

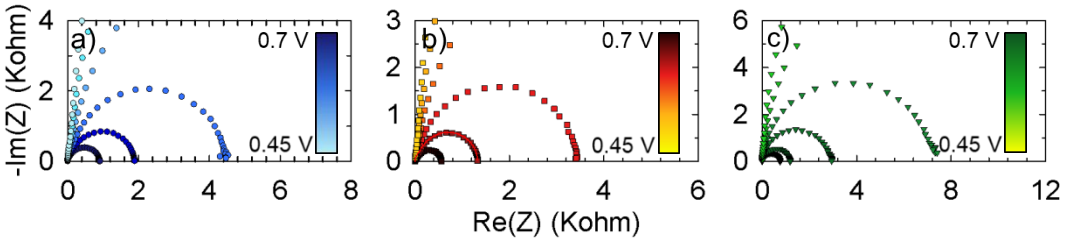

Figure 3.6.: Nyquist plots of untreated device (a), ET device (b) and device containing PFO-NBr-EP (c) at different applied bias in dark condition.

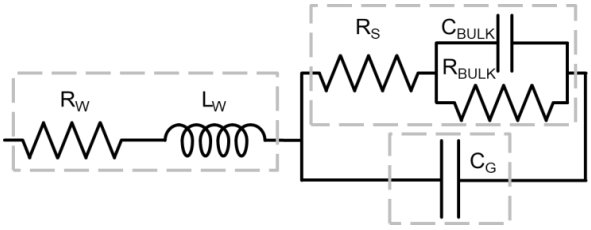

Figure 3.7.: Equivalent electrical circuit used for the fitting of the Nyquist plots reported in a), b), c). R_W and L_W are the resistance and the impedance of the wires connection, C_G corresponds to the geometrical capacitance of the depleted device, and R_S, C_{BULK} and R_{BULK} are the elements representing the behavior of the device during the applied voltage swift.

containing PFO-NBr-EP. The V_{BI} is extracted as the voltage above which the C^{-2} curves in the positive region of V no longer exhibit a linear dependence with the voltage, indicating the transition from the depletion to the injection regime[172, 175]. The V_{BI} extracted, highlighted with arrows in the fig. 3b-d, are increasing going from the untreated device (0.631V) to ET device (0.713V) to the device containing PFO-NBr-EP (0.756V). This observed trend through interfacial engineering is coherently related to the variation already observed for the V_{OC}. From the negative bias region an estimation for the ε_R of the multilayer can be derived. At high negative voltage, the total charge depletion condition is reached and the measured capacitance is equal to the geometrical capacitance (C_G) of a capacitance with the same geometry of the device. From the C_G, ε_R can be calculated as $\varepsilon_R = C_G \cdot d/\varepsilon_0 \cdot S$ where d is the thickness of the device and S its area.

For untreated device a 3.42 value was found, which is in good agreement with the 3.5 value reported in other work for PTB7:PCBM71 blend, while ET and PFO-NBr-EP induce an enhancement of ε_R up to 3.92 and 4.24 respectively. These results indicate a progressive enhancement of polarity, which in the

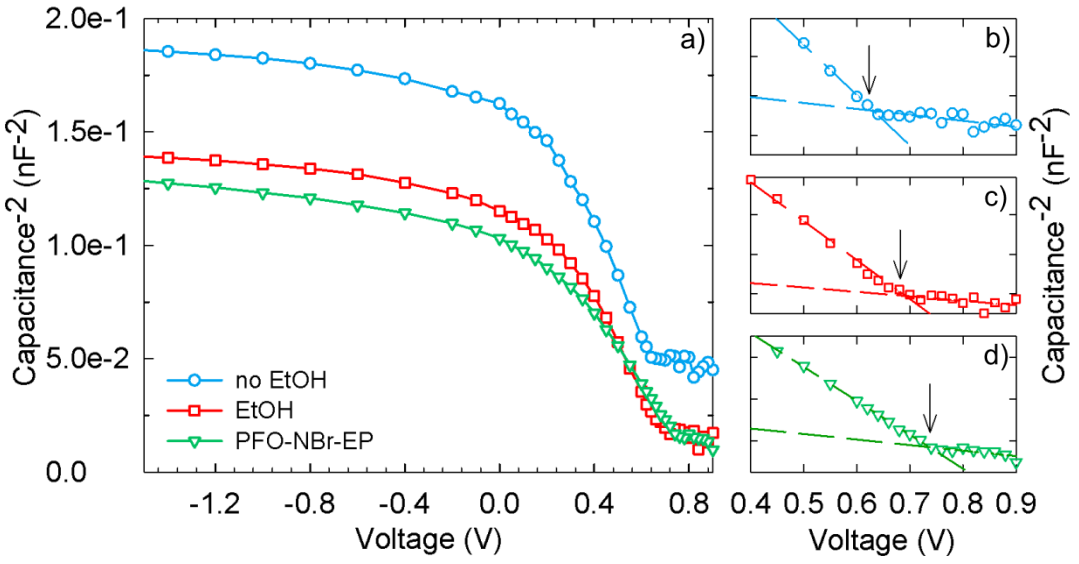

Figure 3.8: (a) Mott-Schottky plots of untreated device (blue circles), ET device (red squares) and device with PFO-NBr-EP (green triangles); enlargement of Mott-Schottky plot in the 0.4-0.9V region for the extraction of V_{BI} from untreated device (b), ET device (c) and device with PFO-NBr-EP (d)

multilayer can be ascribed mainly to a modification of surfaces polarity, since the inner active layer blend was already demonstrated not to be affected by surface engineering. On one hand the polarity of ethanol induces a modification at the active-layer/PEDOT:PSS interface, as already reported in other papers (ref. [176]), while on the other hand, PFO-NBr-EP contains functionalities with highly polarizable groups (NBr in particular) which form a polar thin layer at the active-layer/Al interface[177]. The complete study performed through photoelectrical, electrical and surface characterizations clarify that the increased performances of the device containing PFO-NBr-EP are due to a combined effect of the CIM and alcohol. The modification of ε_R and an enhanced surface potential confirm that FPO-NBr-EP form a polar layer at the active-layer/Al interface. The polarity of interfacial layer induces a modification in the work function of the aluminium electrode, which has a direct consequence on the anode-cathode offset of the device, as confirmed by the enhanced V_{BI}. The modification of the aluminium work function results in a better level alignment between the cathode and the electronic level of active layer. Such feature is observed by considering reduction of the R_S and increase of FF, which are both hints of a better ohmicity of the active-layer/electrode contact.

3.3.4. Degradation measurements

Besides performances, stability is one of the key properties to assess when testing a novel functional material for polymeric solar cells. To investigate the influence of PFO-NBr-EP on the device stability, I compared the shelf life of a set of devices prepared using different combinations of metal electrodes and/or CIM layers. First I compared the shelf stability of the device with PFO-NBr-EP/ Al as cathode with a control device made with a Ca/Al electrode whose low work function ensures a good pinning/ ohmic contact to the active layer but is known to be highly reactive. The variations of the PCE versus storage time for the devices without encapsulation, kept either in the glovebox or in room atmosphere are displayed in fig. 3.9.

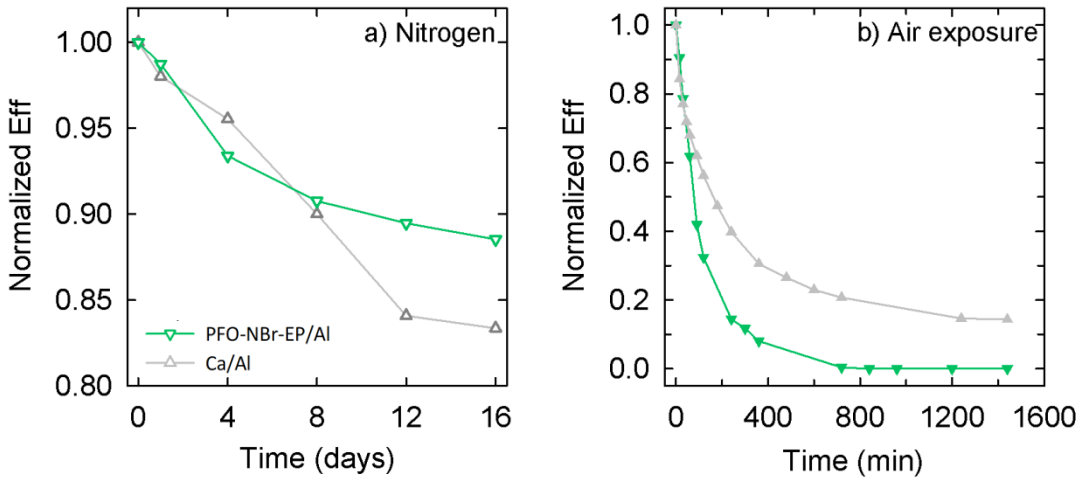

Figure 3.9.: a) Normalized efficiencies as a function of storage time of devices with Ca/Al and PFO-NBr-EP/Al as cathode; in inert atmosphere (a) and in room atmosphere (b)

After 12 days of storage in the glovebox, where the exposure to moisture and air is minimized, the PCE of the device containing the PFO-NBr-EP/ Al cathode retained 90 % of its initial value while the device with Ca/Al retained just 84 % of its initial PCE. Fig.3.4 evidences that the device made with PFO-NBr-EP/Al shows better stability than the device made with Ca/Al when stored in the glovebox. Moreover, as inferred from the kinetic of degradation reported in fig.3.9a, such differences are expected to increase further for longer periods of storage.

The storage in room atmosphere, see fig. 3.9b, notably speeds up the device degradation because of the moisture and/or oxygen exposure. Such characteristics are ascribable to the combined degradation of the cathode, of PEDOT:PSS and of the active layer as well[178-180]. Interestingly, unlike to storage in the glovebox, under room atmosphere the presence of PFO-NBr-EP induces a much faster degradation compared to Ca. The time necessary to reduce to 50% the initial PCE (T_{50}) is 150 mins for the Ca/Al device and it is reduced to 70 mins for the device made with the PFO-NBr-EP/Al. Note that a similar result was also reported in one of the few papers appeared in the literature that discusses the stability of the devices under conventional geometry, which highlighted that the hydrophilic nature of the CIM materials is detrimental to the metal electrodes, in particular to Al[181]. Furthermore, this paper reported a similar trend to fig.

3.9b, i.e. a faster degradation than Ca/Al when using a polar hydrophilic CIM/Al cathode.

For sake of comparison, I measured the decreasing of performance in time of a device containing another PFN-based interlayer, PFO-EP, a CIM fully substituted with only the phosphonated side group, which has been widely used in direct and inverted BHJ[96, 126]. The degradation under room atmosphere of device containing PFO-EP is notably slowing down (fig. 3.10a) compared to the PFO-NBr-Ep interlayer and even to CaAl, even though angle contact measurements (fig 3.10b) revealed this to be more hydroscopic than the PFO-NBr-EP. In this case, the T_{50} time of PFO-EP based device is 360 min, 2.5 time longer than for CaAl and more than 5 times longer than the PFO-NBr-EP device. One of the reasons that prompted us to insert phosphonated groups in the side chains of the novel PFO CIM here under study was the strong interaction among this side group and the Al electrode[152, 182]. The improved stability obtained with the PFO-EP suggests that the strong interaction among the phosphonated groups and the Al electrode is indeed playing a role in slowing down the Al degradation. Therefore, the speeding up of the Al oxidation induced by the intrinsic hydrophilicity of the CIM materials seems to be counterbalanced by the phosphonated interaction to the Al electrode when the PFO-EP is used as CIM

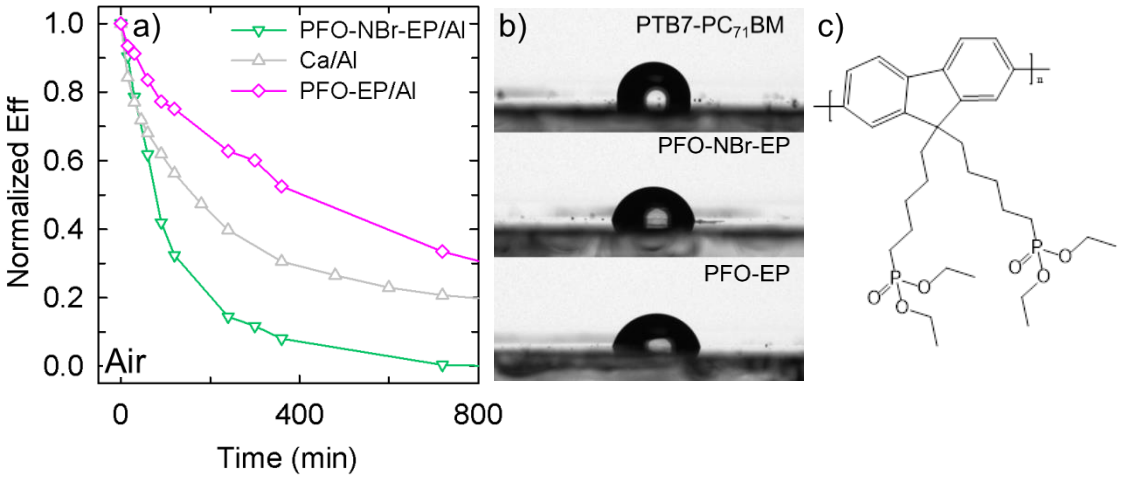

Figure 3.10.: a) Normalized efficiencies as a function of storage time for devices with Ca/Al, PFO-NBr-EP/Al and PFO-EP/Al as cathode; b) contact angle measurements with water of PTB7:$PC_{71}BM$ without treatment,

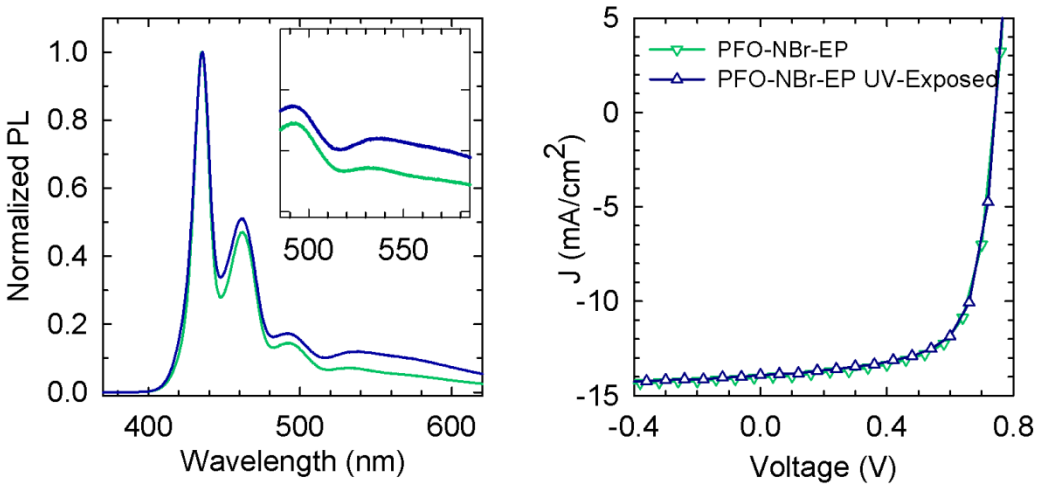

Figure 3.11.: a) Photoluminescence spectra of PFO-NBr-EP films casted from solution not exposed to UV light (green) and exposed to UV light (blue), with the inset highlighting the spectral region of the PFO-NBr-EP fluorenone specie emission; b) JV characteristics of PTB7:$PC_{71}BM$ device with untreated (green) and UV treated (blue) PFO-NBr-EP.

layer. When the number of phosphonated groups linked to the side chains is reduced, as in case of PFO-NBr-EP, the kinetics of degradation under room atmosphere is mostly influenced by the hydrophilicity of the CIM material rather than from the protective role of phosphonated groups.

Due to the easy oxidation of PFO-derivatives under room atmosphere, it is reasonable to suppose that the observed fast degradation of devices upon interlayers deposition coluld be related to the relatively easy photo-oxidation of their PFO backbone. PFO derivatives easily suffers from the attack of oxygen in the meso-position of its backbone, generating fluorenone species[183, 184]. To verify whether the PF photo-oxidation could eventually play some role in the observed device degradation, I prepared some freshly made devices using a PFO-NBr-EP ethanol solution that was exposed to a high intensity UV light (4500mW/cm^2), prior to deposition, to induce some oxidation of the PF backbone. Evidences of the formation of a fluorenone species can be easily detected from the modification of the photoluminescence profile of its film[185]. The photoluminescence of the film of untreated and treated PFO-NBr-EP solutions and the JV characteristic of corresponding devices are reported in fig 3.11. Even though the PL profile of UV-treated film exhibit an higher low-energy features arising from the formation of fluorenone species, confirming thus the partial oxidation of the CIM[186], no differences in the photovoltaic performances of the two devices were detected. These features are ruling out that the CIM

photo-xidation plays anyhow a central role in the observed degradation of the PV performances of the devices kept outside the glovebox.

To get further insights about the devices stability, I analysed the difference in the evolution of the PV parameters with time of storage outside the glovebox for devices with different CIM/cathode combinations. In this study I took into account the devices made with the PFO-NBr-EP and PFO-EP CIM/Al cathodes, taking the bare Al as reference device instead of Ca/Al. In order to focus just on the differences arising from the cathode interfacial layer, I opted to minimize the differences at the anodes, taking an Al device that underwent ETOH treatment prior to the Al evaporation.

The J-V curves as a function of storage time for PFO-NBr-EP devices are reported in fig. 3.12 a and b, while the variation of the PV parameters are depicted in fig. 3.12 c-h. Considering the set of devices with Al as cathode electrode, the PCE degradation in time arises basically from a drop of the J_{SC} parameter upon exposure to room atmosphere. This feature was suggested to be the fingerprint of the formation of insulating aluminium oxide islands at the inner active-layer/Al interface which progressively reduce the surface of the cathode available for the collection of charges and thus the J_{SC} [183]. The formation of a kink in the fourth quarter upon aging is also observed, which is indicative for a growing barrier to charge carrier extraction with storage time[187]. Such hindrance to charge extraction is indeed consistent with the just mentioned formation of the insulating oxide at the Al electrode.

It has been reported that also the hydroscopic nature of PEDOT:PSS layer facilitates moisture diffusion into the device, favouring the formation of Al oxide islands at the active layer/Al interface under room atmosphere. For this reason, after only 1 day of storage under room atmosphere, the Al control device retains only about 15 % of its PCE initial value[187, 188]. With PFO-NBr-EP there is a faster and more significant drop of the J_{SC} and PCE that indicates that the oxidation of the Al electrode is speeding up because of the CIM interlayer.

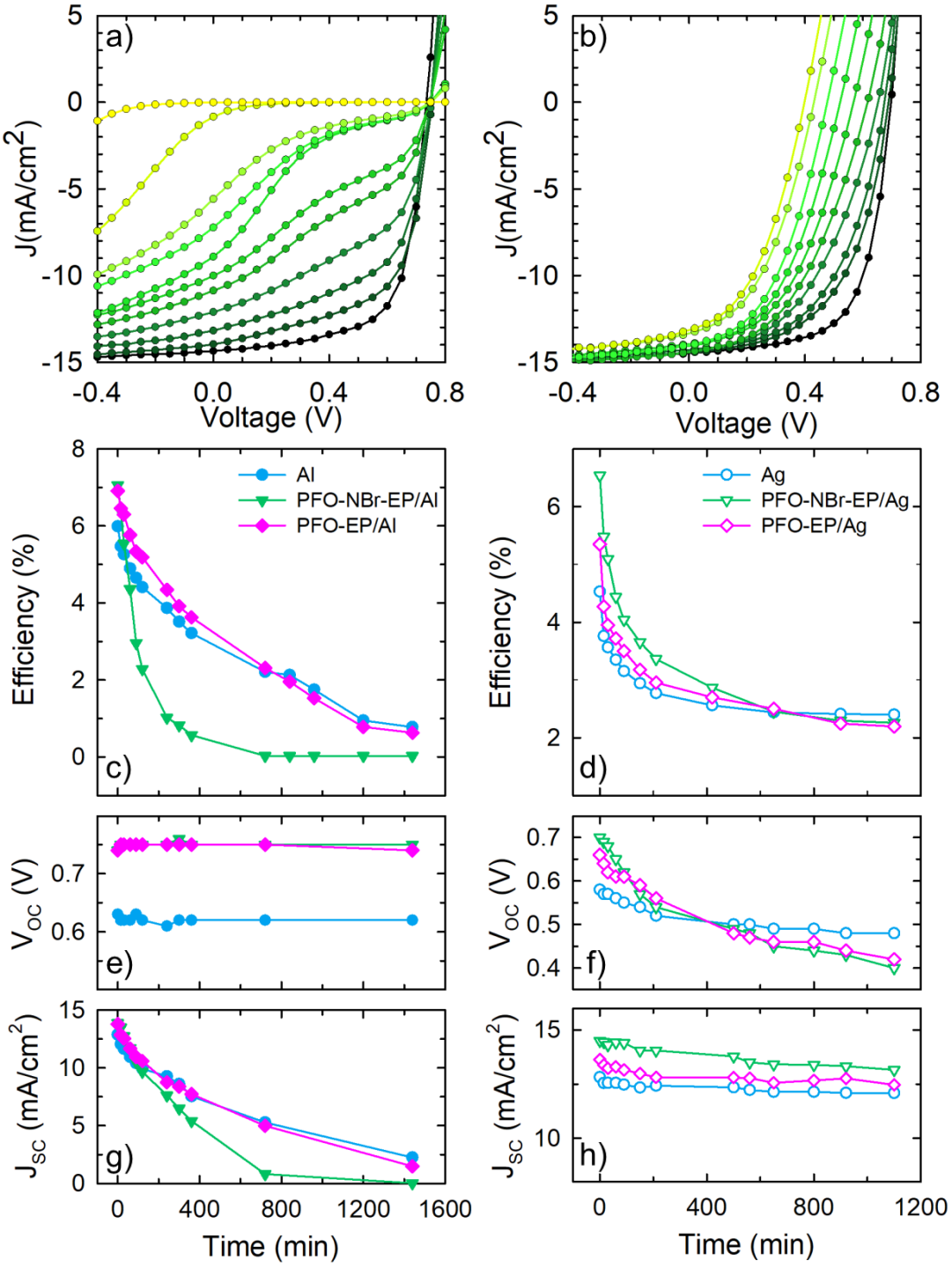

Figure 3.12.: JV characteristics of PTB7:$PC_{71}BM$ devices with PFO-NBr-EP as CIM with Al (a) and Ag (b) as metal cathodes as a function of air exposure time (dark green curve 0 mins, yellow curve 760 mins); Evolution of PCE (c, d), V_{OC} (e, f) and J_{SC} (g, h) of PTB/:$PC_{71}BM$ devices with PFO-NBr-EP (green), PFO-EP (pink)and without CIM (blue) as a function of air exposing time. Filled markers are for devices with Al as cathode, while empty markers are for devices with Ag as cathode.

In analogy to PEDOT:PSS, it is reasonable to argue that the moisture

diffusion in the device is facilitated by the presence of the hydrophilic cathode interlayer which favours the oxidation of the Al electrode. From Fig.3.10 it is possible to derive the rate of degradation of the device containing the PFO-EP interlayer, which is indeed reduced when compared to PFO-EP-NBr and shows a similar trend to the device made with Al. This indicates that there is a balancing between the tendency to oxidation, catalysed by the diffusion of moisture and the protective role of the phosphonated moieties. To be sure about the role of Al oxidation in the degradation of the devices, I have also considered the degradation as a function of storage time of devices prepared using Ag, which is a less reactive metal electrode than Al and which has never been reported to exhibit selective interaction with phosphonate groups.

In the case of silver cathode set, the exposure to air brings the devices to the same final efficiency, approximately 2%, without difference between devices containing CIMs or just ET, fig.3.10b and fig. 3.10d. Moreover in these systems the PV parameters that mostly influences the total efficiency drop turn out to be the V_{OC}, while photocurrent does not exhibit significant variations (fig 3.10.f-h). Formation of kink/charge carrier extraction barrier in the JV curves are not observed. This result can be explained considering that the oxidation of silver leads to a progressive modification of the cathode work function, from 4.3 eV to 5.0 eV, reducing the anode-cathode offset, and thus the V_{OC} of the cell[179, 188, 189]. Moreover, also PEDOT:PSS work function can be modified in presence of moisture when exposed to air. The variation of the energy levels of the electrodes vanishes the presence of any CIM, as shown by the equal efficiency of devices after long exposure to air, indicating that there is no protection effect from the EP side groups with Ag cathode. This result confirms that the drop of efficiency in time in devices with aluminium cathode is due to a degradation process involving the CIM and the aluminium cathode.

3.4. Conclusions

In this work, a novel PFN-based polymer was used as cathodic interlayer in BHJ solar cell with PTB7-$PC_{71}BM$ as active layer. Through the use of electrical and photoelectrical characterization I could assess that the enhancement of the performances of the device are ascribed to the combined positive effect of PFO-NBr-EP and alcoholic solvent. The use of PFO-NBr-EP casted from alcohol solution induces a remarkable 60% increasing of PCE, resulting in a 7.24% compared to device without the interlayer. A comparative study including also a device which underwent bare ethanol treatment allowed to distinguish the contribution of these two factor to the total enhanced performance of the device.

On one hand, I found that polar terminal groups of the side chains of PFO-NBr-EP forma a polar layer at the interface with aluminum. Such layer induces an effective modification of the aluminum cathode work function, which results in a better anode-cathode off-set. The better alignment of interfacial energy levels increased the extraction properties (as deduces from the lower cell resistance and higher fill factor) and hinder charges recombinations in the device. On the other hand the effects of alcohol treatment mainly concern the modification of underlying interface with PEDOT:PSS.

Finally I could discuss the effect of the presence of different lateral group on the PFN backbone in relation to the degradation of the device. This study highlighted that the choice of side groups for PFO-NBr-EP not only boosts the initial efficiency, but, in controlled atmosphere condition, can also limit the efficiency drop which characterizes devices with typical inorganic interlayers as calcium. From the results emerging from the storage of the devices with different cathodes in room atmosphere, a description of degradation mechanism was proposed in relation to the PFO-side chains. It was observed that EP groups can prevent the device from the fast oxidation of cathode inner interface, but they also exhibit a higher hygroscopic than NBr groups, enhancing

the absorbance of water at interface. The balancing of these effect was found determinant for the rate of cathode oxidation.

3.5. Materials and methods

3.5.1 PFO-NBr-EP Synthesis

Intermediate. 2,7-Bis-[9,9'-bis(6''-bromohexyl)fluorenyl]-4,4,5,5-tetramethyl [1.3.2]dioxa-borolane (**1**) and 2,7-Dibromo-9,9-bis(6'-diethoxylphosphorylhexyl)-fluorene (**2**) were prepared according to literature (ref. [190] and [191] respectively). A mixture of 2,7-Bis-[9,9'-bis(6''-bromohexyl) fluorenyl]-4,4,5,5-tetramethyl [1.3.2]dioxa-borolane (**1**) (0.97mg, 0.13 mmol,) and 2,7-Dibromo-9,9-bis(6'-diethoxylphosphorylhexyl)-fluorene (**2**) (100 mg, 0.13 mmol) and $PdCl_2(PPh_3)_2$ (1 mg, 0.0015 mmol), TEBA (5mg as catalist), degassed aqueous potassium carbonate (2 M, 1.5 mL), and Toluene (3 mL) were introduced in a Schenk tube under nitrogen atmosphere. The reaction mixture was stirred for 8 h at 90°C. The end groups were capped with an excess of bromobenzene (0.16 mmol) for 10h and then with an excess of phenylboronic acid pinacol ester (0.16 mmol) for further 10 h.

After cooling to room temperature, the organic phase was filtered on Celite diethoxylphosphorylhexyl)-fluorene)-alt-(2,7-(9,9′-bis(6″-dibromo)hexyl)-fluorene)])] (**3**)with a yield of 86%. 1H NMR (CDCl3, 600 MHz, δ, ppm): 7.85(4H, br, fluorenyl group), 7.69 (8H, m, fluorenyl group), 4.82(8H, m, CH2-O-P), 3.30 (4H, m, −CH2Br), 2.14 (8H, br, −CH2−), 1.70 (4H, br, −CH2−), 1.45 (8H, br,−CH2−),1.26(12H, m, CH3-CH2-O-P) 1.19 (16H, br, −CH2−), 0.83 (8H, br, -CH2-). GPC (THF, polystyrene standard) analysis showed a Mw = 6200 and PDI = 2.26.

The cationic polymer was obtained by trimethylamine ionization of (**3**): 12 mL of a 1:2 v/v solution of condensed trimethylamine in THF were added dropwise to a stirring solution of the neutral precursor polymer (100 mg) in 10 mL of THF at −78 °C. The mixture was then allowed to warm up to room

temperature and then stirred overnight. After the solvent was removed, the salified polymer was recovered as a white-yellow powder in quantitative yield. The complete synthetic scheme of PFO-NBr-EP is reported in fig 3.11.

1H NMR (600 MHz, CD3OD): δ 7.87(4H, br, fluorenyl group), 7.72 (8H, br, fluorenyl group), 3.35(8H, br, CH2-O-P), 2.98 (18H, s, –CH3N), 2.21 (8H, br, –CH2–), 1.56 (8H, br, –CH2–), 1.35 (4H, br,–CH2–), 1.18-1.51 (32H, br, CH3-CH2-O-P and –CH2–), 0.73 (8H, br, -CH2-).

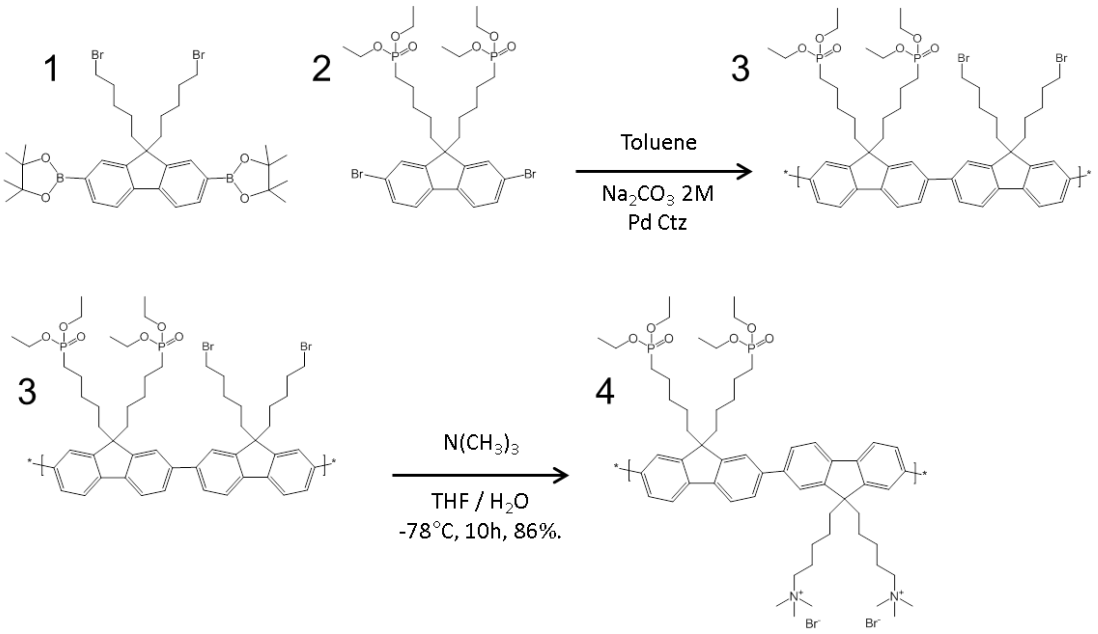

Figura 3.11.: Scheme of the synthesis of PFO-NBr-EP

3.5.2 Device Fabrication

The devices were assembled with a standard geometry glass/ITO/ PEDOT:PSS/active layer/interlayer/cathode. Each ITO-glass substrate, Kintec 15 U sq^{-1} , was mechanically cleaned with wet paper and then washed in an ultrasonic bath at 55° C, sequentially with water, acetone and isopropanol. Subsequently, the substrates were left in an isopropanol bath for 1 h. After drying under a compressed nitrogen flow, the substrates underwent 10 minutes of plasma treatment. Next, PEDOT:PSS (Clevios VP Al 4083) was spin coated on rotating samples at 2000 rpm for 60 seconds (40 nm thick) in air and then

annealed in glovebox on a 110° C hot plate for 10 min. PTB7 (1-material) and PC71BM (Solenne BV, 99% purity) were dissolved at the composition of 1:1.5 weight ratio in chlorobenzene (CB), with a solute concentration of 25 mg/mL and the solution was stirred overnight at 65° C. 10 min before film casting, a 2% v/v of 4-Anisaldehyde was added to the blend solution under stirring on hotplate.

The active layers were spin coated on firm substrate at 1500 rpm for 60 seconds, generating films with thickness of about 90 nm. All devices underwent a solvent evaporation process at room temperature for 20 min followed by an annealing at 65°C for 10 min. In the case of devices treated with alcohol, 60 μl of ethanol were dropped on rotating sample at 1500 rpm and were kept rotating for 60 seconds to facilitate ethanol evaporation. In the case of devices with interlayers, they were casted from ethanol solutions at different concentrations (from 0.2 to 5 mg/ml) on rotating substrate at 4000 rpm for 90 seconds. Finally, a 100 nm Aluminum or Silver layers were thermally evaporated, through a shadow mask under a pressure of $1.5 \cdot 10^{-6}$ mbar. In the comparative device also a 20 nm layer of Calcium was evaporated before Al. The deposition rates were respectively 0.7 nm/s for Ag and Al and 0.1 nm/s for Ca. On each substrate six devices were separately connected and characterized with an active area of 6.1 mm^2 each.

3.5.3. Measurements

The current density–voltage measurements were performed directly in glovebox where the solar cells were assembled, with a Keithley 2602 source meter, under AM 1.5G solar simulation (ABET 2000). The incident power, measured with a calibrated photodiode (Si cell + KG5 filter), was 100 mW cm^2 and subsequently was attenuated through the use of neutral optical filter from 0.1 to 2.5 Optical Density. For the aging measurements, the device were stored under dark condition in glovebox and measured every 48 hours, while in the case of moisture degradation measurements, devices were store in air without

exposition to direct incident light and were measured in increasing time span. The EQE spectral responses were recorded by dispersing a Xe lamp through a monochromator, using a Si solar cell with a calibrated spectral response to measure the incident light power intensity at each wavelength. The devices were taken outside the glovebox for the EQE measurements, after mounting them on a sealed cell to avoid moisture and oxygen exposure.

Impedance spectroscopy measurements were performed in nitrogen atmosphere in dark condition using a Bio Logic SP-200 Research grade Potentiostat/Galvanostat. The devices were measured with an frequency dependent probe voltage of 10 mV in the 100 mHz – 2 MHz frequency range. The frequency-independent voltage was varied from -2V to +1V with the following steps: a 200 mV increase in the -2V – 0V range, a 50 mV increase in the 0V – +0.6V range and a 20 mV increase in the +0.6V – +1V range.

Bibliography

PART I

1. Debije, M.G. and P.P.C. Verbunt, *Solar Concentrators: Thirty Years of Luminescent Solar Concentrator Research: Solar Energy for the Built Environment.* Advanced Energy Materials, 2012. **2**(1): p. 12-35.
2. Currie, M.J., et al., *High-efficiency organic solar concentrators for photovoltaics.* Science, 2008. **321**(5886): p. 226-228.
3. van Sark, W.G.J.H.M., et al., *Luminescent Solar Concentrators - A review of recent results.* Optics Express, 2008. **16**(26): p. 21773-21792.
4. Banal, J.L., K.P. Ghiggino, and W.W.H. Wong, *Efficient light harvesting of a luminescent solar concentrator using excitation energy transfer from an aggregation-induced emitter.* Physical Chemistry Chemical Physics, 2014. **16**(46): p. 25358-25363.
5. Batchelder, J.S., A.H. Zewail, and T. Cole, *Luminescent Solar Concentrators .1. Theory of Operation and Techniques for Performance Evaluation.* Applied Optics, 1979. **18**(18): p. 3090-3110.
6. Weber, W.H. and J. Lambe, *Luminescent greenhouse collector for solar radiation.* Applied Optics, 1976. **15**(10): p. 2299-2300.
7. Goetzberger, A. and W. Greube, *Solar energy conversion with fluorescent collectors.* Applied physics, 1977. **14**(2): p. 123-139.
8. Swanson, R.M., *The promise of concentrators.* Progress in Photovoltaics, 2000. **8**(1): p. 93-111.
9. *The European Parliament and the Council of the European Union. Directive 2010/31/EU of the European Parliament and the Council on the energy performance of buildings (recast)*, in *Official Journal of the European Union*. 2010.
10. Debije, M.G., *Solar Energy Collectors with Tunable Transmission.* Advanced Functional Materials, 2010. **20**(9): p. 1498-1502.

11. Global Industry Analysts Inc., *Building integrated photovoltaics (BIPV) - A global strategic business report.* Report, 2015. **MCP7004**.
12. Castillo-Cagigal, M., et al., *PV self-consumption optimization with storage and Active DSM for the residential sector.* Solar Energy, 2011. **85**(9): p. 2338-2348.
13. Debije, M.G. and P.P.C. Verbunt, *Thirty Years of Luminescent Solar Concentrator Research: Solar Energy for the Built Environment.* Advanced Energy Materials, 2012. **2**(1): p. 12-35.
14. Meinardi, F., et al., *Large-area luminescent solar concentrators based on/Stokes-shift-engineered/'nanocrystals in a mass-polymerized PMMA matrix.* Nature Photonics, 2014. **8**(5): p. 392-399.
15. Meinardi, F., et al., *Highly efficient large-area colourless luminescent solar concentrators using heavy-metal-free colloidal quantum dots.* Nat Nano, 2015.
16. Gallagher, S.J., B. Norton, and P.C. Eames, *Quantum dot solar concentrators: Electrical conversion efficiencies and comparative concentrating factors of fabricated devices.* Solar Energy, 2007. **81**(6): p. 813-821.
17. Reisfeld, R. and R. Zusman, *Thin film of glass or plastic containing dye*. 1987, Google Patents.
18. Kanemoto, R., et al., *Relations between dewetting of polymer thin films and phase-separation of encompassed quantum dots.* Journal of Physical Chemistry C, 2008. **112**(22): p. 8184-8191.
19. Knowles, K.E., et al., *Bright CuInS2/CdS nanocrystal phosphors for high-gain full-spectrum luminescent solar concentrators.* Chemical Communications, 2015. **51**(44): p. 9129-9132.
20. Bullen, C. and P. Mulvaney, *The effects of chemisorption on the luminescence of CdSe quantum dots.* Langmuir, 2006. **22**(7): p. 3007-3013.
21. Zhao, Y.M., et al., *High-Temperature Luminescence Quenching of Colloidal Quantum Dots.* Acs Nano, 2012. **6**(10): p. 9058-9067.
22. Bomm, J., et al., *Fabrication and full characterization of state-of-the-art quantum dot luminescent solar concentrators.* Solar Energy Materials and Solar Cells, 2011. **95**(8): p. 2087-2094.
23. Krumer, Z., et al., *Tackling self-absorption in luminescent solar concentrators with type-II colloidal quantum dots.* Solar Energy Materials and Solar Cells, 2013. **111**(Supplement C): p. 57-65.

24. Desmet, L., et al., *Monocrystalline silicon photovoltaic luminescent solar concentrator with 4.2% power conversion efficiency.* Optics Letters, 2012. **37**(15): p. 3087-3089.
25. Debije, M.G., et al., *Promising fluorescent dye for solar energy conversion based on a perylene perinone.* Applied Optics, 2011. **50**(2): p. 163-169.
26. Sanguineti, A., et al., *NIR emitting ytterbium chelates for colourless luminescent solar concentrators.* Physical Chemistry Chemical Physics, 2012. **14**(18): p. 6452-6455.
27. Turrisi, R., et al., *Stokes shift/emission efficiency trade-off in donor-acceptor perylenemonoimides for luminescent solar concentrators.* Journal of Materials Chemistry A, 2015. **3**(15): p. 8045-8054.
28. Thomas, W.R.L., J.M. Drake, and M.L. Lesiecki, *Light Transport in Planar Luminescent Solar Concentrators - The Role of Matrix Losses.* Applied Optics, 1983. **22**(21): p. 3440-3450.
29. Meinardi, F., et al., *Large-area luminescent solar concentrators based on 'Stokes-shift-engineered' nanocrystals in a mass-polymerized PMMA matrix.* Nature Photonics, 2014. **8**: p. 392.
30. Li, Z., et al., *General Method for the Synthesis of Ultrastable Core/Shell Quantum Dots by Aluminum Doping.* Journal of the American Chemical Society, 2015. **137**(39): p. 12430-12433.
31. Bradshaw, L.R., et al., *Nanocrystals for Luminescent Solar Concentrators.* Nano Letters, 2015. **15**(2): p. 1315-1323.
32. Monguzzi, A., et al., *Vibrational overtones quenching of near infrared emission in Er3+ complexes.* New Journal of Chemistry, 2009. **33**(7): p. 1542-1548.
33. Debije, M.G., et al., *The effect of a scattering layer on the edge output of a luminescent solar concentrator.* Solar Energy Materials and Solar Cells, 2009. **93**(8): p. 1345-1350.
34. Debije, M.G., et al., *Measured surface loss from luminescent solar concentrator waveguides.* Applied Optics, 2008. **47**(36): p. 6763-6768.
35. van Sark, W.G.J.H.M., *Luminescent solar concentrators – A low cost photovoltaics alternative.* Renewable Energy, 2013. **49**(Supplement C): p. 207-210.
36. Sanguineti, A., et al., *High Stokes shift perylene dyes for luminescent solar concentrators.* Chemical Communications, 2013. **49**(16): p. 1618-1620.

37. Yamaguchi, Y., et al., *How the π Conjugation Length Affects the Fluorescence Emission Efficiency.* Journal of the American Chemical Society, 2008. **130**(42): p. 13867-13869.
38. Wang, T., et al., *Luminescent solar concentrator employing rare earth complex with zero self-absorption loss.* Solar Energy, 2011. **85**(11): p. 2571-2579.
39. Zhou, Y., et al., *Near Infrared, Highly Efficient Luminescent Solar Concentrators.* Advanced Energy Materials, 2016. **6**(11): p. 1501913-n/a.
40. Talapin, D.V., et al., *Seeded Growth of Highly Luminescent CdSe/CdS Nanoheterostructures with Rod and Tetrapod Morphologies.* Nano Letters, 2007. **7**(10): p. 2951-2959.
41. Bronstein, N.D., et al., *Luminescent Solar Concentration with Semiconductor Nanorods and Transfer-Printed Micro-Silicon Solar Cells.* Acs Nano, 2014. **8**(1): p. 44-53.
42. Viswanatha, R., et al., *Copper-Doped Inverted Core/Shell Nanocrystals with "Permanent" Optically Active Holes.* Nano Letters, 2011. **11**(11): p. 4753-4758.
43. Hu, X., et al., *Ray-trace simulation of CuInS(Se)2 quantum dot based luminescent solar concentrators.* Optics Express, 2015. **23**(15): p. A858-A867.
44. Coropceanu, I. and M.G. Bawendi, *Core/Shell Quantum Dot Based Luminescent Solar Concentrators with Reduced Reabsorption and Enhanced Efficiency.* Nano Letters, 2014. **14**(7): p. 4097-4101.
45. Erickson, C.S., et al., *Zero-Reabsorption Doped-Nanocrystal Luminescent Solar Concentrators.* Acs Nano, 2014. **8**(4): p. 3461-3467.
46. Tolcin, A.C., *Mineral Commodity Summaries 2015* 2015, U.S. Geological Survey.
47. Moss, R.L., Tzimas, E., Kara, H., Willis, P. & Kooroshy, J., *Critical Metals in Strategic Energy Technologies, Assessing Rare Metals as Supply-Chain Bottlenecks in Low-Carbon Energy Technologies*. 2011, European Commission: Joint Research Centre.
48. Holmes, J.D., et al., *Highly luminescent silicon nanocrystals with discrete optical transitions.* Journal of the American Chemical Society, 2001. **123**(16): p. 3743-3748.
49. Hybertsen, M.S., *Absorption and emission of light in nanoscale silicon structures.* Physical Review Letters, 1994. **72**(10): p. 1514-1517.

50. Lee, B.G., et al., *Quasi-Direct Optical Transitions in Silicon Nanocrystals with Intensity Exceeding the Bulk.* Nano Letters, 2016. **16**(3): p. 1583-1589.
51. Hessel, C.M., et al., *Synthesis of Ligand-Stabilized Silicon Nanocrystals with Size-Dependent Photoluminescence Spanning Visible to Near-Infrared Wavelengths.* Chemistry of Materials, 2012. **24**(2): p. 393-401.
52. Mangolini, L., E. Thimsen, and U. Kortshagen, *High-yield plasma synthesis of luminescent silicon nanocrystals.* Nano Letters, 2005. **5**(4): p. 655-659.
53. Mangolini, L. and U. Kortshagen, *Plasma-assisted synthesis of silicon nanocrystal inks.* Advanced Materials, 2007. **19**(18): p. 2513-+.
54. Jurbergs, D., et al., *Silicon nanocrystals with ensemble quantum yields exceeding 60%.* Applied Physics Letters, 2006. **88**(23): p. 233116.
55. Anthony, R.J., et al., *Routes to Achieving High Quantum Yield Luminescence from Gas-Phase-Produced Silicon Nanocrystals.* Advanced Functional Materials, 2011. **21**(21): p. 4042-4046.
56. Hannah, D.C., et al., *On the Origin of Photoluminescence in Silicon Nanocrystals: Pressure-Dependent Structural and Optical Studies.* Nano Letters, 2012. **12**(8): p. 4200-4205.
57. Delerue, C., G. Allan, and M. Lannoo, *Electron-phonon coupling and optical transitions for indirect-gap semiconductor nanocrystals.* Physical Review B, 2001. **64**(19): p. 193402.
58. Meier, C., et al., *Silicon nanoparticles: Absorption, emission, and the nature of the electronic bandgap.* Journal of Applied Physics, 2007. **101**(10): p. 103112.
59. Slooff, L.H., et al., *A luminescent solar concentrator with 7.1% power conversion efficiency.* physica status solidi (RRL) – Rapid Research Letters, 2008. **2**(6): p. 257-259.
60. Wilson, W.L., P.F. Szajowski, and L.E. Brus, *Quantum Confinement in Size-Selected, Surface-Oxidized Silicon Nanocrystals.* Science, 1993. **262**(5137): p. 1242-1244.
61. Sychugov, I., et al., *Single-dot absorption spectroscopy and theory of silicon nanocrystals.* Physical Review B, 2016. **93**(16): p. 161413.
62. Sangghaleh, F., et al., *Near-Unity Internal Quantum Efficiency of Luminescent Silicon Nanocrystals with Ligand Passivation.* ACS Nano, 2015. **9**(7): p. 7097-7104.

63. Tummeltshammer, C., et al., *Flexible and fluorophore-doped luminescent solar concentrators based on polydimethylsiloxane.* Optics Letters, 2016. **41**(4): p. 713-716.
64. Wu, J.J. and U.R. Kortshagen, *Photostability of thermally-hydrosilylated silicon quantum dots.* RSC Advances, 2015. **5**(126): p. 103822-103828.
65. Rebecca J. Anthony, et al., *Photoluminescence: Routes to Achieving High Quantum Yield Luminescence from Gas-Phase-Produced Silicon Nanocrystals.* Advanced Functional Materials, 2011. **21**(21): p. 4041.

PART II

66. Krebs, F.C., *Polymeric Solar Cells. Materials, Design, Manufacture*. 2010: DEStech Publications, Inc.
67. Spanggaard, H. and F.C. Krebs, *A brief history of the development of organic and polymeric photovoltaics.* Solar Energy Materials and Solar Cells, 2004. **83**(2): p. 125-146.
68. Green, M.A., et al., *Solar cell efficiency tables (Version 45).* Progress in Photovoltaics, 2015. **23**(1): p. 1-9.
69. Green, M.A., *Thin-film solar cells: review of materials, technologies and commercial status.* Journal of Materials Science: Materials in Electronics, 2007. **18**(1): p. 15-19.
70. Ameri, T., N. Li, and C.J. Brabec, *Highly efficient organic tandem solar cells: a follow up review.* Energy & Environmental Science, 2013. **6**(8): p. 2390-2413.
71. O'Regan, B. and M. Grätzel, *A low-cost, high-efficiency solar cell based on dye-sensitized colloidal TiO2 films.* Nature, 1991. **353**: p. 737.
72. Günes, S., H. Neugebauer, and N.S. Sariciftci, *Conjugated Polymer-Based Organic Solar Cells.* Chemical Reviews, 2007. **107**(4): p. 1324-1338.
73. Brabec, C.J., *Organic photovoltaics: technology and market.* Solar Energy Materials and Solar Cells, 2004. **83**(2): p. 273-292.
74. Green, M.A., et al., *Solar cell efficiency tables (version 50).* Progress in Photovoltaics: Research and Applications, 2017. **25**(7): p. 668-676.

75. Takamoto, T., H. Washio, and H. Juso. *Application of InGaP/GaAs/InGaAs triple junction solar cells to space use and concentrator photovoltaic*. in *2014 IEEE 40th Photovoltaic Specialist Conference (PVSC)*. 2014.
76. Niu, G., X. Guo, and L. Wang, *Review of recent progress in chemical stability of perovskite solar cells.* Journal of Materials Chemistry A, 2015. **3**(17): p. 8970-8980.
77. Green, M.A., et al., *Solar cell efficiency tables (Version 45).* Progress in Photovoltaics: Research and Applications, 2015. **23**(1): p. 1-9.
78. Lungenschmied, C., et al., *Flexible, long-lived, large-area, organic solar cells.* Solar Energy Materials and Solar Cells, 2007. **91**(5): p. 379-384.
79. Dennler, G., et al., *Angle dependence of external and internal quantum efficiencies in bulk-heterojunction organic solar cells.* Journal of Applied Physics, 2007. **102**(5): p. 054516.
80. Sacco, A., et al., *Characterization of photovoltaic modules for low-power indoor application.* Applied Energy, 2013. **102**(Supplement C): p. 1295-1302.
81. Nelson, R.C., *Sensitization of Photoconductivity in Cadmium Sulfide*.* Journal of the Optical Society of America, 1956. **46**(1): p. 13-16.
82. Tang, C.W. and A.C. Albrecht, *TRANSIENT PHOTOVOLTAIC EFFECTS IN METAL-CHLOROPHYLL-A-METAL SANDWICH CELLS.* Journal of Chemical Physics, 1975. **63**(2): p. 953-961.
83. Tang, C.W., *Two-layer organic photovoltaic cell.* Applied Physics Letters, 1986. **48**(2): p. 183-185.
84. Scharber, M.C. and N.S. Sariciftci, *Efficiency of bulk-heterojunction organic solar cells.* Progress in Polymer Science, 2013. **38**(12): p. 1929-1940.
85. Blatt, F.J., *Modern Physics*. 1992: McGraw-Hill.
86. Scully, S.R. and M.D. McGehee, *Effects of optical interference and energy transfer on exciton diffusion length measurements in organic semiconductors.* Journal of Applied Physics, 2006. **100**(3): p. 034907.
87. Rauscher, U., et al., *Exciton versus band description of the absorption and luminescence spectra in poly(p-phenylenevinylene).* Physical Review B, 1990. **42**(16): p. 9830-9836.
88. Frankevich, E.L., et al., *POLARON-PAIR GENERATION IN POLY(PHENYLENE VINYLENES).* Physical Review B, 1992. **46**(15): p. 9320-9324.

89. Mozer, A.J. and N.S. Sariciftci, *Conjugated polymer photovoltaic devices and materials.* Comptes Rendus Chimie, 2006. **9**(5-6): p. 568-577.
90. Sariciftci, N.S., et al., *Photoinduced Electron Transfer from a Conducting Polymer to Buckminsterfullerene.* Science, 1992. **258**(5087): p. 1474-1476.
91. Yu, G., et al., *Polymer Photovoltaic cells - Enhanced Efficiencies via a Network of Internal Donor-Acceptor Heterojunctions.* Science, 1995. **270**(5243): p. 1789-1791.
92. Kannan, B., K. Castelino, and A. Majumdar, *Design of Nanostructured Heterojunction Polymer Photovoltaic Devices.* Nano Letters, 2003. **3**(12): p. 1729-1733.
93. Steim, R., F.R. Kogler, and C.J. Brabec, *Interface materials for organic solar cells.* Journal of Materials Chemistry, 2010. **20**(13): p. 2499-2512.
94. Martínez-Otero, A., et al., *High-Performance Polymer Solar Cells Using an Optically Enhanced Architecture.* Advanced Optical Materials, 2013. **1**(1): p. 37-42.
95. Kim, J.Y., et al., *New Architecture for High-Efficiency Polymer Photovoltaic Cells Using Solution-Based Titanium Oxide as an Optical Spacer.* Advanced Materials, 2006. **18**(5): p. 572-576.
96. He, Z., et al., *Enhanced power-conversion efficiency in polymer solar cells using an inverted device structure.* Nature Photonics, 2012. **6**: p. 591.
97. Jong, M.P.d., L.J.v. IJzendoorn, and M.J.A.d. Voigt, *Stability of the interface between indium-tin-oxide and poly(3,4-ethylenedioxythiophene)/poly(styrenesulfonate) in polymer light-emitting diodes.* Applied Physics Letters, 2000. **77**(14): p. 2255-2257.
98. Nunzi, J.M., *Organic photovoltaic materials and devices.* Comptes Rendus Physique, 2002. **3**(4): p. 523-542.
99. Brabec, C.J., et al., *Tracing photoinduced electron transfer process in conjugated polymer/fullerene bulk heterojunctions in real time.* Chemical Physics Letters, 2001. **340**(3-4): p. 232-236.
100. Parker, I.D., *Carrier Tunneling and Device Characteristics in Polymer Light-Emitting Diodes.* Journal of Applied Physics, 1994. **75**(3): p. 1656-1666.

101. Pivrikas, A., et al., *A review of charge transport and recombination in polymer/fullerene organic solar cells.* Progress in Photovoltaics: Research and Applications, 2007. **15**(8): p. 677-696.
102. Drees, M., et al., *Stabilization of the nanomorphology of polymer-fullerene "bulk heterojunction'' blends using a novel polymerizable fullerene derivative.* Journal of Materials Chemistry, 2005. **15**(48): p. 5158-5163.
103. Hoppe, H. and N.S. Sariciftci, *Organic solar cells: An overview.* Journal of Materials Research, 2004. **19**(7): p. 1924-1945.
104. Rostalski, J. and D. Meissner, *Monochromatic versus solar efficiencies of organic solar cells.* Solar Energy Materials and Solar Cells, 2000. **61**(1): p. 87-95.
105. Lee, J.H., et al., *Enhanced diode characteristics of organic solar cells using titanium suboxide electron transport layer.* Applied Physics Letters, 2010. **96**(16): p. 163303.
106. Brabec, C.J., et al., *Origin of the open circuit voltage of plastic solar cells.* Advanced Functional Materials, 2001. **11**(5): p. 374-380.
107. Scharber, M.C., et al., *Design rules for donors in bulk-heterojunction solar cells - Towards 10 % energy-conversion efficiency.* Advanced Materials, 2006. **18**(6): p. 789-+.
108. Campoy-Quiles, M., et al., *Morphology evolution via self-organization and lateral and vertical diffusion in polymer:fullerene solar cell blends.* Nature Materials, 2008. **7**: p. 158.
109. Mishra, A. and P. Bäuerle, *Small Molecule Organic Semiconductors on the Move: Promises for Future Solar Energy Technology.* Angewandte Chemie International Edition, 2012. **51**(9): p. 2020-2067.
110. Halls, J.J.M., et al., *Charge- and energy-transfer processes at polymer/polymer interfaces: A joint experimental and theoretical study.* Physical Review B, 1999. **60**(8): p. 5721-5727.
111. Chen, D., et al., *P3HT/PCBM Bulk Heterojunction Organic Photovoltaics: Correlating Efficiency and Morphology.* Nano Letters, 2011. **11**(2): p. 561-567.
112. Walker, B., et al., *Nanoscale Phase Separation and High Photovoltaic Efficiency in Solution-Processed, Small-Molecule Bulk Heterojunction Solar Cells.* Advanced Functional Materials, 2009. **19**(19): p. 3063-3069.

113. Qi, B. and J. Wang, *Fill factor in organic solar cells.* Physical Chemistry Chemical Physics, 2013. **15**(23): p. 8972-8982.
114. Riedel, I. and V. Dyakonov, *Influence of electronic transport properties of polymer-fullerene blends on the performance of bulk heterojunction photovoltaic devices.* Physica Status Solidi a-Applied Research, 2004. **201**(6): p. 1332-1341.
115. Gebeyehu, D., et al., *Bulk-heterojunction photovoltaic devices based on donor-acceptor organic small molecule blends.* Solar Energy Materials and Solar Cells, 2003. **79**(1): p. 81-92.
116. Lee, H.K.H., et al., *Batch-to-Batch Variation of Polymeric Photovoltaic Materials: its Origin and Impacts on Charge Carrier Transport and Device Performances.* Advanced Energy Materials, 2014. **4**(16): p. 1400768-n/a.
117. Chen, L.-M., et al., *Recent Progress in Polymer Solar Cells: Manipulation of Polymer:Fullerene Morphology and the Formation of Efficient Inverted Polymer Solar Cells.* Advanced Materials, 2009. **21**(14-15): p. 1434-1449.
118. Brabec, C.J., et al., *Polymer–Fullerene Bulk-Heterojunction Solar Cells.* Advanced Materials, 2010. **22**(34): p. 3839-3856.
119. Labram, J.G., et al., *Impact of Fullerene Molecular Weight on P3HT:PCBM Microstructure Studied Using Organic Thin-Film Transistors.* Advanced Energy Materials, 2011. **1**(6): p. 1176-1183.
120. Chen, W. and Q. Zhang, *Recent progress in non-fullerene small molecule acceptors in organic solar cells (OSCs).* Journal of Materials Chemistry C, 2017. **5**(6): p. 1275-1302.
121. Brabec, C.J., et al., *Effect of LiF/metal electrodes on the performance of plastic solar cells.* Applied Physics Letters, 2002. **80**(7): p. 1288-1290.
122. Ma, W., et al., *Thermally Stable, Efficient Polymer Solar Cells with Nanoscale Control of the Interpenetrating Network Morphology.* Advanced Functional Materials, 2005. **15**(10): p. 1617-1622.
123. Thompson, B.C. and J.M.J. Fréchet, *Polymer–Fullerene Composite Solar Cells.* Angewandte Chemie International Edition, 2008. **47**(1): p. 58-77.
124. Po, R., et al., *"All That Glisters Is Not Gold": An Analysis of the Synthetic Complexity of Efficient Polymer Donors for Polymer Solar Cells.* Macromolecules, 2015. **48**(3): p. 453-461.

125. Liao, S.-H., et al., *Single Junction Inverted Polymer Solar Cell Reaching Power Conversion Efficiency 10.31% by Employing Dual-Doped Zinc Oxide Nano-Film as Cathode Interlayer.* Scientific Reports, 2014. **4**: p. 6813.
126. He, Z., et al., *Simultaneous Enhancement of Open-Circuit Voltage, Short-Circuit Current Density, and Fill Factor in Polymer Solar Cells.* Advanced Materials, 2011. **23**(40): p. 4636-4643.
127. He, Z., H. Wu, and Y. Cao, *Recent Advances in Polymer Solar Cells: Realization of High Device Performance by Incorporating Water/Alcohol-Soluble Conjugated Polymers as Electrode Buffer Layer.* Advanced Materials, 2014. **26**(7): p. 1006-1024.
128. Chueh, C.-C., C.-Z. Li, and A.K.Y. Jen, *Recent progress and perspective in solution-processed Interfacial materials for efficient and stable polymer and organometal perovskite solar cells.* Energy & Environmental Science, 2015. **8**(4): p. 1160-1189.
129. Reese, M.O., et al., *Optimal negative electrodes for poly(3-hexylthiophene): [6,6]-phenyl C61-butyric acid methyl ester bulk heterojunction photovoltaic devices.* Applied Physics Letters, 2008. **92**(5): p. 053307.
130. Duan, C., et al., *Conjugated zwitterionic polyelectrolyte-based interface modification materials for high performance polymer optoelectronic devices.* Chemical Science, 2013. **4**(3): p. 1298-1307.
131. Liu, W., et al., *Solution-Processed 8-Hydroquinolatolithium as Effective Cathode Interlayer for High-Performance Polymer Solar Cells.* ACS Applied Materials & Interfaces, 2016. **8**(14): p. 9254-9261.
132. Liao, S.-H., et al., *Fullerene Derivative-Doped Zinc Oxide Nanofilm as the Cathode of Inverted Polymer Solar Cells with Low-Bandgap Polymer (PTB7-Th) for High Performance.* Advanced Materials, 2013. **25**(34): p. 4766-4771.
133. Kim, J.S., et al., *Control of the electrode work function and active layer morphology via surface modification of indium tin oxide for high efficiency organic photovoltaics.* Applied Physics Letters, 2007. **91**(11): p. 112111.
134. Hoke, E.T., et al., *Recombination in Polymer:Fullerene Solar Cells with Open-Circuit Voltages Approaching and Exceeding 1.0 V.* Advanced Energy Materials, 2013. **3**(2): p. 220-230.

135. Marzano, G., et al., *Organometallic Approaches to Conjugated Polymers for Plastic Solar Cells: From Laboratory Synthesis to Industrial Production.* European Journal of Organic Chemistry, 2014(30): p. 6583-6614.
136. Mercier, L.G. and M. Leclerc, *Direct (Hetero)Arylation: A New Tool for Polymer Chemists.* Accounts of Chemical Research, 2013. **46**(7): p. 1597-1605.
137. Okamoto, K., et al., *C-H Arylation Reaction: Atom Efficient and Greener Syntheses of pi-Conjugated Small Molecules and Macromolecules for Organic Electronic Materials.* Macromolecules, 2013. **46**(20): p. 8059-8078.
138. Marzano, G., et al., *Tin-Free Synthesis of a Ternary Random Copolymer for BHJ Solar Cells: Direct (Hetero)arylation versus Stille Polymerization.* Macromolecules, 2015. **48**(19): p. 7039-7048.
139. Beaupre, S., et al., *Thieno-, Furo-, and Selenopheno 3,4-c pyrrole-4,6-dione Copolymers: Effect of the Heteroatom on the Electrooptical Properties.* Macromolecules, 2012. **45**(17): p. 6906-6914.
140. Wakioka, M., et al., *A Highly Efficient Catalyst for the Synthesis of Alternating Copolymers with Thieno 3,4-c pyrrole-4,6-dione Units via Direct Arylation Polymerization.* Macromolecules, 2014. **47**(2): p. 626-631.
141. Zou, Y., et al., *A Thieno 3,4-c pyrrole-4,6-dione-Based Copolymer for Efficient Solar Cells.* Journal of the American Chemical Society, 2010. **132**(15): p. 5330-+.
142. Cabanetos, C., et al., *Linear Side Chains in Benzo 1,2-b:4,5-b ' dithiophene-Thieno 3,4-c pyrrole-4,6-dione Polymers Direct Self-Assembly and Solar Cell Performance.* Journal of the American Chemical Society, 2013. **135**(12): p. 4656-4659.
143. Friedel, B., et al., *Influence of solution heating on the properties of PEDOT:PSS colloidal solutions and impact on the device performance of polymer solar cells.* Organic Electronics, 2011. **12**(10): p. 1736-1745.
144. Bartelt, J.A., et al., *Controlling Solution-Phase Polymer Aggregation with Molecular Weight and Solvent Additives to Optimize Polymer-Fullerene Bulk Heterojunction Solar Cells.* Advanced Energy Materials, 2014. **4**(9).
145. Kumar, A., et al., *Interface limited charge extraction and recombination in organic photovoltaics.* Energy & Environmental Science, 2014. **7**(7): p. 2227-2231.

146. Wang, Y., et al., *Significant Enhancement of Polymer Solar Cell Performance via Side-Chain Engineering and Simple Solvent Treatment.* Chemistry of Materials, 2013. **25**(15): p. 3196-3204.
147. Min Nam, Y., J. Huh, and W. Ho Jo, *Optimization of thickness and morphology of active layer for high performance of bulk-heterojunction organic solar cells.* Solar Energy Materials and Solar Cells, 2010. **94**(6): p. 1118-1124.
148. Hoven, C.V., et al., *Improved Performance of Polymer Bulk Heterojunction Solar Cells Through the Reduction of Phase Separation via Solvent Additives.* Advanced Materials, 2010. **22**(8): p. E63-+.
149. Cowan, S.R., A. Roy, and A.J. Heeger, *Recombination in polymer-fullerene bulk heterojunction solar cells.* Physical Review B, 2010. **82**(24): p. 245207.
150. Koster, L.J.A., V.D. Mihailetchi, and P.W.M. Blom, *Bimolecular recombination in polymer/fullerene bulk heterojunction solar cells.* Applied Physics Letters, 2006. **88**(5): p. 052104.
151. Duan, C., et al., *Recent advances in water/alcohol-soluble [small pi]-conjugated materials: new materials and growing applications in solar cells.* Chemical Society Reviews, 2013. **42**(23): p. 9071-9104.
152. Zhang, B., et al., *On the origin of efficient electron injection at phosphonate-functionalized polyfluorene/aluminum interface in efficient polymer light-emitting diodes.* Applied Physics Letters, 2010. **97**(4): p. 043506.
153. Seo, J.H., et al., *Improved High-Efficiency Organic Solar Cells via Incorporation of a Conjugated Polyelectrolyte Interlayer.* Journal of the American Chemical Society, 2011. **133**(22): p. 8416-8419.
154. Na, S.-I., et al., *Efficient organic solar cells with polyfluorene derivatives as a cathode interfacial layer.* Organic Electronics, 2009. **10**(3): p. 496-500.
155. Zhao, Y., et al., *Enhanced charge collection in polymer photovoltaic cells by using an ethanol-soluble conjugated polyfluorene as cathode buffer layer.* Solar Energy Materials and Solar Cells, 2009. **93**(5): p. 604-608.
156. Zhang, W., et al., *A PTB7-based narrow band-gap conjugated polyelectrolyte as an efficient cathode interlayer in PTB7-based polymer solar cells.* Chemical Communications, 2017. **53**(12): p. 2005-2008.
157. Zhang, W., et al., *Highly efficient polymer solar cells with PTB7-based narrow band-gap conjugated polyelectrolytes as cathode interlayers: Device performance*

dependence on the ionic pendants. Organic Electronics, 2017. **47**(Supplement C): p. 94-101.

158. Hu, Z., et al., *Self-Doped N-Type Water/Alcohol Soluble-Conjugated Polymers with Tailored Backbones and Polar Groups for Highly Efficient Polymer Solar Cells.* Solar RRL, 2017. **1**(6): p. 1700055-n/a.
159. Hu, L., et al., *Alcohol-Soluble n-Type Conjugated Polyelectrolyte as Electron Transport Layer for Polymer Solar Cells.* Macromolecules, 2015. **48**(16): p. 5578-5586.
160. Sun, J., et al., *High Efficiency and High Voc Inverted Polymer Solar Cells Based on a Low-Lying HOMO Polycarbazole Donor and a Hydrophilic Polycarbazole Interlayer on ITO Cathode.* The Journal of Physical Chemistry C, 2012. **116**(27): p. 14188-14198.
161. Oh, S.-H., et al., *Water-Soluble Polyfluorenes as an Interfacial Layer Leading to Cathode-Independent High Performance of Organic Solar Cells.* Advanced Functional Materials, 2010. **20**(12): p. 1977-1983.
162. Lee, B.H., et al., *Multi-Charged Conjugated Polyelectrolytes as a Versatile Work Function Modifier for Organic Electronic Devices.* Advanced Functional Materials, 2014. **24**(8): p. 1100-1108.
163. Yao, S., et al., *Influence of a polyelectrolyte based-fluorene interfacial layer on the performance of a polymer solar cell.* Journal of Materials Chemistry A, 2013. **1**(37): p. 11443-11450.
164. Yang, T., et al., *Inverted polymer solar cells with 8.4% efficiency by conjugated polyelectrolyte.* Energy & Environmental Science, 2012. **5**(8): p. 8208-8214.
165. Zhou, Y., et al., *A Universal Method to Produce Low–Work Function Electrodes for Organic Electronics.* Science, 2012. **336**(6079): p. 327-332.
166. Sprau, C., et al., *Highly efficient polymer solar cells cast from non-halogenated xylene/anisaldehyde solution.* Energy & Environmental Science, 2015. **8**(9): p. 2744-2752.
167. Yi, C., et al., *Interfacial engineering for high performance organic photovoltaics.* Materials Today, 2016. **19**(3): p. 169-177.
168. Seo, J.H. and T.-Q. Nguyen, *Electronic Properties of Conjugated Polyelectrolyte Thin Films.* Journal of the American Chemical Society, 2008. **130**(31): p. 10042-10043.

169. Liu, Z., et al., *Efficient polymer solar cells based on the synergy effect of a novel non-conjugated small-molecule electrolyte and polar solvent.* Journal of Materials Chemistry A, 2016. **4**(7): p. 2530-2536.
170. Sun, Q., et al., *A two-step strategy to clarify the roles of a solution processed PFN interfacial layer in highly efficient polymer solar cells.* Journal of Materials Chemistry A, 2015. **3**(36): p. 18432-18441.
171. Li, Y.-L., et al., *Structure Tuning of Crown Ether Grafted Conjugated Polymers as the Electron Transport Layer in Bulk-Heterojunction Polymer Solar Cells for High Performance.* Advanced Functional Materials, 2014. **24**(43): p. 6811-6817.
172. Zhou, H., et al., *High-Efficiency Polymer Solar Cells Enhanced by Solvent Treatment.* Advanced Materials, 2013. **25**(11): p. 1646-1652.
173. Brus, V.V., et al., *Quantifying interface states and bulk defects in high-efficiency solution-processed small-molecule solar cells by impedance and capacitance characteristics.* Progress in Photovoltaics: Research and Applications, 2015. **23**(11): p. 1526-1535.
174. Brus, V.V., et al., *Capacitance Spectroscopy for Quantifying Recombination Losses in Nonfullerene Small-Molecule Bulk Heterojunction Solar Cells.* Advanced Energy Materials, 2016. **6**(11): p. 1502250-n/a.
175. Qi, B., Z.-G. Zhang, and J. Wang, *Uncovering the role of cathode buffer layer in organic solar cells.* Scientific Reports, 2015. **5**: p. 7803.
176. Tan, Z.-K., et al., *In-Situ Switching from Barrier-Limited to Ohmic Anodes for Efficient Organic Optoelectronics.* Advanced Functional Materials, 2014. **24**(20): p. 3051-3058.
177. van Reenen, S., et al., *Origin of Work Function Modification by Ionic and Amine-Based Interface Layers.* Advanced Materials Interfaces, 2014. **1**(8): p. 1400189-n/a.
178. Jørgensen, M., K. Norrman, and F.C. Krebs, *Stability/degradation of polymer solar cells.* Solar Energy Materials & Solar Cells, 2008. **92**: p. 686-714.
179. Grossiord, N., et al., *Degradation mechanisms in organic photovoltaic devices.* Organic Electronics, 2012. **13**(3): p. 432-456.
180. Kawano, K., et al., *Degradation of organic solar cells due to air exposure.* Solar Energy Materials and Solar Cells, 2006. **90**(20): p. 3520-3530.

181. Chang, Y.-M., et al., *Electrostatic Self-Assembly Conjugated Polyelectrolyte-Surfactant Complex as an Interlayer for High Performance Polymer Solar Cells.* Advanced Functional Materials, 2012. **22**(15): p. 3284-3289.
182. Liu, J., et al., *Printable Highly Conductive Conjugated Polymer Sensitized ZnO NCs as Cathode Interfacial Layer for Efficient Polymer Solar Cells.* ACS Applied Materials & Interfaces, 2014. **6**(11): p. 8237-8245.
183. Zhao, W., T. Cao, and J.M. White, *On the Origin of Green Emission in Polyfluorene Polymers: The Roles of Thermal Oxidation Degradation and Crosslinking.* Advanced Functional Materials, 2004. **14**(8): p. 783-790.
184. Gong, X., et al., *White Light Electrophosphorescence from Polyfluorene-Based Light-Emitting Diodes: Utilization of Fluorenone Defects.* The Journal of Physical Chemistry B, 2004. **108**(25): p. 8601-8605.
185. Lee, J.-I., G. Klaerner, and R.D. Miller, *Oxidative Stability and Its Effect on the Photoluminescence of Poly(Fluorene) Derivatives: End Group Effects.* Chemistry of Materials, 1999. **11**(4): p. 1083-1088.
186. Grisorio, R., et al., *On the Degradation Process Involving Polyfluorenes and the Factors Governing Their Spectral Stability.* Macromolecules, 2011. **44**(20): p. 7977-7986.
187. Voroshazi, E., et al., *Influence of cathode oxidation via the hole extraction layer in polymer:fullerene solar cells.* Organic Electronics, 2011. **12**(5): p. 736-744.
188. Lloyd, M.T., et al., *Impact of contact evolution on the shelf life of organic solar cells.* Journal of Materials Chemistry, 2009. **19**(41): p. 7638-7642.
189. Choi, H.W., et al., *Enhancement of hole injection using O2 plasma-treated Ag anode for top-emitting organic light-emitting diodes.* Applied Physics Letters, 2005. **86**(1): p. 012104.
190. Chi, C., A. Mikhailovsky, and G.C. Bazan, *Design of Cationic Conjugated Polyelectrolytes for DNA Concentration Determination.* Journal of the American Chemical Society, 2007. **129**(36): p. 11134-11145.
191. Qin, C., et al., *Phosphonate-Functionalized Polyfluorene as a Highly Water-Soluble Iron(III) Chemosensor.* Macromolecules, 2008. **41**(21): p. 7798-7804.